

IAEA Photonuclear Data Library 2019

T. Kawano,^{1,*} Y. S. Cho,² P. Dimitriou,³ D. Filipescu,⁴ N. Iwamoto,⁵ V. Plujko,⁶ X. Tao,⁷ H. Utsunomiya,⁸ V. Varlamov,⁹ R. Xu,⁷ R. Capote,³ I. Gheorghe,⁴ O. Gorbachenko,⁶ Y.L. Jin,⁷ T. Renstrøm,¹⁰ K. Stopani,⁹ Y. Tian,⁷ G. M. Tveten,¹⁰ J.M. Wang,⁷ T. Belgia,¹¹ R. Firestone,¹² S. Goriely,¹³ J. Kopecky,¹⁴ M. Kr̄t̄iĉka,¹⁵ R. Schwengner,¹⁶ S. Siem,¹⁰ and M. Wiedeking¹⁷

¹*Theoretical Division, Los Alamos National Laboratory, Los Alamos, NM 87545, USA*

²*Nuclear Data Center, Korea Atomic Energy Research Institute, Daedeok-Daero 989-111, Yuseong-gu, Daejeon, Korea*

³*NPAC-Nuclear Data Section, International Atomic Energy Agency, PO Box 100, 1400 Vienna, Austria*

⁴*Horia Hulubei National Institute for Physics and Nuclear Engineering (IFIN-HH), 30 Reactorului, Bucharest-Magurele 077125, Romania*

⁵*Nuclear Data Center, Japan Atomic Energy Agency, Tokai-mura, Ibaraki 319-1195, Japan*

⁶*Nuclear Physics Department, Taras Shevchenko National University, Kyiv, Ukraine*

⁷*China Nuclear Data Center, China Institute of Atomic Energy, P.O. Box 275(41), Beijing 102413, China*

⁸*Department of Physics, Konan University, Okamoto 8-9-1, Higashinada, Kobe 658-8501, Japan*

⁹*Lomonosov Moscow State University, Skobeltsyn Institute of Nuclear Physics, Moscow 119991, Russia*

¹⁰*University of Oslo, Sem Saelands vel 24, P.O. Box 1048, Oslo 0316, Norway*

¹¹*Centre for Energy Research, Hungarian Academy of Sciences, Konkoly Thege Miklos 29-33, 1525 Budapest, Hungary*

¹²*University of California, Berkeley CA 94720, USA*

¹³*Institut d'Astronomie et d'Astrophysique, Université Libre de Bruxelles, Campus de la Plaine, CP 226, 1050 Brussels, Belgium*

¹⁴*JUKO Research, Kalmanstraat 4, Alkmaar 1817, The Netherlands*

¹⁵*Charles University, V Holešoviĉkách 2, 18000 Prague, Czech Republic*

¹⁶*Helmholtz Zentrum Dresden-Rossendorf, Bautzner Landstrasse 400, 01328 Dresden, Germany*

¹⁷*Themba LABS, P.O. Box 722, Somerset West, 7129, South Africa*

(Dated: January 20, 2022; Received xx July 2018; revised received xx September 2018; accepted xx October 2018)

Photo-induced reaction cross section data are of importance for a variety of current or emerging applications, such as radiation shielding design and radiation transport analyses, calculations of absorbed dose in the human body during radiotherapy, physics and technology of fission reactors (influence of photo-reactions on neutron balance) and fusion reactors (plasma diagnostics and shielding), activation analyses, safeguards and inspection technologies, nuclear waste transmutation, medical isotope production and astrophysical applications.

To address these data needs the IAEA Photonuclear Data library was produced in 2000, containing evaluated photo-induced cross sections and neutron spectra for 164 nuclides which were deemed relevant for the applications.

Since the release of the IAEA Photonuclear Data Library however, new experimental data as well as new methods to assess the reliability of experimental cross sections have become available. Theoretical models and input parameters used to evaluate photo-induced reactions have improved significantly over the years. In addition, new measurements of partial photoneutron cross sections using mono-energetic photon beams and advanced neutron detection systems have been performed allowing for the validation of the evaluations and assessments of the experimental data. Furthermore, technological advances have led to the construction of new and more powerful gamma-beam facilities, therefore new data needs are emerging.

We report our coordinated efforts to address these data needs and present the results of the new evaluations of more than 200 nuclides included in the new updated IAEA Photonuclear Data Library, where the photon energy goes up to 200 MeV. We discuss the new assessment method and make recommendations to the user community in cases where the experimental data are discrepant and the assessments disagree. In addition, in the absence of experimental data, we present model predictions for photo-induced reaction cross section on nuclides of potential interest to medical radioisotope production.

* Corresponding author: kawano@lanl.gov

CONTENTS			
I. INTRODUCTION	2	3. ^{239}Pu	32
II. DEFINITIONS	4	E. Data Evaluation at CIAE	34
III. AVAILABLE EXPERIMENTAL DATA	5	1. ^9Be	34
A. Experiments	5	2. ^{14}N	34
1. Bremsstrahlung	5	3. ^{16}O	36
2. Positron Annihilation in Flight	5	4. ^{27}Al	36
3. Bremsstrahlung Tagging	6	5. ^{50}Cr	36
4. Laser Compton-scattering	6	6. ^{90}Zr	37
B. Partial Reaction Measurement	8	7. ^{118}Sn	38
1. Bremsstrahlung	8	VI. CONTENTS OF THE LIBRARY	40
2. Quasi-monoenergetic Annihilation Photons	8	VII. CONCLUSIONS	40
3. Bremsstrahlung Activation	9	Acknowledgments	41
4. Direct neutron-multiplicity sorting with a flat-efficiency detector	9	References	41
C. Experimental Databases and Resources	11	A. Contents of IAEA 1999 and 2019 Photonuclear Data Libraries	47
1. Bibliographic Data	11	B. GDR ATLAS	49
2. Compilation of Photonuclear Cross Sections and GDR Parameters	11	I. INTRODUCTION	
3. EXFOR Database	11	Photonuclear data describing interactions of photons with atomic nuclei are important for a range of applications such as (i) radiation shielding and radiation transport analyses, (ii) calculation of absorbed doses in the human body during radiotherapy, (iii) activation analyses, (iv) safeguards and inspection technologies, (v) nuclear waste transmutation, (vi) fission and fusion reactor technologies, and (vii) astrophysical nucleosynthesis.	
IV. NUCLEAR MODELS AND CODES	11	Photons can be produced as bremsstrahlung radiation by electron accelerators which are commonly used in hospitals, industries and laboratories. Significant technological advances led to the production of quasi-monochromatic beams using the positron annihilation in flight technique at the national facilities of the Lawrence Livermore National Laboratory (LLNL, USA) and Centre d'Études Nucléaires de Saclay (France) in the 1960's. As a result, a large number of measurements of photonuclear cross sections was performed at these two facilities for almost three decades (1962 – 1987). This pioneering work was captured by B.L. Berman in his comprehensive compilation of photonuclear cross sections “Atlas of Photoneutron Cross-sections obtained by Monoenergetic Photons” published in 1975 [1], and later in the follow-up produced in 1988 [2]. Note that because these institutes changed their names several times, we herewith abbreviate them simply to Livermore and Saclay.	
A. Theory for Photonuclear Reactions	11	Despite those experimental efforts, there was still a need for evaluated photonuclear data since (a) it is not possible to produce a complete photonuclear data files based on measured cross sections alone, (b) often the experimental data suffer from systematic discrepancies which are not easy to resolve, and (c) there is a lack of data in a number of cases. These deficiencies in the ex-	
1. Photo-Absorption Cross Section	11		
2. Pre-Equilibrium Particle Emission	12		
3. Decay of Compound Nucleus	13		
4. Energy and Angular Distributions of Secondary Particles	14		
5. Model Parameters in Photonuclear Reaction Calculation	14		
B. Nuclear Reaction Codes for Photonuclear Data Evaluation	14		
1. Special notes on each model code	15		
2. Photonuclear reaction code inter-comparison	15		
V. EVALUATION	15		
A. Evaluation of Experimental Data	16		
B. Data Evaluation at KAERI	18		
1. ^{94}Zr	19		
2. ^{133}Cs	20		
3. ^{138}Ba	20		
4. ^{142}Ce	20		
C. Data Evaluation at IFIN-HH	23		
1. ^{59}Co	23		
2. ^{89}Y	25		
3. ^{103}Rh	25		
4. ^{159}Tb	26		
5. ^{165}Ho	26		
6. ^{169}Tm	27		
7. ^{181}Ta	27		
D. Data Evaluation at JAEA	31		
1. ^{40}Ca	31		
2. ^{139}La	32		

perimental data can be addressed and often resolved by performing an evaluation which consists of three systematic operations: compilation of experimental data, critical assessment of the measurement techniques used and theoretical calculations based on reliable nuclear models. As a result of the evaluation, one can obtain production cross sections as well as energy and angular distributions of the emitted particle for a wide range of incident and outgoing energies, which is useful for the applications.

To address the growing needs for photonuclear data, the IAEA held a Coordinated Research Project (CRP) under the title *Compilation and Evaluation of Photonuclear Data for Applications* between 1996 and 1999. This CRP produced the IAEA Photonuclear Data Library which is described in the *Handbook on Photonuclear Data for Applications* [3] and is available at the IAEA web-site (<http://www-nds.iaea.org/photonuclear>). The library includes photon absorption data, total and partial photo-neutron reaction cross sections and neutron spectra for 164 isotopes, primarily for structural, shielding, biological and fissionable materials. In this paper we refer this previous library to IAEA 1999.

The list of 164 isotopes included in the 1999 Photonuclear Data Library [3] can be broken down in four categories:

- Structural, shielding and bremsstrahlung target materials: Be, Al, Si, Ti, V, Cr, Fe, Co, Ni, Cu, Zn, Zr, Mo, Sn, Ta, W, and Pb.
- Biological materials: C, N, O, Na, S, P, Cl, and Ca;
- Fissionable materials: Th, U, Np, and Pu; and
- Other materials: H, K, Ge, Sr, Nb, Pd, Ag, Cd, Sb, Te, I, Cs, Sm, and Tb.

Of the above four categories, the most important for the applications are the 40 major isotopes of the 29 elements in the first three groups.

Although this database has been extremely useful to a broad user community, it has become evident that it needs to be revised since

- some of the experimental data measured with quasi-monochromatic photon beams are unreliable and discrepant,
- data have been measured for 37 isotopes that have not been evaluated,
- improved methods to resolve experimental discrepancies are available, and
- new data measured with modern techniques have been published in recent years.

New experimental facilities, such as HI γ S at the Triangle University National Laboratory (USA) and the Laser Compton Scattering Facility (NewSUBARU) at University of Hyogo (Japan), offering highly monoenergetic photon beams in combination with advancements in neutron

detector technologies have opened the field to new possibilities: new measurements of photo-neutron cross sections with better accuracy that are expected to help resolve the long-standing discrepancies observed between the data measured using quasi-monoenergetic beams.

Furthermore, the needs for evaluated photonuclear data are growing. In the field of medical isotope production, photonuclear reactions are being explored for the production of medical radionuclides. With the advent of new facilities producing brilliant photon beams with extremely high activity, photo-production of some important radionuclides could become a competitive alternative to the traditional methods using neutrons produced at highly-enriched Uranium reactors or charged-particle beams [4–7]. A list of radionuclides proposed for potential diagnostic and therapeutic applications in nuclear medicine which have also been identified as suitable candidates for production via photonuclear reactions is given below:

- $^{166,170}\text{Er}$ for the production of $^{165,169}\text{Er}$,
- ^{187}Re for the production of ^{186}Re ,
- ^{226}Ra for the production of ^{225}Ra which further decays to ^{225}Ac ,
- ^{98}Ru for the production of ^{97}Ru ,
- ^{194}Pt for the production of $^{193\text{m}}\text{Pt}$,
- ^{132}Xe for the production of ^{131}I ,
- ^{162}Dy for the production of ^{161}Tb , and
- ^{178}Hf for the production of ^{177}Lu .

Other important candidates such as ^{100}Mo (for the production of ^{99}Mo via (γ, n)), ^{48}Ca , ^{52}Cr , ^{65}Cu , ^{48}Ti and ^{46}Ti are already included in the existing photonuclear data library.

In view of the above developments, it was timely to update the existing IAEA Photonuclear Data Library to reflect the progress in the field and the emerging demands for photonuclear data. A coordinated research project (CRP) was endorsed by the International Nuclear Data Committee at the 2014 meeting in Vienna and was initiated by the IAEA with the title “Updating the Photonuclear Data Library.” All the 164 isotopes in the existing library were revisited and evaluated by considering new data, the results of experimental-based evaluations as well as the new Giant Dipole Resonance (GDR) parameters from the recently updated Atlas of GDR parameters [8] and improved reaction models. In addition to these 164 isotopes, evaluations were performed for 37 isotopes for which experimental data are available, as well as for the 9 isotopes identified in the above-mentioned list as relevant for medical applications. In some cases where no experimental information is available, a model prediction is given as the evaluation. In total, 220 isotopes were evaluated. All available experimental data for photo-absorption cross sections, photo-neutron production cross

sections and yields, as well as for partial photo-neutron cross sections and photo-charged-particle cross sections that were available in the EXFOR database [9] up to the cut-off date of April 2019 were considered. In addition, all the new measurements obtained with the new direct neutron-multiplicity sorting technique [10] that was fully developed and implemented for the CRP, were also taken into account in the evaluations. The evaluations were extended to energies of 200 MeV for use in accelerator-driven transmutation technologies, to complement the neutron and proton high-energy libraries that are being developed for radiation transport simulation codes.

The CRP has a second branch under the title “Generating a Reference Database for Photon Strength Functions” which has led to a new database of experimental and calculated photon strength functions [11]. The evaluations performed for the updated photonuclear data library have formed the basis for the recommended photonuclear photon strength functions in Ref. [11]. In this paper we adopt the same definition of the photon strength functions as in Ref. [11].

In this report, we present the results of both experimental and evaluation efforts carried out within the CRP to update the IAEA Photonuclear Data Library. The measurements of reliable photo-neutron production cross sections using the new neutron multiplicity sorting technique as well as an overview of all available experimental data can be found in Sec. III. In Sec. IV, we present the nuclear reaction models that are used to describe photonuclear reactions as well as the different codes employed in this coordinated effort. In Sec. V, we present the different evaluations and highlight some comparisons with experimental data. The contents of the new IAEA photonuclear data library are described in Sec. VI. Our conclusions are given in Sec. VII. The new Atlas of GDR parameters is provided in the Appendix.

II. DEFINITIONS

Experimental photonuclear reaction data are usually obtained by directly counting the number of emitted particles or by measuring the residual nucleus activity. For energies above the multi-particle emission threshold, more than one combination of emitted light-particles can accompany the same number of produced neutrons or can lead to the same residual nucleus, respectively. Often, authors do not mention clearly what it is they measure which can lead to confusion when comparing experimental data with evaluations. For example, an experimental data set that is reported as the (γ, n) cross section could have charged particles emitted concurrently with one-neutron emission, *i.e.* $(\gamma, 1n) + (\gamma, 1np) + (\gamma, n2p) + \dots$ depending on the energy. This can lead to significant differences, especially for light nuclei, where photo-charged-particle emission is quite strong. Here we define several cross sections relevant to the photonuclear data library.

When the charged-particle emission is negligible, the

measured one-neutron emission cross section is identical to the cross section for the production of $(Z, A - 1)$ nucleus, and the two-neutron emission is equal to the production of $(Z, A - 2)$, and so on. However, when charged-particle emission is non-negligible, then the measured one-neutron emission cross section σ_{1nX} should read

$$\sigma_{1nX} = \sigma(\gamma, 1n) + \sigma(\gamma, np) + \sigma(\gamma, n\alpha) + \dots, \quad (1)$$

and *ditto* for $\sigma(\gamma, 2nX)$, $\sigma(\gamma, 3nX)$, *etc.* Thus, $\sigma(\gamma, inX)$ is understood to be the inclusive i -neutron emission cross section, where X stands for anything except for i -neutrons. These cross sections are not given explicitly in the evaluated photonuclear data library, instead one has to reconstruct σ_{1nX} by summing each term in Eq. (1).

The photo-neutron production cross section is defined in two ways, either involving the neutron multiplicity or not. We denote the photo-neutron yield (or production) cross section σ_{xn} as

$$\begin{aligned} \sigma_{xn} &= \sigma(\gamma, 1n) + \sigma(\gamma, np) + \sigma(\gamma, n\alpha) + \dots \\ &+ 2\sigma(\gamma, 2n) + 2\sigma(\gamma, 2np) + 2\sigma(\gamma, 2n\alpha) + \dots \\ &+ 3\sigma(\gamma, 3n) + 3\sigma(\gamma, 3np) + 3\sigma(\gamma, 3n\alpha) + \dots, \\ &= \sum_i i\sigma_{inX}, \end{aligned} \quad (2)$$

and the total photo-neutron cross section σ_{Sn} as

$$\begin{aligned} \sigma_{Sn} &= \sigma(\gamma, 1n) + \sigma(\gamma, np) + \sigma(\gamma, n\alpha) + \dots \\ &+ \sigma(\gamma, 2n) + \sigma(\gamma, 2np) + \sigma(\gamma, 2n\alpha) + \dots \\ &+ \sigma(\gamma, 3n) + \sigma(\gamma, 3np) + \sigma(\gamma, 3n\alpha) + \dots \\ &= \sum_i \sigma_{inX}. \end{aligned} \quad (3)$$

When the photo-charged particle reaction cross sections — $\sigma(\gamma, p)$, $\sigma(\gamma, \alpha)$, *etc.* — are negligible, and no photo-fission occurs, σ_{Sn} is the same as the photo-absorption cross section σ_{abs} . Otherwise, the sum of this cross section σ_{Sn} with the photo-charged-particle cross section will give the total photo-absorption cross section as

$$\begin{aligned} \sigma_{abs} &= \sigma_{Sn} + \sigma(\gamma, p) + \sigma(\gamma, 2p) + \dots + \\ &+ \sigma(\gamma, d) + \sigma(\gamma, dp) + \dots + \sigma(\gamma, \alpha) + \dots \end{aligned} \quad (4)$$

Usually σ_{xn} is explicitly given in the photonuclear data library as the neutron multiplicity, while σ_{Sn} is implicit. When the target photo-fissions, Eqs. (2) and (3) have an extra term;

$$\sigma_{xn} = \sigma(\gamma, n) + 2\sigma(\gamma, 2n) + \dots + \bar{\nu}\sigma(\gamma, f), \quad (5)$$

$$\sigma_{Sn} = \sigma(\gamma, n) + \sigma(\gamma, 2n) + \dots + \sigma(\gamma, f), \quad (6)$$

where $\bar{\nu}$ is the average number of neutrons per fission.

Varlamov *et al.* proposed an F_i value [12]

$$F_i = \frac{\sigma(\gamma, inX)}{\sigma(\gamma, xn)}, \quad (7)$$

to facilitate the assessment and evaluation of the experimental $\sigma(\gamma, inX)$ cross sections. F_i has a maximum value

for each i -neutron reaction channel: $F_1 < 1$ for $i = 1$, $F_2 < 1/2$ for $i = 2$, and $F_3 < 1/3$ for $i = 3$. When F_i exceeds these limits then there are issues in the measurement of $\sigma(\gamma, inx)$ data by the same group. Since the above-mentioned limits are automatically satisfied in the theoretical calculations, it is essential to apply a model-based approach in the evaluation of the available photonuclear experimental data to avoid such inconsistencies.

III. AVAILABLE EXPERIMENTAL DATA

The experimental photonuclear reaction data have been obtained in various types of measurements, with bremsstrahlung and quasi-monoenergetic photons from positron annihilation in flight and more recently from laser Compton scattering (LCS). While the photo-neutron yield cross sections are obtained by counting the total number of neutrons emitted, the determination of partial photo-neutron cross sections requires neutron-multiplicity sorting. Below we provide a brief description of the experimental procedures most frequently used in the past [3] and most recently developed.

A. Experiments

To determine the photonuclear reaction cross section, one needs to measure on an absolute scale both the flux of the incident photons and the number of reaction products. The incident photon flux can be determined directly with an ionization chamber, scintillator or solid-state detector or indirectly by normalizing to known reaction cross sections (for bremsstrahlung beams). The number of reaction products is determined either by counting the emitted particles or by measuring the activity of radioactive residual nuclei. We summarize the characteristics of various γ -ray sources and photonuclear cross sections measurements below.

1. Bremsstrahlung

Bremsstrahlung beams were used in the first measurements of photo-nuclear cross sections. The continuous bremsstrahlung spectra were produced by striking a radiator target with an electron beam from an accelerator (initially betatrons and synchrotrons, and later, linear accelerators). Several laboratories around the world (mostly in Russia, Canada and Australia) developed this type of photon beams.

As the spectrum of photon energies is continuous, only the yield of the reaction can be measured:

$$Y(E_0) = N_R \int_{E_{\text{th}}}^{E_0} \frac{\sigma(E_\gamma)}{E_\gamma} W(E_0, E_\gamma) dE_\gamma, \quad (8)$$

where E_γ is the photon energy, $\sigma(E_\gamma)$ is the reaction cross section, $W(E_0, E_\gamma)$ is the bremsstrahlung energy spectrum, E_0 is the end-point energy of the bremsstrahlung spectrum which is equal to the electron beam energy, E_{th} is the threshold energy, and N_R is the normalization coefficient. Changing E_0 by small steps allows one to measure a yield curve and then by applying an ‘‘unfolding’’ procedure to obtain the photo-nuclear reaction cross section.

Several unfolding methods for spectrum-averaged cross sections have been developed, among which the most widely used ones are:

- the Photon Difference Method [13] in which the difference of two bremsstrahlung spectra near the slightly differing end-point energies is interpreted as an almost quasi-monoenergetic spectrum; a modified version uses the linear combination of three bremsstrahlung spectra [14] which improves the shape of the resulting spectrum;
- the Penfold-Leiss method [15] in which the integral Eq. (8) is replaced by a set of linear equations for finite analysis bins; some modifications of this method [16] vary the analysis bin depending on the yield accuracy;
- the regularization method [17] in which the mean square difference between the reaction cross section and the model value is minimized assuming different approaches for smoothing the cross section; modifications of this method are based on various regularizers [18–20].

The typical apparatus functions (effective photon spectra) for these methods have different line shapes localized in photon energy though not close to a Gaussian line shape, allowing experimentalists to obtain the information on the reaction cross section at energy E_γ with energy resolution dependent on the data processing.

The advantage of bremsstrahlung measurements is the large photon beam intensity, which allows one to obtain reasonable counting statistics even for relatively small reaction cross sections. However, there are several disadvantages of using such a technique. First, one needs to know the bremsstrahlung spectrum sufficiently well for all electron energies. Second, measuring a reaction yield curve in small energy steps requires a stable accelerator and large counting statistics. Third, the process of subtracting the yield curves in the unfolding procedure may introduce correlations between the experimental data points that can lead to unphysical fluctuations in the unfolded cross sections.

2. Positron Annihilation in Flight

While the unfolding of the experimental reaction yield resulting from bremsstrahlung measurements may involve a ‘‘mathematical’’ method of obtaining the ‘‘quasi-monoenergetic’’ photons, positron annihilation in flight

offered an ‘‘apparatus method’’ of producing them with variable energies. The method [21] was realized in several laboratories around the world, mostly in LLNL (USA) and Saclay (France) [22]. An intense beam of high-energy electrons from a linear accelerator hits a thick high- Z converter and produces bremsstrahlung which undergoes electron-positron pair production in the converter. The fast positron beam then impinges on a thin, low- Z target and produces a bremsstrahlung spectrum and a peak of annihilation photons. The Livermore and Saclay facilities were nearly the same except that while in the Livermore system positrons from the converter were re-accelerated before undergoing annihilation, in the Saclay system the positrons were simply separated without re-acceleration.

To separate the bremsstrahlung component from the annihilation photons, this kind of measurement proceeded in the following three steps:

1. similar to the bremsstrahlung measurement, the reaction yield, $Y^+(E_0)$, is obtained with the γ -ray spectrum that consists of the positron annihilation and bremsstrahlung components. See Ref. [23] for the 15.6 MeV positrons on the 0.0060 in. thick LiH target. The peak energy of the annihilation γ -rays is given by $E_0 + 3mc^2/2$ with the kinetic energy of positrons E_0 and the electron rest mass energy mc^2 ;
2. the reaction yield $Y^-(E_0)$ is given by bremsstrahlung of electrons with the energy E_0 ; and
3. the reaction cross section is deduced as the difference between the positron and electron reaction yields assuming that the bremsstrahlung spectra from positrons and electrons are identical to first order approximation; the subtraction is supposedly subject to the stability of the accelerator parameters.

Hence the photonuclear cross section reads

$$\sigma(E_\gamma) = Y^+(E_0) - Y^-(E_0) . \quad (9)$$

The effective photon spectrum for this method is essentially the positron-annihilation line shape, which may be asymmetric with respect to the low-energy tail because of the subtraction procedure described above. The disadvantage of this method, as compared to bremsstrahlung, is the low intensity of the photon beam attributed to the small cross sections of the electron-positron pair production and positron annihilation processes.

3. Bremsstrahlung Tagging

As an alternative to the complex task of unfolding the reaction cross section from the experimental reaction yield by solving the inverse integral equation of Eq. (8), the method of producing (quasi)monoenergetic photons

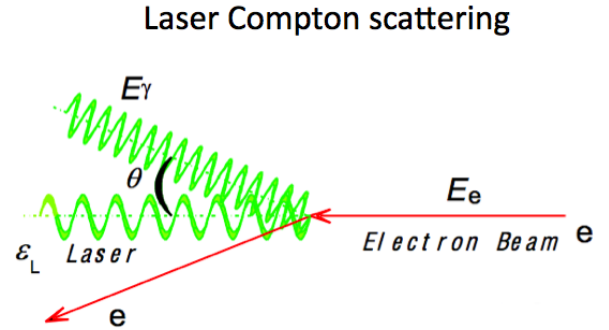


FIG. 1. (Color online) Laser Compton scattering of laser photons from relativistic electrons.

by tagging was proposed [24]. It was implemented at the University of Illinois (USA) using the beam from a high duty-cycle electron linear accelerator. The idea was to produce photons by letting electrons impinge on a very thin radiator with an energy E_0 and then to tag the photons with scattered electrons with an energy E_{scatt} . Thus, photons are tagged with an energy E_γ ,

$$E_\gamma = E_0 - E_{\text{scatt}} . \quad (10)$$

The scattered electron is deflected by the magnetic spectrometer to an array of detectors placed in its focal plane. The energy spread (resolution) of the photon beam depends on the number of detectors mounted in focal plane. A thin-sliced part of the bremsstrahlung spectrum represents the typical effective photon spectrum from this method, which is close to a Gaussian line shape. partial reaction cross sections were obtained using the tagged bremsstrahlung photons.

The disadvantage of this method is the low-intensity photon beam extracted from the very thin bremsstrahlung-producing radiator that makes coincidence measurements difficult.

4. Laser Compton-scattering

Following the development of high duty-cycle electron accelerators and high-power lasers, new quasi-monoenergetic γ -ray beams have been produced in collisions of laser photons with relativistic electrons which is referred to as laser Compton scattering (LCS) [25–28] as illustrated in Fig. 1. The LCS γ -ray beam-line of the NewSUBARU synchrotron radiation facility [28] is shown in Fig. 2. An electron beam at 1.0 GeV in nominal energy is injected from a linear accelerator to the storage ring and either decelerated to 0.5 GeV or accelerated to 1.5 GeV.

Pulse γ -ray beams are produced with Q-switch lasers; low-energy beams are produced typically at 20 kHz with

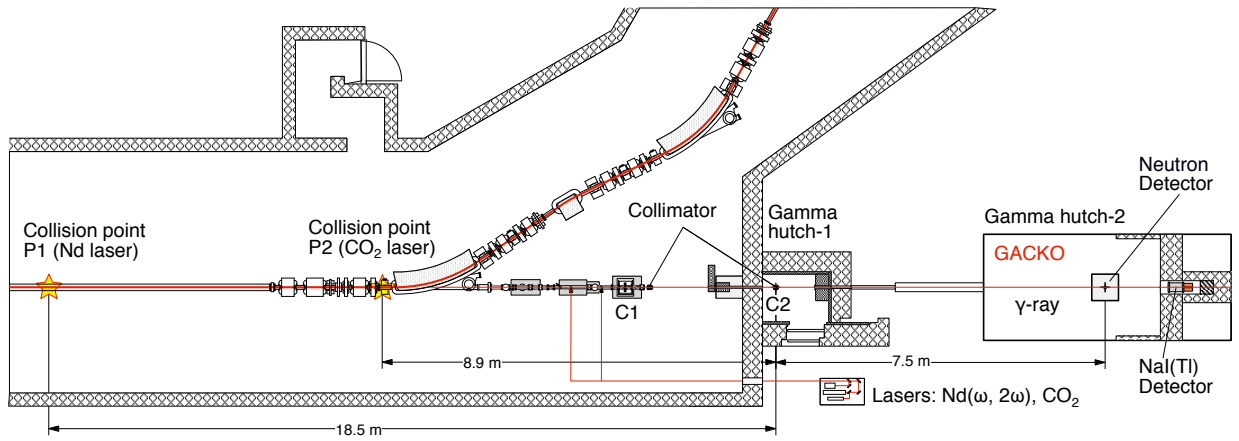


FIG. 2. (Color online) The γ -ray beam-line BL01 of the NewSUBARU synchrotron radiation facility.

the INAZUMA laser (1064 nm wavelength and 60 ns pulse width) for $(\gamma, 1n)$ cross section measurements below $(\gamma, 2n)$ threshold, while high-energy beams at 1 kHz with the Talon laser (532 nm, 40 ns) for partial cross section measurements above $(\gamma, 2n)$ threshold. The frequency and pulse width of the electron beam in the NewSUBARU storage ring are 500 MHz and 60 ps, respectively, so that the frequency and width of the γ -ray pulse are the same as those of the laser.

The electron beam energy has been calibrated with the accuracy of the order of 10^{-5} [29] by using low-energy LCS γ -ray beams produced with a grating-fixed CO_2 laser with the central wavelength of the P(20) master transition ($\lambda = 10.5915 \mu\text{m} \pm 3 \text{ \AA}$) with the bandwidth 1.3 \AA in the full width at half maximum. The γ -ray beam energy is determined from the calibrated electron beam energy.

The flux of pulsed γ -rays is determined with the pile-up or Poisson-fitting method [30–32]. Large numbers of laser photons and electrons are involved in the collision with a small probability of the laser Compton scattering. As a result, the number of photons involved in a γ -ray pulse follows the Poisson distribution [30]. Figure 3 shows an experimental multi-photon spectrum for 34-MeV γ -rays measured with a $8'' \times 12''$ NaI(Tl) detector along with the best-fit Poisson distribution. The average number of photons per γ -pulse is determined with the intrinsic accuracy less than 0.1% [32]. The γ -ray flux is determined with the experimental formula [31, 32] for a product ($m^{\text{exp}} \times N_{\gamma}^{\text{pulse}}$) of the average number,

$$m^{\text{exp}} = \frac{\langle N_m \rangle}{\langle N_s \rangle}, \quad (11)$$

and the number of γ -ray pulses

$$N_{\gamma}^{\text{pulse}} = \sum_i N_m(i), \quad (12)$$

where $N_m(i)$ and $N_s(i)$ are the number of photons at channel i in the multi- and single-photon spectra, respec-

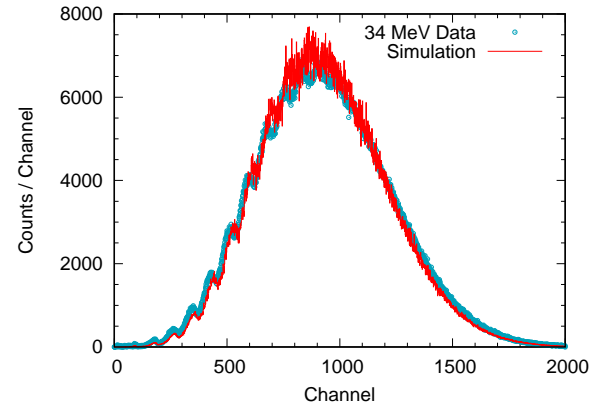


FIG. 3. (Color online) Experimental multi-photon spectrum at 34 MeV in comparison with the best-fit Poisson distribution.

tively, and $\langle N \rangle$ stands for their average channel number [32].

The energy-profile of the LCS γ -rays is determined by best reproducing response functions of an energy-profile monitor with a Monte Carlo code GEANT4 that incorporates the kinematics of the laser Compton scattering, transportation of LCS γ -rays through the collimators (C1 and C2) to the energy-profile monitor mounted in the experimental hutch GACKO (Gamma Collaboration hutch of KOnan university) in the γ -ray beam line of the NewSUBARU facility, and electromagnetic interactions of γ -rays inside the monitor detector. Figure 4 shows experimental γ -ray spectra for the 3 mm C1 and 2 mm C2 collimators measured with a $3.5'' \times 4.0''$ LaBr3(Ce) detector, best-fit Monte Carlo simulations, and incident γ -ray spectra at 6, 10, 20, 30 and 39 MeV. As shown in Fig. 4, the energy-profile of the LCS γ -rays produced at the NewSUBARU facility is characterized by a sharp cut-off at the maximum energy corresponding to the head-on

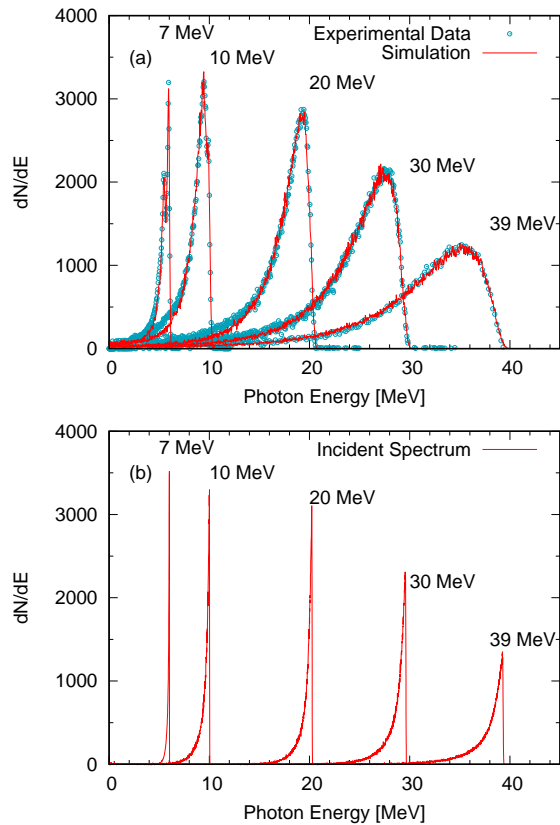


FIG. 4. (Color online) (a) Experimental and simulated response functions of a 3.5×4.0 '' LaBr₃(Ce) detector to LCS γ -ray beams, and (b) energy spectra of incident LCS γ -ray beams obtained by Monte Carlo simulations with the GEANT4 code. The energy spread is a few % in the full width at half maximum: 68, 247, 325, 578, and 965 keV for 6.0, 10, 20, 30, and 39 MeV LCS γ -ray beams, respectively.

collision and a low-energy tail with an energy spread determined by the electron beam divergence and the collimator size. The energy spread is a few % in the full width at half maximum.

The synchrotron radiation accompanies the LCS γ -rays as background which is considerably lower in both intensity and energy than the positron bremsstrahlung which accompanied the positron-annihilation-in-flight γ -rays. The laser was turned on and off at 10 Hz for 80 ms and 20 ms, respectively, to measure the background neutrons resulting from the synchrotron radiation.

B. Partial Reaction Measurement

One can determine the neutron yield cross section from the total number of neutrons detected using Eq. (2) virtually in all measurements with the different γ -ray sources summarized in Sec. III A. However, it is not straightforward at all to determine partial photoneutron cross sections, $(\gamma, 1n)$, $(\gamma, 2n)$, $(\gamma, 3n)$, *etc.* In this section, we de-

scribe how partial photoneutron cross sections are derived using the various measurement techniques, and then focus our discussions on the long-standing discrepancies between the Livermore and Saclay data and the new direct neutron-multiplicity sorting technique that was a major topic of the present CRP.

1. Bremsstrahlung

Since the effective photon spectrum is continuous, a special correction that is based on the statistical theory of nuclear reactions is applied to $\sigma(\gamma, xn)$ to obtain the total photo-neutron reaction cross section of Eq. (3). After the correction is applied, $(\gamma, 2n)$ and $(\gamma, 1n)$ cross sections below the $(\gamma, 3n)$ reaction threshold B_{3n} , can be obtained by subtraction as follows

$$\sigma(\gamma, 2n) = \sigma_{xn} - \sigma_{Sn}, \quad (13)$$

$$\sigma(\gamma, 1n) = \sigma_{Sn} - \sigma(\gamma, 2n), \quad (14)$$

$$\sigma(\gamma, 1n) = \sigma_{xn} - 2\sigma(\gamma, 2n). \quad (15)$$

2. Quasi-monoenergetic Annihilation Photons

Highly-efficient 4π neutron detectors for measuring multi-neutron coincidences and neutron multiplicity sorting techniques for separating partial reactions were developed in Livermore [22], Saclay, and other laboratories, to deal with the competition between various partial reactions $(\gamma, 1n)$, $(\gamma, 2n)$, $(\gamma, 3n)$, *etc.* over a wide range of energies.

Large arrays of $^{10}\text{BF}_3$ tubes embedded in a paraffin or polyethylene matrix in several concentric rings were used at Livermore. For example, the array of 48 $^{10}\text{BF}_3$ tubes in a paraffin moderator had a neutron detection efficiency of 45 – 30% in the energy range up to 5 MeV [33]. The ring-ratio technique was developed to determine the average neutron kinetic energy [33]. The ring-ratio, i.e. the ratio of the neutron count of the outer-ring detector to that of the inner-ring detector, is a monotonically-increasing function with neutron energy. It allows to distinguish, for example, between $(\gamma, 2n)$ and two $(\gamma, 1n)$ events. Thus, it became possible to directly determine/probe the total photo-neutron (Eq. (3)) and neutron yield (Eq. (2)) cross sections.

A large tank of Gd-loaded liquid scintillator was used at Saclay. The high neutron detection efficiency of over 90% that was achieved in the energy range up to 5 MeV allowed direct measurements of partial photoneutron reaction cross sections which were used to determine the total and neutron-yield cross sections, Eqs. (3) and (2), respectively. The discrimination of various partial reaction cross sections was more complex and less reliable with the Livermore detector than with the Saclay detector, even with the help of the ring-ratio technique. The reason was that the detection efficiency of the Livermore detector was lower and varied more with energy than that

of the Saclay detector. The Saclay detector, on the other hand, suffered from pile-up and background events as well as dead-time caused by a γ -flash from the target [22].

The results obtained at the two laboratories for the same nuclei show intricate discrepancies in magnitude not only for the total but for partial cross sections as well. For example, it was found [34–36] that, in general, the Saclay $(\gamma, 1n)$ cross sections are larger than the Livermore data, whereas the $(\gamma, 2n)$ cross sections are smaller than the corresponding Livermore data. This is discussed in detail in Sec. V A.

3. Bremsstrahlung Activation

A series of activation measurements was performed using high-intensity bremsstrahlung. The partial photoneutron reaction cross sections $(\gamma, 1n)$, $(\gamma, 2n)$, $(\gamma, 3n)$, *etc.* were determined by measuring the activity of the residual unstable nuclei.

After irradiating a target by bremsstrahlung with various end-point energies, γ -ray counting was carried out for residual nuclei. The γ -lines unique to residual nuclei were clearly identified in the γ -ray spectra measured with an energy- and efficiency-calibrated high-purity germanium (HPGe) detector [37–39]. Photonuclear reaction cross sections were deduced from the γ -lines.

4. Direct neutron-multiplicity sorting with a flat-efficiency detector

The partial photoneutron cross section $\sigma(\gamma, in)$ with neutron multiplicity $i = 1, 2, 3, \dots$ can typically be determined experimentally from the number of (γ, in) reactions N_i by

$$N_i = N_\gamma N_T \sigma(\gamma, in) , \quad (16)$$

where N_γ is the number of γ -rays incident on a target, and N_T is the number of target nuclei per unit area.

The problem with using Eq. (16) lies in the fact that N_i is not a direct experimental observable. The neutron detection efficiency of moderator-based neutron detectors depends on the neutron kinetic energy. The ring ratio technique [33] was developed at Livermore to determine the average neutron energy. However, this technique cannot be applied to N_i , but to the experimental observable, *i.e.* multi-neutron coincidence events. This may be a source of uncertainties associated with the Livermore partial photoneutron cross sections.

A novel technique [10] was developed to overcome the shortcomings of the neutron-multiplicity sorting of Livermore. This technique, referred to as direct neutron-multiplicity sorting with a flat-efficiency detector (FED), combined with the LCS γ -ray beam provides an experimental opportunity to obtain partial photoneutron cross sections with improved reliability.

In the case of neutron detection, for example, between $(\gamma, 3n)$ and $(\gamma, 4n)$ thresholds, using a pulsed γ -ray beam, j -fold events for single ($j = 1$), double ($j = 2$), and triple ($j = 3$) neutron coincidences are observed.

The single neutron event corresponds to observing only one neutron during the time interval of two successive γ -ray pulses. There are three contributions from $(\gamma, 1n)$, $(\gamma, 2n)$, and $(\gamma, 3n)$ reactions to the single neutron event as

$$\begin{aligned} N_s &= N_1 \varepsilon(E_1) \\ &+ N_2 {}_2C_1 \varepsilon(E_2) \{1 - \varepsilon(E_2)\} \\ &+ N_3 {}_3C_1 \varepsilon(E_3) \{1 - \varepsilon(E_2)\}^2 . \end{aligned} \quad (17)$$

The first term means simply that one neutron emitted in the $(\gamma, 1n)$ reaction is observed with detection efficiency $\varepsilon(E_1)$ for neutron kinetic energy E_1 . The second term means that one of two neutrons emitted in the $(\gamma, 2n)$ reaction is observed with detection efficiency $\varepsilon(E_2)$ for neutron kinetic energy E_2 and that the other neutron is not observed with unobserved efficiency $(1 - \varepsilon(E_2))$. The third term corresponds to the observation of one of three neutrons emitted in the $(\gamma, 3n)$ reaction. It is noted that there is no way to know E_1 , E_2 , and E_3 because the ring-ratio technique is applied to the experimental observable N_s , not to the number of reactions N_1 , N_2 , and N_3 , individually. Furthermore, the neutron kinetic energy depends on the emission order from an excited nucleus. Therefore, the second term of Eq. (17) should be written as

$$\begin{aligned} &N_2 {}_2C_1 \varepsilon(E_2) \{1 - \varepsilon(E_2)\} \\ &= N_2 \varepsilon(E_{21}) \{1 - \varepsilon(E_{22})\} \\ &+ N_2 \varepsilon(E_{22}) \{1 - \varepsilon(E_{21})\} , \end{aligned} \quad (18)$$

using kinetic energies E_{21} and E_{22} of the first neutron and second neutron emitted, respectively.

The concept of the novel technique is to make the detection efficiency independent of neutron kinetic energies. Thus, using a constant efficiency ε , we can rewrite Eq. (17) as

$$\begin{aligned} N_s &= N_1 \varepsilon \\ &+ N_2 {}_2C_1 \varepsilon(1 - \varepsilon) \\ &+ N_3 {}_3C_1 \varepsilon(1 - \varepsilon)^2 . \end{aligned} \quad (19)$$

Similarly, the double and triple neutron coincident events are written as

$$N_d = N_2 \varepsilon^2 + N_3 {}_3C_2 \varepsilon^2(1 - \varepsilon) , \quad (20)$$

and

$$N_t = N_3 \varepsilon^3 , \quad (21)$$

respectively.

One can solve the set of Eqs. (19) – (21) with known ε to obtain N_1 , N_2 , and N_3 from which then the partial cross sections $(\gamma, 1n)$, $(\gamma, 2n)$, and $(\gamma, 3n)$ are determined as in Eq. (16).

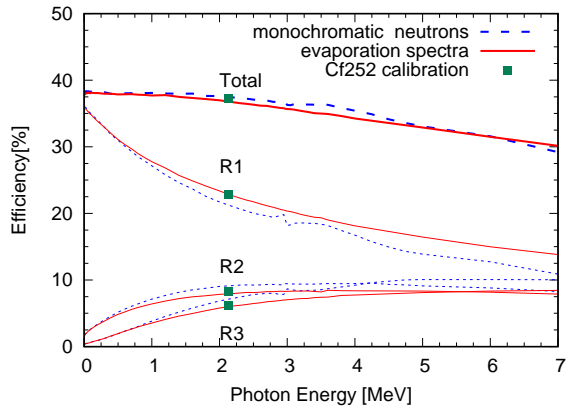


FIG. 5. The total detection efficiency and efficiencies of three rings.

The FED consists of three concentric rings of 4, 9, and 18 He counters embedded in a 46 cm (horizontally) \times 46 cm (vertically) \times 50 cm (along the beam axis) polyethylene moderator at the distances of 5.5, 13.0 and 16.0 cm from the γ -ray beam axis, respectively. The moderator is shielded by additional 5 cm-thick borated polyethylene plates for background neutron suppression. Figure 5 shows the total detection efficiency and efficiencies of the individual rings of the FED. Results of the calibration with a ^{252}Cf source are shown by the filled symbols. Results of the MCNP Monte Carlo simulations for monochromatic neutrons [10] are shown by the broken lines, while those for the neutron-evaporation spectra by the solid lines.

There are two issues that make the data reduction to obtain partial photoneutron cross sections rather complicated. First, double firings of photo-reactions can be induced by multi-photons involved in a single γ -ray pulse. For example, double firings of $(\gamma, 1n)$ reactions can be identified as a $(\gamma, 2n)$ reaction. Indeed, a small amount of non-zero $(\gamma, 2n)$ events attributable to such double firings was often observed below $(\gamma, 2n)$ threshold. Second, the electromagnetic interactions (pair production, Compton scattering, photo-electric absorption) of high-energy γ -rays in thick high- Z target material can generate secondary γ -rays which can induce the giant dipole resonance most effectively in the peak region which is mostly governed by the $(\gamma, 1n)$ channel. Thus, the secondary gamma rays produce extra neutrons which may mistakenly be assigned to reaction neutrons of the $(\gamma, 1n)$ channel associated with the primary gamma rays. Such effect was observed when a 10mm-thick ^{209}Bi target was irradiated with a 40 MeV LCS γ -ray beam.

The procedure of unfolding the photoneutron cross section which is convoluted with the energy distribution of the LCS γ -ray beam (Fig. 4) is rather straightforward because of the monochromaticity of the LCS γ -ray beam with low background. Previously, the Taylor expansion method [40] and the least-square fitting method [41] were developed. These methods were used to mostly deduce

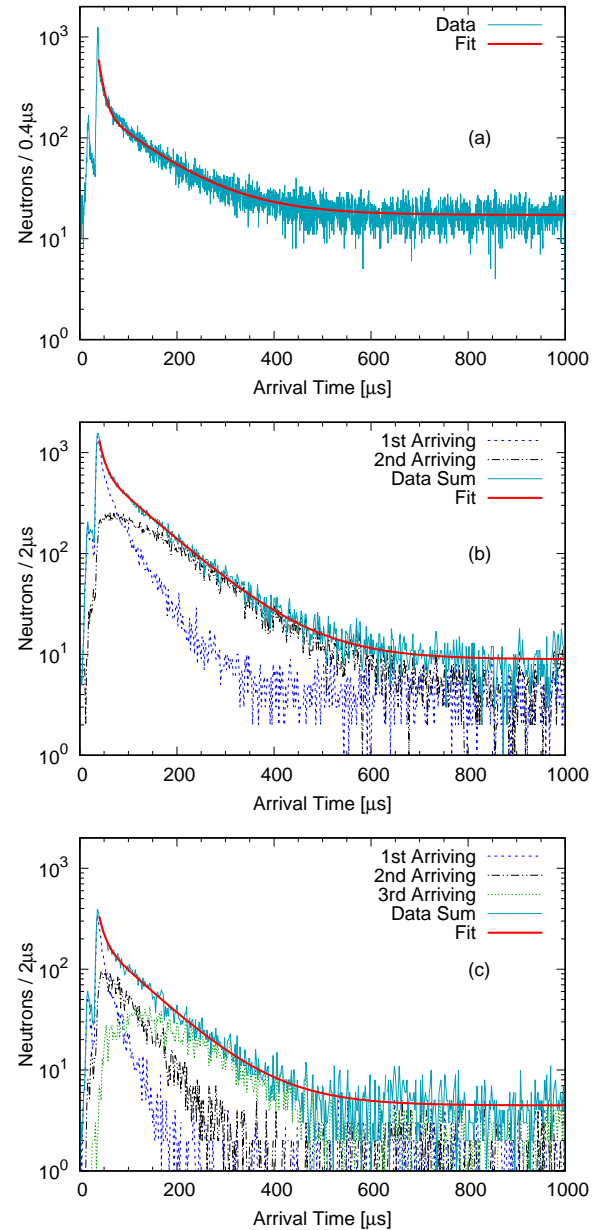


FIG. 6. (Color online) Neutron arrival-time distributions for (a) the single, (b) double, and (c) triple neutron events in the $^{209}\text{Bi}(\gamma, in)$ reactions at 34 MeV.

$(\gamma, 1n)$ cross sections at the average γ -ray energy below the $(\gamma, 2n)$ reaction threshold [42–45]. More recently, a new unfolding method has been developed [46] that deduces partial photoneutron cross sections at the maximum γ -ray energy corresponding to the maximum γ -ray yield (Fig. 4) over a wide energy range. The unfolded cross sections resulting from the Taylor expansion method and the new method were cross-checked in the case of ^{209}Bi [47] partial cross sections and were found to be in agreement.

C. Experimental Databases and Resources

1. Bibliographic Data

The list of photonuclear reaction bibliographies has remained unchanged since the publication of the previous IAEA Photonuclear Data Library in 2000 and can be found in Ref. [3]. The list includes mainly compilations of total and partial reaction cross sections for photo-induced disintegration and fission, photon absorption and scattering processes up to 1999. The list includes, for example, “photonuclear reactions,” 10th IAEA Bibliographical Series at IAEA [48], “Photonuclear data - abstract sheets 1955 – 1982,” at National Institute of Standards and Technology (NIST) [49], “Photonuclear data index 1976 – 1995,” at Centr Dannykh Fotoyadernykh Eksperimentov (CDFE) [50], and “Bibliographic Index to photonuclear reaction data (1955 – 1992)” at Japan Atomic Energy Research Institute (JAERI) [51]. More detailed information is given in Ref. [3]. These indices are available at CDFE [52].

2. Compilation of Photonuclear Cross Sections and GDR Parameters

The photonuclear cross sections and GDR parameters compiled prior to this CRP, have been reviewed in Ref [3]. Below we briefly summarize the important publications and the most recent compilation of GDR parameters performed within this CRP.

- Dietrich and Berman [2] published “Atlas of photoneutron cross sections obtained with monoenergetic photons,” which contains the photonuclear data measured with quasi-monoenergetic photons by annihilation in flight of fast positrons and by bremsstrahlung tagging;
- “Handbook on Nuclear Activation Data” compiled by Forkman and Petersson and published from IAEA [53];
- “Plots of the Experimental and Evaluated Photonuclear Cross-Sections” by Blokhon and Nasyrova [54] gives graphs of experimental and evaluated photoneutron reaction data for some selected nuclides;
- Varlamov *et al.* [55] published “Atlas of GDR,” which is a compilation of many photonuclear reaction data. This report covers all the reaction data compiled by Antonescu [48], and is given in the Annex of previous IAEA photonuclear data library report [3];
- the GDR parameters for heated atomic nuclei are determined from the γ -decay data. Compilation and parametrization of the GDR resonances built on excited states are given by Schiller and Thoennessen [56]; and

- the most recent comprehensive databases of the GDR parameters with their uncertainties from ground-state photo-absorption are compiled by Plujko *et al.* [8, 57].

In the recent databases [8, 57], Plujko *et al.* applied the least-squares technique to the updated experimental databases to obtain the GDR parameters and their uncertainties. The theoretical photo-absorption cross section, which is fitted to the experimental data, consists of both the GDR component with the SLO and SMLO models [58] and the QD contribution, which are given later. These databases [8, 57] were constructed based on the experimental data reported before Jan. 2010 and June 2017, respectively. Further updated GDR parameter tables, where the data published before Dec. 2018 are involved, are given in Appendix B.

3. EXFOR Database

The EXFOR database [9, 59], maintained by the international network of Nuclear Reaction Data Centers (NRDC) [60], is the main foundation for producing evaluated nuclear data libraries nowadays. The database as well as the Web data retrieval system [61] facilitates access to published experimental data in a computer-readable format.

IV. NUCLEAR MODELS AND CODES

A. Theory for Photonuclear Reactions

1. Photo-Absorption Cross Section

To calculate and evaluate the photonuclear reaction cross sections in the 1 – 200 MeV photon energy range, we adopt the independent hypothesis of a compound nucleus (CN) reaction, namely that the decay of the CN is independent of how it is formed, whereas the energy, spin, and parity are conserved. A photon is absorbed by a nucleus through two distinct nuclear reaction mechanisms; the Giant Dipole Resonance (GDR) and the quasi-deuteron (QD) photo-absorption process [62, 63]. While GDR is the dominant process in the energy range of typical photonuclear data applications ($E_\gamma = 10 \sim 20$ MeV), the QD model describes the photo-absorption mechanism for $E_\gamma > 30$ MeV or so. The experimentally observed photo-absorption cross section σ_{abs} includes both of these mechanisms

$$\sigma_{\text{abs}}(E_\gamma) = \sigma_{\text{GDR}}(E_\gamma) + \sigma_{\text{QD}}(E_\gamma), \quad (22)$$

where σ_{GDR} and σ_{QD} are the absorption cross sections for the GDR and QD mechanism, respectively.

We often apply a phenomenological parameterization to describe the GDR part of the photonuclear reaction

cross sections. Several models can be used to represent the measured absorption cross section σ_{GDR} , such as Lorentzian, Breit-Wigner or Gaussian functions. However the most simple and suitable function that has been confirmed by experimental photo-absorption data [22] is a Lorentzian shape of

$$\sigma_{\text{GDR}}(E_\gamma) = \sigma_R \frac{E_\gamma^2 \Gamma_R^2}{(E_R^2 - E_\gamma^2)^2 + E_\gamma^2 \Gamma_R^2}, \quad (23)$$

where σ_R is the GDR peak cross section, E_R is the resonance energy, and Γ_R is the width. In the case of deformed nuclei, the GDR peak splits into two, where each corresponds to the major or minor axis of ellipsoid, and the photo-absorption cross section is given by the sum of two GDRs. This is often called as the Standard Lorentzian (SLO) model for the photon strength function [58], which is also known as the Brink-Axel Lorentzian.

While the standard Lorentzian (SLO) parameterization of Eq. (23) is adequate to describe GDR around the peak, it fails to reproduce the data at lower energies around the neutron separation energy. Modified versions of the SLO, such as the generalized Lorentzian [64–66] and the Simple Modified Lorentzian (SMLO) [8, 57] were developed to account for data both at the GDR peak and at lower energies around the neutron separation energies. In addition to the phenomenological GDR models, significant effort has been devoted to developing more microscopic approaches such as the quasiparticle random phase approximation for the description of giant multipole resonances [67, 68] and even the shell model has been applied to electromagnetic excitations of light nuclei (see Ref. [11] for an overview).

For the purpose of updating the photonuclear evaluations in the IAEA Photonuclear Data Library, the SLO, SMLO and GLO models available in RIPL [58] were used to describe the GDR cross sections. The GDR parameters of these models have been fitted to available experimental data, and the systematic behavior of these parameters, as a function of Z and A numbers, E_γ , and/or nuclear deformation, has been extracted [58, 69]. When we assume the multipolarity of E1 is the largest contribution to the photo-absorption, the formed CN state will have the spin J of $|I - 1| \leq J \leq I + 1$, where I is the target nucleus spin, and the parity flips. This will be the initial configuration in the statistical model calculation.

The QD model of Chadwick *et al.* [70] is commonly implemented in the model codes we employ, where the so-called Levinger constant L is taken to be 6.5. This is a scaling constant that has been adjusted to the experimental photo-absorption cross section σ_{QD} by [70], and is seldom fine-tuned in practical calculations. The model reads

$$\sigma_{\text{QD}} = L \frac{NZ}{A} \sigma_d p_b, \quad (24)$$

where the photo-disintegration cross section σ_d is param-

eterized as

$$\sigma_d = \begin{cases} 61.2(E_\gamma - B_d)^{3/2} E_\gamma^{-3} \text{ mb} & E_\gamma > B_d \\ 0 & \text{otherwise} \end{cases}, \quad (25)$$

where the energies are in MeV, and B_d is the deuteron binding energy (2.22452 MeV). In the energy range $20 \leq E_\gamma \leq 140$ MeV, the Pauli blocking factor P_b is given by a polynomial;

$$P_b = 0.083714 - 0.0098343 E_\gamma + 4.1222 \times 10^{-4} E_\gamma^2 - 3.4762 \times 10^{-6} E_\gamma^3 + 9.3537 \times 10^{-9} E_\gamma^4, \quad (26)$$

and it is extrapolated to the outside as

$$P_b = \begin{cases} \exp(-73.3/E_\gamma) & E_\gamma < 20 \text{ MeV} \\ \exp(-24.2348/E_\gamma) & E_\gamma > 140 \text{ MeV} \end{cases}. \quad (27)$$

Assuming the QD component is negligible in the GDR energy range, the determination of the GDR parameters σ_R , E_R , and Γ_R can be performed by taking $\sigma_{\text{abs}} \simeq \sigma_{\text{GDR}}$.

2. Pre-Equilibrium Particle Emission

Nucleon or composite particle emission during the pre-equilibrium process has not been studied extensively for photonuclear reactions. In the GDR photo-absorption mechanism, the initial nuclear excitation can be interpreted as a superposition of particle-hole excitations in the shell model space, whereby the $1p$ - $1h$ configuration initiates the pre-equilibrium chain in the \mathcal{Q} -space as classified in the theory of Feshbach, Kerman, and Koonin [71], and eventually one nucleon is scattered into the \mathcal{P} -space. The QD model directly leads to the pre-equilibrium chain by creating the $2p$ - $2h$ configuration.

However, the nuclear reaction codes that were employed to create the photonuclear data library — EMPIRE [72, 73], TALYS [74], CCONE [75], and CoH₃ [76] — have implemented relatively simple pre-equilibrium models for photonuclear reactions. In some cases, the exciton model for a neutron-induced reaction is considered as a surrogate for the photo-induced precompound process, and the initial configuration of $1p$ - $0h$ or $2p$ - $1h$ is assumed.

The pre-equilibrium process implemented in CoH₃ is different from the other codes. A fraction of the pre-equilibrium process in the GDR absorption is restricted to the bound $1p$ - $1h$ configuration

$$\sigma_a^{\text{PE}} = R \sigma_{\text{GDR}}, \quad (28)$$

$$R = \frac{\omega_B(1p, 1h)}{\omega(1p, 1h)} \simeq \frac{S_n}{E_\gamma - \Delta}, \quad (29)$$

where S_n is the neutron separation energy, Δ is the pairing energy, ω is the $1p$ - $1h$ state density, while ω_B is $1p$ - $1h$ but with all particles in the bound state. When we insert the state density of Williams' [77] for ω , and Betak

and Dobes [78] for ω_B , the right-hand-side of Eq. (29) becomes simply $S_n/(E_\gamma - \Delta)$. This is analogous to a correction factor in the multi-step compound strength [79, 80]. The QD process creates a $2p-2h$ initial configuration, and CoH₃ makes $1p-1h$ configuration in both the neutron and proton shells. On the other hand, the GDR $1p-1h$ is created in the neutron shell. Because we have two different initial configurations, CoH₃ calculates the pre-equilibrium process twice and sums the results.

To illustrate the impact on the pre-equilibrium calculations of the different treatment of the initial configuration as well as the pre-equilibrium damping factor in Eq. (29), we calculate the $(\gamma, 1n)$ and $(\gamma, 2n)$ cross sections of ¹⁸¹Ta with the initial configuration of $1p-0h$, $1p-1h$, and $2p-1h$. The results are shown by the ratio to the CoH₃ default calculation, which is the $1p-1h$ for GDR and $2p-2h$ for QD, in Fig. 7. Because $\sigma_{\text{abs}} \simeq \sigma_{\text{QD}}$ above 20 MeV, the difference increases rapidly as the photon energy increases. However, at these higher energies we are comparing very small cross sections obtained from Eq. (24). The uncertainty in σ_{QD} could be comparable to the pre-equilibrium model deficiency.

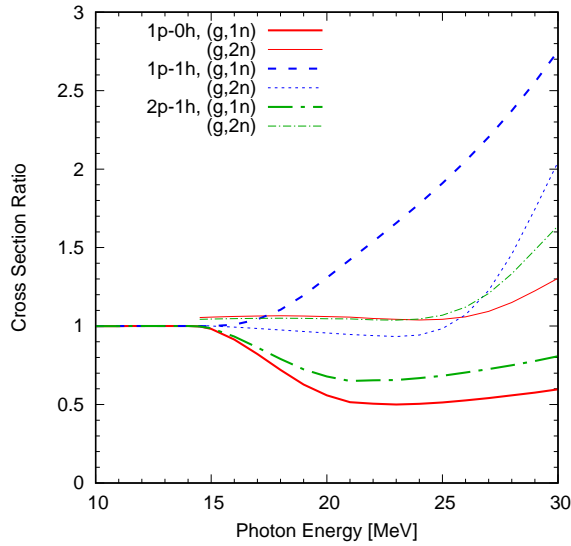


FIG. 7. (Color online) Calculated ¹⁸¹Ta(γ, n) and $(\gamma, 2n)$ cross section when the initial exciton configuration is $1p-0h$ (solid), $1p-1h$ (dashed), and $2p-1h$ (dot-dashed). The calculated cross sections are shown by the ratios to the CoH₃ default calculation.

3. Decay of Compound Nucleus

The decay of the CN state formed by the photo-absorption reaction is treated in the usual Hauser-Feshbach model [81], the only difference being the relatively narrow distribution of compound nucleus J compared to the particle-induced CN reactions. We define a population $P(E_x, J, \Pi)$ at the excitation energy of E_x ,

which is formed by the incoming photon $E_\gamma = E_x$, and is normalized to $\sigma_{\text{abs}}(E_\gamma)$ as

$$\sigma_{\text{abs}}(E_\gamma) = \sum_{J, \Pi} P(E_x, J, \Pi). \quad (30)$$

The decay of the CN state (E_x, J, Π) into a final outgoing channel is governed by the branching ratio for that channel which is calculated using the particle and γ -ray transmission coefficients. For a nucleon or a composite particle, the transmission coefficient is denoted by $T_{lj}(\epsilon)$, where l is the orbital angular momentum, spin j , and the center-of-mass energy ϵ . The transmission coefficient for the γ -ray emission is specified by the multipolarity XL , where $X = E$ or M . Hereafter we drop Π since the parity conservation is trivial.

To simplify, we consider a case where no charged particles are emitted, and all the final states are in the continuum. A population of (E'_x, J') formed after the γ -ray transition is written as

$$P(E'_x, J') = \frac{P(E_x, J)}{N} \sum_{XL} T_{XL}(E_\gamma) \times \rho_0(E'_x, J') dE, \quad (31)$$

$$E_\gamma = E_x - E'_x, \quad (32)$$

where N is the normalization shown later, $\rho_0(E, J)$ is the level density of the same nucleus as the target, and $|J - J'| \leq L \leq J + J'$ is fulfilled in the summation. When a neutron is emitted, the population of (E'_x, J') in the $(Z, A - 1)$ nucleus is

$$P(E'_x, J') = \frac{P(E_x, J)}{N} \sum_{lj} T_{lj}(E_n) \times \rho_1(E'_x, J') dE, \quad (33)$$

$$E_n = E_x - E'_x - S_n, \quad (34)$$

where S_n is the neutron separation energy, the level density $\rho_1(E'_x, J')$ is for the residual $(Z, A - 1)$, and the triangular relation reads $|J - J'| \leq j \leq J + J'$. The normalization factor N is given by integrating all the possible final states

$$N = \int_0^{E_x} \sum_{XL} T_{XL}(E_\gamma) \rho_0(E'_x, J') dE + \int_0^{E_x - S_n} \sum_{lj} T_{lj}(E_n) \rho_1(E'_x, J') dE. \quad (35)$$

The neutron transmission coefficient T_{lj} is obtained by solving the Schrödinger equation for a complex one-body (optical) potential. The γ -ray transmission coefficients are calculated from the photon-strength function $f_{XL}(\epsilon)$ for the γ -decay as

$$T_{XL}(\epsilon) = 2\pi\epsilon^{2L+1} f_{XL}(\epsilon). \quad (36)$$

When the final state is in the discrete part of the level scheme, the integration in Eq. (35) is replaced by

a proper summation over branching ratios to these discrete levels which are often taken from the nuclear structure database [58]. An extension of these formulas to the case where charged-particle channels are involved should be straightforward. These calculations are repeated until the initial excitation energy E_x is exhausted by the emitted particle and γ -ray energies, as well as the particle binding energies.

4. Energy and Angular Distributions of Secondary Particles

The secondary particle energy and angular distributions are less known experimentally, hence this type of information relies strongly on the nuclear reaction models that are used to calculate the cross sections. The angle-integrated particle emission spectra consists of two components — the pre-equilibrium contribution and the evaporation component. Many of the reaction codes employ the exciton model and the Hauser-Feshbach statistical model to calculate the angle-integrated energy spectra. As mentioned above, different pre-equilibrium exciton models are implemented in the codes, therefore the hardness of the calculated energy spectra can be different. These differences are not expected to be significant, however, since the most important energy range is near GDR, where the CN decay dominates giving an isotropic evaporation spectrum and all the codes describe this part similarly.

A forward-peaked angular distribution is expected at higher incident photon energies due to the pre-equilibrium process. This is not so extensively studied for the photo-induced reaction case, and there is no general description for the evaluation of the angular distribution. A practical workaround [82], which was also applied to the previous IAEA photonuclear data library, is to emulate the neutron-induced reaction, and adopt the double-differential data systematics by Kalbach [83].

5. Model Parameters in Photonuclear Reaction Calculation

As mentioned in the previous section, there are some differences in the pre-equilibrium models implemented in the nuclear reaction codes that have been employed to evaluate the photonuclear reaction cross sections. These differences are, however, notable in the high energy region only. The dominant photonuclear reaction part is in the GDR energy range, and the differences in the model calculations mainly come from the Hauser-Feshbach model parameters. These parameters include the neutron and charged-particle optical potentials, the level density, and the γ -ray strength function. When the photo-absorption cross section is estimated within the reaction code itself, the built-in GDR parameter library can also be a source of difference between the various calculations. The global optical potential of Koning and Delaroche [84] is widely used in these type of calculations, therefore the differ-

ences in the calculations are mostly due to the level density models. Furthermore, the probability of γ -ray emission is much smaller than particle emission, so differences among the γ -ray strength functions have a very modest impact on the photonuclear reaction calculations.

B. Nuclear Reaction Codes for Photonuclear Data Evaluation

Since it is almost impossible to obtain complete information for photonuclear reactions from experiments only, the nuclear reaction codes play a significant role in creating the evaluated data library. For example, the only possible way to generate the evaluated energy and angular distributions of the emitted particle is to use the model calculations, which, of course, should consistently describe the available cross section data. In the previous release of the IAEA photonuclear data library [3], the evaluation was done using several reaction model codes available at the participating institutes: GNASH [85, 86] at LANL and KAERI, ALICE-F [87] and MCPHOTO [88] at JAERI, GUNF [89] and GLUNF [90] at CIAE, and XGFISS [91] at IPPE.

The modern Hauser-Feshbach nuclear reaction codes, EMPIRE [72, 73], TALYS [74], CCONE [75], and CoH₃ [76], which are often utilized for nucleon-induced reaction calculations, are also capable of calculating photo-induced reaction cross sections. As a result, they are widely used in the evaluation of general purpose nuclear data libraries, and are combined with the advanced-capabilities utility codes to create ENDF-6 format data files. Albeit these codes are built on common well-established nuclear reaction models to describe the various reaction mechanisms, the implementation of the nuclear reaction models in each code may give rise to differences in the calculated results which are inherent to the code and do not depend on the model or model parameters. It is therefore important to understand the characteristics of each code before comparing evaluations performed with the codes. Recently, an inter-comparison of the codes EMPIRE, TALYS, CCONE, and CoH₃ was performed for neutron-induced reactions on actinides [92] by fixing all the input parameters as consistently as possible, so that any observed difference would be due to the model implementation. It was concluded that in terms of model implementation, the implementation of the width fluctuation correction might give rise to differences in the calculated cross sections by up to $\approx 15\%$. The ambiguity related to the width fluctuation correction is not expected to affect the photonuclear reaction case, since the (γ, n) channel is much larger than the photon elastic scattering (the elastic enhancement does not impact (γ, n) [93].) However, as already discussed in Sec. IV A, the pre-equilibrium models employed in the different codes are different therefore the pre-equilibrium component is one of the sources of ambiguity among the codes.

The newly evaluated photonuclear data were produced with the codes EMPIRE, TALYS, CCONE, and MEND-G [94]. Some data files were produced with ALICE-F as was the case in the previous IAEA photonuclear data library. CoH₃ has not been used to produce any evaluations, since it focuses mainly on low-energy nuclear reactions. However, CoH₃ has been considered in the code comparison. The CPNRM (Combined Photonuclear Reaction Model) code [95, 96] developed at SINP/MSU is also included in the code comparison as it has been used extensively to correct the experimental data as described in Sec. V A.

1. Special notes on each model code

As described in Sec. IV A, photonuclear reaction calculations consist of three stages, the photo-absorption process, the pre-equilibrium particle emission, and the statistical Hauser-Feshbach decay. The absorption cross section is unambiguously determined by providing a set of GDR parameters (energy, width and peak cross section) using a standard Lorentzian or variants such as the Generalized Lorentzian or Simple Modified Lorentzian. Alternatively the absorption cross section can be pre-calculated and stored in an external file.

For the pre-equilibrium emission component, the codes adopt the one-component or two-component exciton model, however the initial particle-hole configuration used in each code may be different. CoH₃ assumes the initial configuration is $1p-1h$ created in the neutron shell for GDR, and $2p-2h$ ($1p-1h$ in both neutron and proton shells) for the QD process. It also includes the damping factor of Eq. (29). EMPIRE begins the calculation with $1p-0h$, unless specified otherwise. TALYS also assumes $1p-0h$. When the two-component exciton model is selected, the particle-hole pair is given in the neutron shell. In MEND-G, $2p-2h$ is the initial configuration for the QD contribution. CCONE assumes $1p-0h$ as the initial configuration. The particle-hole pair in the two-component model is given in the neutron shell for photo-reaction.

In the statistical decay stage, the particle transmission coefficients are calculated using an optical potential. Table I summarizes the optical potentials employed in each code for the evaluation. Since often the potential parameters are adjusted to better reproduce experimental data, we provide a default set of potentials when not specified. CoH₃ does not offer a default option for the potential. However, those given in the table are typical choices for the photonuclear reaction calculations.

2. Photonuclear reaction code inter-comparison

The F_i values in Eq. (7) were calculated with CPNRM, TALYS, CCONE, CoH₃, EMPIRE, and MEND-G, for the photo-induced reactions on ¹⁸¹Ta. We chose all default model parameters in each code. The results are

TABLE I. Optical potential used in the photonuclear cross section calculations. The abbreviations are, KD03 (Koning and Delaroche [84]), KD03-f (folding KD03 potential by technique of Watanabe [97]) AV94 (Avrigneanu *et al.* [98]), AV09 (Avrigneanu *et al.* [99]), AV10 (Avrigneanu *et al.* [100]), AV14 (Avrigneanu *et al.* [101]), AC06 (An and Cai [102]), BO88 (Bjowald *et al.* [103]), BG69 (Becchetti and Greenlees) [104, 105] HA06 (Han *et al.* [106]) XU11 (Xu *et al.*) [107]

	n	p	α	d	t	³ He
EMPIRE	KD03	KD03	AV94	AC06	BG69	BG69
TALYS	KD03	KD03	AV14	KD03-f	KD03-f	KD03-f
CCONE	KD03	KD03	AV10	HA06	KD03-f	XU11
MEND-G	KD03	KD03	BG69	BG69	BG69	BG69
CoH ₃	KD03	KD03	AV09	BO88	BG69	BG69

shown in Fig. 8, together with the evaluated experimental data by Varlamov *et al.* [108]. Large discrepancies amongst the model codes are seen in the high energy region, where pre-equilibrium emission is the dominant process, yet it should be noted that the cross sections in this region are tiny compared to GDR. In general, CPNRM gives the largest pre-equilibrium contribution, while the pre-equilibrium component of CoH₃ is the weakest. This is understood as a result of applying the correction factor of Eq. (29) in CoH₃. The F_1 and F_2 values by CPNRM increase above 30 MeV, which is not seen in the other codes.

From Fig. 8 it is clear that not only do the codes give different values of F_i , but that these differences vary with energy. The theoretical F_i values are determined by the competition between the neutron and the γ -ray emissions in the statistical decay of CN. Obviously they depend on the neutron and γ -ray transmission coefficients, as well as the level density of the final states. The conclusion is that if the theoretical F_i s are used to correct problematic or inconsistent experimental data, as proposed in Sec. V A, then the uncertainties in F_i due to different codes and model parameters need to be considered. Moreover, since these uncertainties are shown to vary with energy, the introduction of an overall constant uncertainty may not be adequate.

V. EVALUATION

The new evaluations for the updated Photonuclear Data Library were performed at five institutes: SINP/MSU (Skobeltsyn Institute of Nuclear Physics, Lomonosov Moscow State University), NDC/KAERI (Nuclear Data Center, Korean Atomic Energy Research Institute), IFIN-HH (Horia Hulubei National Institute for Physics and Nuclear Engineering), NDC/JAEA (Nuclear Data Center, Japan Atomic Energy Agency), and CNDC/CIAE (China Nuclear Data Center, China Institute of Atomic Energy). In the following sections, a summary of the evaluation procedure, adoption of experimen-

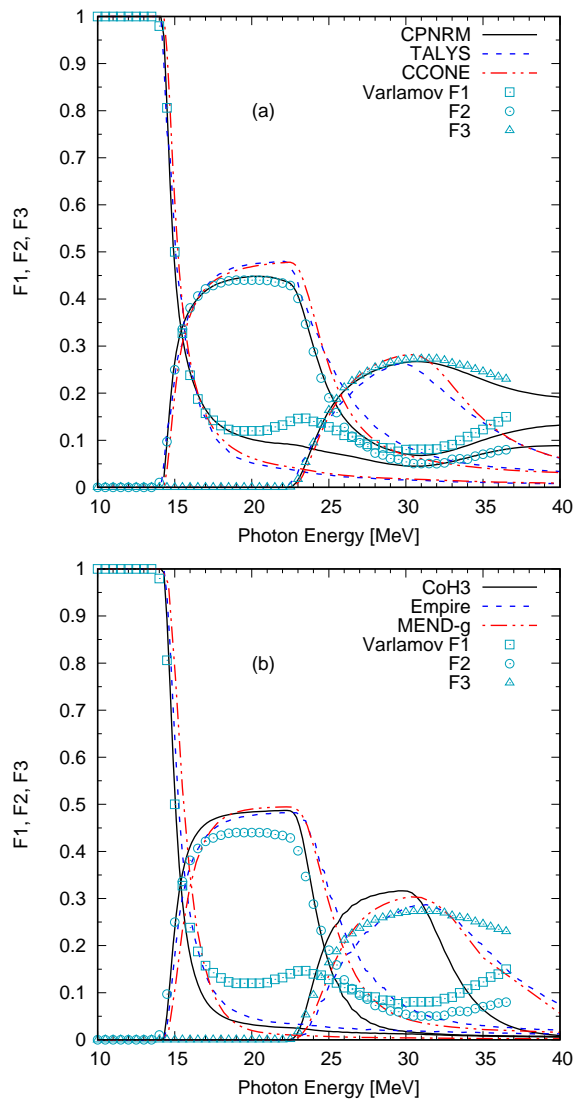


FIG. 8. (Color online) Calculated F_i values for $^{181}\text{Ta}(\gamma, inx)$ cross sections with (a) CPNRM, TALYS, and CCONE, and (b) CoH3, EMPIRE, and Mend-g. The symbols are evaluated experimental data by Varlamov *et al.*

tal data, and models used by each institute is given along with highlights of the resulting evaluations. The complete list of evaluations with graphical comparisons will be made available from an IAEA web interface.

A. Evaluation of Experimental Data

The majority of available experimental total and partial photo-neutron reaction cross sections were obtained by the quasi-monoenergetic annihilation photon beam and the photo-neutron multiplicity sorting technique at Livermore and Saclay [1, 2, 22]. Significant systematic disagreements in the experimental $(\gamma, 1n)$ and $(\gamma, 2n)$

data from these two institutes have been reported for 19 nuclei [35, 109, 110]: ^{51}V , ^{75}As , ^{89}Y , ^{90}Zr , ^{115}In , $^{116,117,118,120,124}\text{Sn}$, ^{127}I , ^{159}Tb , ^{181}Ta , ^{197}Au , ^{208}Pb , ^{232}Th , and ^{238}U . It was found that the $(\gamma, 1n)$ cross sections from Saclay tend to be larger than the Livermore data by up to 100%, while Livermore gives larger $(\gamma, 2n)$ cross sections by up to 100%. An average overall estimate of the differences is given by the ratio of the experimental integrated cross section from Saclay $\sigma_{\text{S,L}}^{\text{int}}$ to that from Livermore $\sigma_{\text{L}}^{\text{int}}$. The experimental integrated cross sections are obtained from

$$\sigma_{\text{S,L}}^{\text{int}} = \int_{E_{\text{th}}}^{E_{\text{max}}} \sigma_{\text{S,L}}(E) dE, \quad (37)$$

where E_{th} is the threshold energy of $1n$ or $2n$ reaction and E_{max} is the highest photon energy in the experiments. The average value $\langle \sigma_{\text{S}}^{\text{int}} / \sigma_{\text{L}}^{\text{int}} \rangle$ is found to be 1.07 for the $(\gamma, 1n)$ reaction, and 0.84 for the $(\gamma, 2n)$ reaction. The ratio $\sigma_{\text{S}}^{\text{int}} / \sigma_{\text{L}}^{\text{int}}$ fluctuates considerably between 0.76 and 1.34 for the $(\gamma, 1n)$ cross section and between 0.71 and 1.22 for all the 19 nuclei mentioned above. Given the large fluctuations in $\sigma_{\text{S}}^{\text{int}} / \sigma_{\text{L}}^{\text{int}}$, the discrepancies between the Livermore and Saclay data cannot be rectified by simply applying a constant normalization factor common to all the 19 nuclei.

On the other hand, the neutron yield cross-section data from these two institutes (Eq. (2)) also disagree by up to 10% on average [110]. This implies that the systematic inconsistency observed in the measured partial reaction cross sections may be due to a shortcoming of the neutron multiplicity sorting method. In order to understand the underlying systematic uncertainties in the experimental data, Varlamov *et al.* [12] introduced the F_i function of Eq. (7), which provides objective criteria for assessing the consistency and reliability of the experimental partial reaction cross-sections obtained in a given measurement, and allows one to investigate the systematic uncertainties. As has been mentioned in Sec. II, since F_1 is defined as the ratio of $\sigma(\gamma, 1n)$ to the photo-neutron yield cross section $\sigma(\gamma, xn)$, it can never be larger than 1; analogously F_2 cannot exceed $1/2$, F_3 cannot exceed $1/3$, and so on. In addition, F_i should always be positive. These constraints on $F_i(E)$ values allow one to identify a potential problem in the way the neutron yield cross section has been partitioned into the individual one, two, three, or even more neutron emission components.

Varlamov *et al.* [12] has shown that the constraints imposed by F_i are not satisfied in many cases [12, 108–115]. The problematic experimental data, where negative cross-sections are reported, include the measurements of photo-neutron reactions on ^{80}Se , $^{91,94}\text{Zr}$, ^{115}In , $^{112-124}\text{Sn}$, ^{133}Cs , ^{138}Ba , ^{159}Tb , ^{181}Ta , $^{186-192}\text{Os}$, ^{197}Au , ^{208}Pb , ^{209}Bi , and some others. In these cases, the corresponding F_1^{exp} values and/or F_2^{exp} values are found to be larger than the aforementioned upper limits, or negative as well. A typical example of the energy dependent $F_i^{\text{exp}}(E)$ values for ^{65}Cu [116] is given in Fig. 9, where it is compared with the theoretical $F_i^{\text{th}}(E)$ curves [114]

obtained for partial reactions (γ, in) with $i = 1$ and 2 within the framework of the CPNRM code [95, 96].

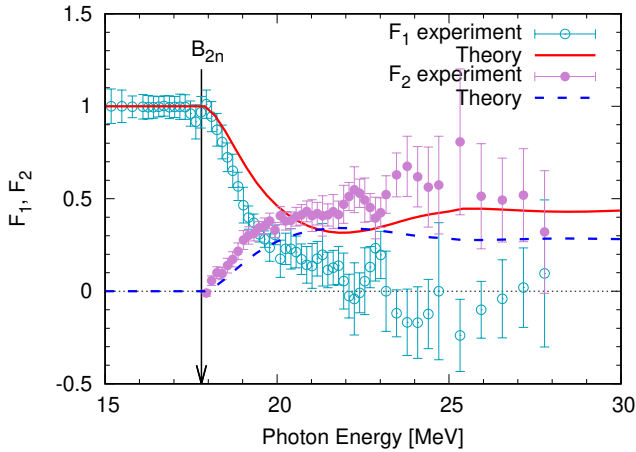


FIG. 9. (Color online) Comparison of the ratios F_i^{exp} [114] using the experimental data (triangles; Ref. [116]) and the theoretical F_i^{th} functions for ^{65}Cu

The partial photo-neutron reactions cross sections should be evaluated under the condition that the inherent issues in the neutron multiplicity sorting method as well as the limitations of the statistical model do not form a bias. In other words, the systematic experimental uncertainties as well as model-dependent uncertainties need to be considered in the evaluation. The evaluation method proposed by Varlamov *et al.* [12], combines the experimental photo-neutron yield data $\sigma^{\text{exp}}(\gamma, xn)$ (Eq. (2)) and the theoretical estimate of F_i^{th} obtained with the CPNRM code [95, 96] and is applicable to nuclei in the medium to heavy mass range. In this method, the physical reliability criteria mentioned above are automatically satisfied because the competition between the partial reaction cross sections is imposed by the model calculations performed with the CPNRM code. The evaluated partial photo-neutron reaction cross section $\sigma^{\text{eval}}(\gamma, in)$ is obtained by multiplying the experimental photo-neutron yield cross section $\sigma^{\text{exp}}(\gamma, xn)$ given in Eq. (2) by the theoretical F_i^{th} functions computed with the CPNRM code for neutron multiplicity $i = 1, 2, 3, \dots$

$$\begin{aligned} \sigma^{\text{eval}}(\gamma, in) &= F_i^{\text{th}} \sigma^{\text{exp}}(\gamma, xn) \\ &= \frac{\sigma^{\text{th}}(\gamma, in)}{\sigma^{\text{th}}(\gamma, xn)} \sigma^{\text{exp}}(\gamma, xn). \end{aligned} \quad (38)$$

The former term in Eq. (38) satisfies the reliability criteria as already mentioned, while the second term is not affected by the issues associated with the experimental neutron multiplicity sorting. The resulting derived cross section data $\sigma^{\text{eval}}(\gamma, in)$ should therefore be free from the systematic experimental uncertainties of the Livermore and Saclay data.

In many cases, the evaluated cross-section data $\sigma^{\text{eval}}(\gamma, in)$ obtained from Eq. (38) form a substantial correction to the experimental data obtained by the neutron

multiplicity sorting method [12, 108–115]. A typical example of this evaluation method is given in Fig. 10, where the results obtained for ^{59}Co are compared with the experimental data.

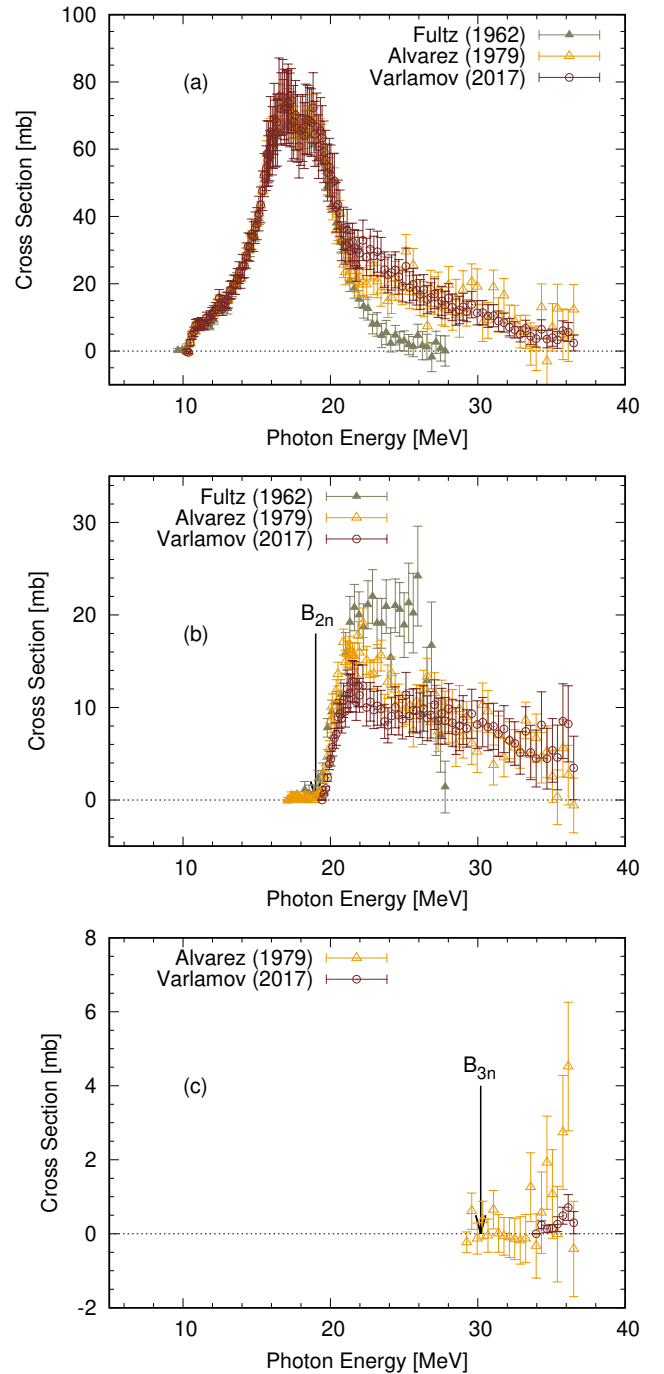


FIG. 10. (Color online) Comparison of the evaluated (open circles with error bars) [117] and experimental (filled triangles [118] and open triangles [119]) partial photo-neutron cross sections for ^{59}Co . (a) $\sigma(\gamma, 1n)$, (b) $\sigma(\gamma, 2n)$, and (c) $\sigma(\gamma, 3n)$.

The neutron multiplicity sorting technique sometimes

cannot distinguish $1n$ and $2n$ events clearly, or $2n$ and $3n$ events. As a result, the partial cross sections $\sigma^{\text{eval}}(\gamma, in)$ fluctuate although the total photo-neutron yield cross section $\sigma^{\text{exp}}(\gamma, xn)$ seems to be reasonable. This can be seen clearly by calculating the differences between the experimental and evaluated integrated cross sections $\sigma^{\text{int,exp}}$ and $\sigma^{\text{int,eval}}$ for the $(\gamma, 1n)$ reaction,

$$\Delta\sigma_1 = \sigma^{\text{int,eval}}(\gamma, 1n) - \sigma^{\text{int,exp}}(\gamma, 1n), \quad (39)$$

and for the $(\gamma, 2n)$ reaction,

$$\Delta\sigma_2 = \sigma^{\text{int,eval}}(\gamma, 2n) - \sigma^{\text{int,exp}}(\gamma, 2n). \quad (40)$$

An example of the differences is shown for ^{92}Zr [33, 120] in Fig. 11. From the figure, it is evident that some of the $(\gamma, 1n)$ events are recorded as $(\gamma, 2n)$ events. It has been shown [38, 110, 121] that this problem is due to the fact that neutrons were sorted into each reaction channel according to the measured neutron kinetic energy. However, the neutron energy spectra for different partial reactions may overlap with each other leading to cross-talks between different partial cross sections, whereby some of the neutrons originating from the $(\gamma, 1n)$ reaction are mistakenly assigned to those from the reaction $(\gamma, 2n)$ and vice versa.

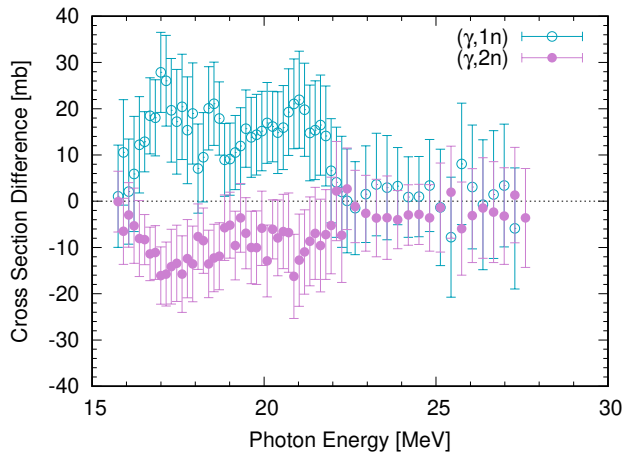


FIG. 11. (Color online) Differences between the evaluated [120] and the experimental [21] cross sections for ^{92}Zr . The open circles are for the $(\gamma, 1n)$ reaction (Δ_1 in Eq. (39)), and filled circles are $(\gamma, 2n)$ reaction (Δ_2 in Eq. (40)).

To test the evaluation method described above, partial photo-neutron reaction cross sections evaluated for ^{181}Ta [108] and ^{209}Bi [115] were compared with those obtained in activation measurements of reaction yields with bremsstrahlung [38, 121]. In the activation measurement, cross sections of various partial reactions were directly determined by identifying the radioactivity from the residual nuclei. Ishkhanov *et al.* [121] and Belyshev *et al.* [38] obtained (γ, in) cross sections with $i = 1 - 6$ for ^{181}Ta and ^{209}Bi as a function of the bombarding photon energy based on the experimental photo-neutron

yields and the CPNRM calculations. The evaluated data for the photo-neutron multiplicity sorting obtained agree well with the activation data. A further confirmation was the agreement found by making a detailed comparison [122] of the evaluated ^{197}Au $(\gamma, 1n)$ and $(\gamma, 2n)$ data with those obtained in activation measurements with bremsstrahlung [39].

It is therefore, advisable to compare the F_i^{exp} with the from F_i^{th} and check whether the following listed conditions are satisfied. In case they are not satisfied, one should investigate possible issues in the measurement that could be responsible for unreliable partial photo-neutron cross sections.

- F_i^{exp} do not exceed the definitive upper limits;
- $\sigma^{\text{exp}}(\gamma, in)$ and corresponding F_i^{exp} are positive; and
- the differences between F_i^{exp} and F_i^{th} are not significant.

Considering the above criteria, the partial and total photo-neutron reaction cross sections were evaluated using the method described above for the following nuclei; ^{59}Co , $^{63,65}\text{Cu}$, ^{75}As , $^{76,78,80,82}\text{Se}$, ^{89}Y , $^{90,91,92,94}\text{Zr}$, ^{98}Mo , ^{103}Rh , ^{115}In , $^{116,117,118,119,120,122,124}\text{Sn}$, ^{133}Cs , ^{138}Ba , ^{139}La , $^{140,142}\text{Ce}$, ^{141}Pr , $^{145,148}\text{Nd}$, ^{153}Eu , ^{159}Tb , ^{160}Gd , ^{165}Ho , ^{181}Ta , ^{186}W , $^{188,189,190,192}\text{Os}$, ^{197}Au , ^{208}Pb , and ^{209}Bi . The derived cross-section data were compiled into the international EXFOR database as “evaluated” data and are available to the nuclear data community.

B. Data Evaluation at KAERI

The photonuclear cross sections have been evaluated for 40 nuclides at KAERI. The experimental data were mainly obtained from the EXFOR database [9] and used for the evaluation work. The F_i -corrected data and the new measurements produced under this CRP, if any, were used preferentially over other data.

As for the nuclear reaction model code, the TALYS code [74] was adopted as it was considered more appropriate for the automatic model parameter tuning system employed to facilitate the present evaluation work. The optical model potential parameters, the GDR parameters, the level density-related parameters, and pre-equilibrium model parameters were adjusted — most of them were within 20% from their default values, and sometimes it goes up to 50% — to reproduce the experimental data or the F_i -corrected data. For the level densities and the γ -ray strength function, the constant temperature and Fermi gas models and the Brink-Axel Lorentzian, respectively, were used in the present evaluations. For the pre-equilibrium reaction, the exciton model was used. The list of adjusted model parameters is summarized below.

- **Optical model:** local parameters for neutron-induced reactions based on the global optical model

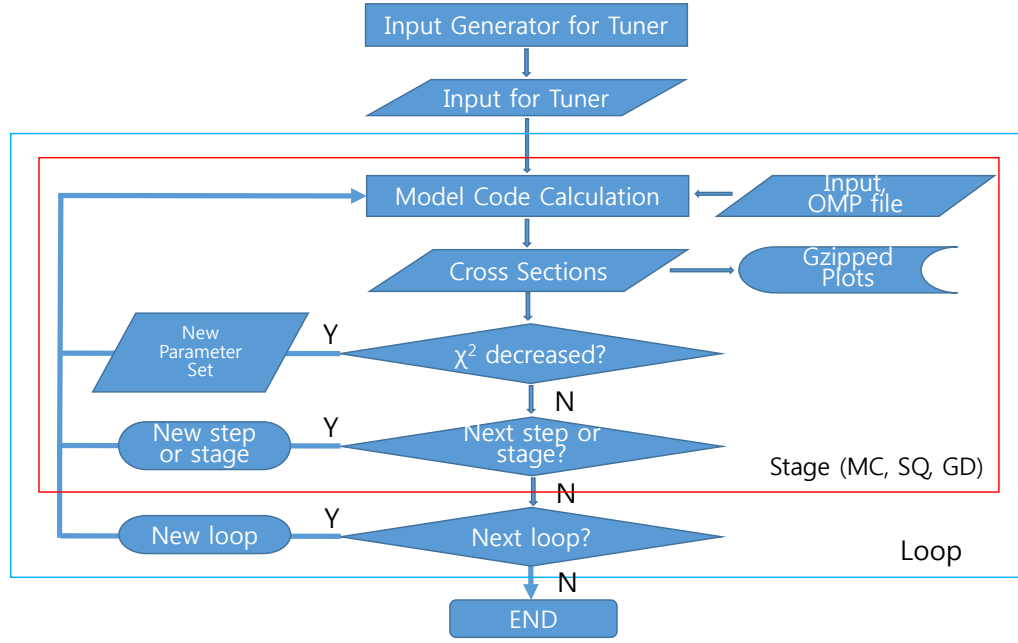


FIG. 12. (Color online) Schematic flow of the automated model parameter tuning at KAERI.

parameters in the Koning-Delaroche form [84]. 19 model parameters are included.

- **Level density related parameters:** the level density parameter, the asymptotic level density, the damping parameter for the shell effects, the pairing correction, the temperature in the Gilbert-Cameron formula for the target and some residual nuclei. About 35 parameters in total for each evaluation are included.
- **GDR parameters:** the peak cross section, energy and width of GDR are adjusted. The γ -ray transmission coefficient calculated from GDR can be re-normalized by a scaling factor.
- **Pre-equilibrium model parameters:** in TALYS the strength of the exciton model is determined by the average squared matrix element M^2 . This is parameterized as

$$M^2 = \frac{C_1}{A^3} \left\{ 7.48C_2 + \frac{4.62 \times 10^5}{\left[\frac{E_{\text{tot}}}{n} + 10.7C_3 \right]^3} \right\}, \quad (41)$$

where n is the number of excitons, C_1 , C_2 , and C_3 are the adjustable parameters included. Since the two-component exciton model in TALYS distinguishes an exciton to be a neutron or a proton, the interaction strength between neutron (ν) and proton (π) can be adjusted by introducing the scaling factors $M_{\pi\pi}^2 = R_{\pi\pi}M^2$, $M_{\nu\nu}^2 = R_{\nu\nu}M^2$, $M_{\pi\nu}^2 = R_{\pi\nu}M^2$, and $M_{\nu\pi}^2 = R_{\nu\pi}M^2$. These R factors are also adjusted.

The model parameter tuning processes were automatically carried out using the specially developed tuning system, as shown in Fig. 12. The parameter tuning system consists of a preprocessor and a tuning tool. The preprocessor automatically generates the necessary input files for the tuning tool by reading the output file of a default TALYS run and EXFOR files. The tuning tool then repeatedly adjusts the model parameters, creates an input file for TALYS, runs TALYS, compares the calculated results with the experimental data, and computes χ^2 . It searches for the optimum model parameters with minimum χ^2 using gradient search, grid search and/or random search. To reduce the computation time, multiple CPUs are employed simultaneously using MPI. The whole process ends after a user-specified number of loops and a user may monitor the current status by looking at the plots which are automatically generated after each calculation. In the following we compare the KAERI evaluations with available experimental data for selected cases.

1. ^{94}Zr

The photonuclear data for ^{94}Zr in the previous IAEA 1999 library were evaluated by KAERI using the GUNF and GNASH code. The previous evaluation was done based on the $(\gamma, 1nX)$, $(\gamma, 2nX)$, σ_{Sn} and σ_{xn} reaction cross sections of Berman *et al.* [33]. The present evaluation was performed to reproduce the new $(\gamma, 1nX)$, $(\gamma, 2nX)$, $(\gamma, 3nX)$ and σ_{Sn} cross sections of Varlamov *et al.* [112] which are F_i -corrected ones. The $(\gamma, 1nX)$ cross

sections of Varlamov are higher than those of Berman by 10% and the new $(\gamma, 2nX)$ cross sections of Varlamov are lower than those of Berman by 15% in the peak region. The calculated photonuclear cross sections for ^{94}Zr are compared with the experimental and evaluated data [33, 112] in Fig. 13. As described above, the model parameters were adjusted to reproduce the evaluated experimental data of Varlamov *et al.*

2. ^{133}Cs

The photonuclear data for ^{133}Cs in the previous IAEA 1999 library were evaluated by KAERI using the GUNF and GNASH code. The previous evaluation was done based on the $(\gamma, 1nX)$, $(\gamma, 2nX)$, σ_{Sn} and σ_{xn} reaction cross sections of Leprêtre *et al.* [123]. The present evaluation was performed to reproduce the new $(\gamma, 1nX)$, $(\gamma, 2nX)$, $(\gamma, 3nX)$ and σ_{Sn} cross sections of Varlamov *et al.* [115] which are F_i -corrected ones. The $(\gamma, 1nX)$ cross sections of Varlamov are similar to those of Leprêtre and the $(\gamma, 2nX)$ cross sections of Varlamov are much higher than those of Leprêtre by 30% in the peak region. The calculated photonuclear cross sections for ^{133}Cs are compared with the evaluated and experimental data [115, 123, 124] in Fig. 14.

3. ^{138}Ba

The photonuclear data for ^{138}Ba were not included in the previous IAEA 1999 library. The present evaluation was performed to reproduce the new $(\gamma, 1nX)$, $(\gamma, 2nX)$, $(\gamma, 3nX)$ and σ_{Sn} cross sections of Varlamov *et al.* [115] which are F_i -corrected ones. The calculated photonuclear cross sections for ^{138}Ba are compared with the experimental and evaluated data [115, 125] in Fig. 15.

4. ^{142}Ce

The photonuclear data for ^{142}Ce were not included in the previous IAEA 1999 library. The present evaluation was performed to reproduce the new $(\gamma, 1nX)$, $(\gamma, 2nX)$ and σ_{xn} cross sections of Leprêtre *et al.* [126]. The calculated photonuclear cross sections for ^{142}Ce are compared with the experimental data [126] in Fig. 16.

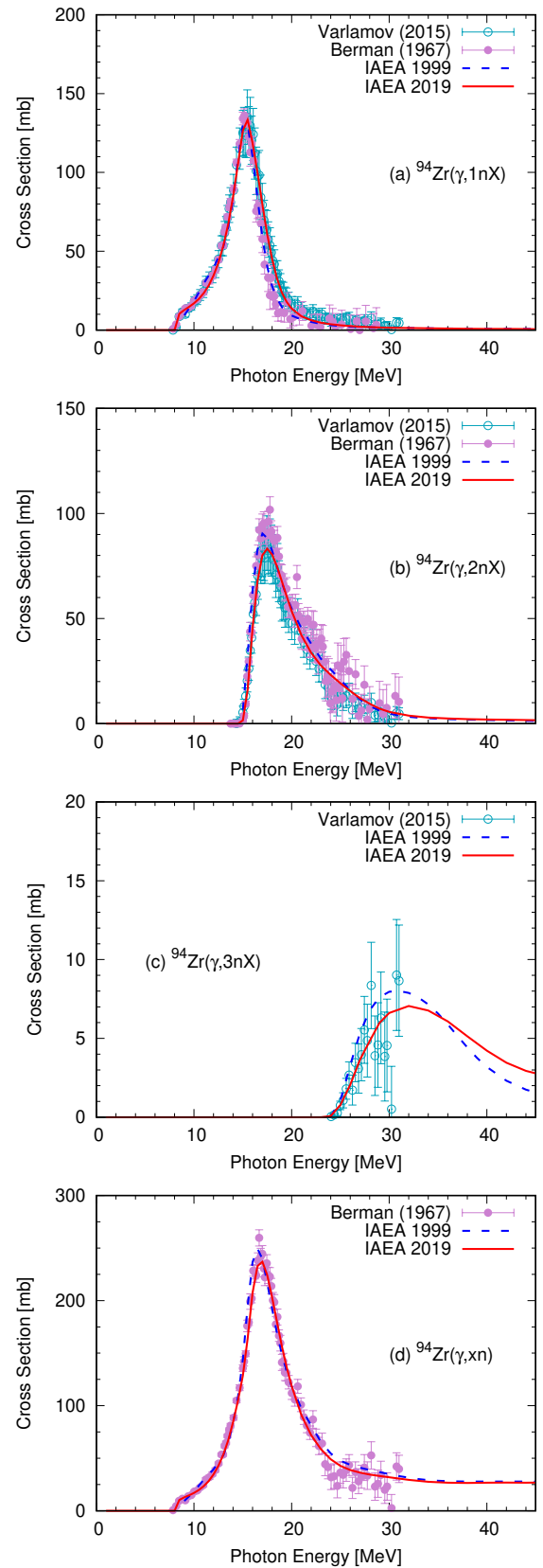


FIG. 13. (Color online) Comparison of evaluated and experimental cross sections for the γ -ray induced reaction on ^{94}Zr . (a) $\sigma(\gamma, 1nX)$, (b) $\sigma(\gamma, 2nX)$, (c) $\sigma(\gamma, 3nX)$, and (d) σ_{xn} .

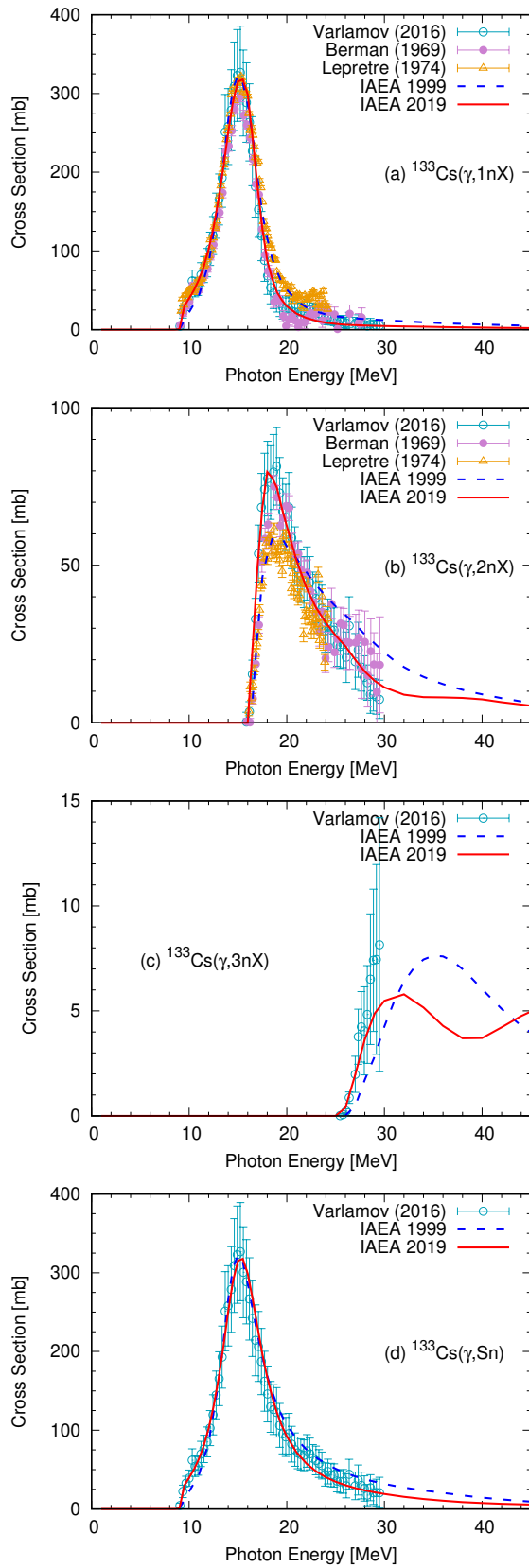


FIG. 14. (Color online) Comparison of evaluated and experimental cross sections for the γ -ray induced reaction on ^{133}Cs . (a) $\sigma(\gamma, 1nX)$, (b) $\sigma(\gamma, 2nX)$, (c) $\sigma(\gamma, 3nX)$, and (d) σ_{Sn} .

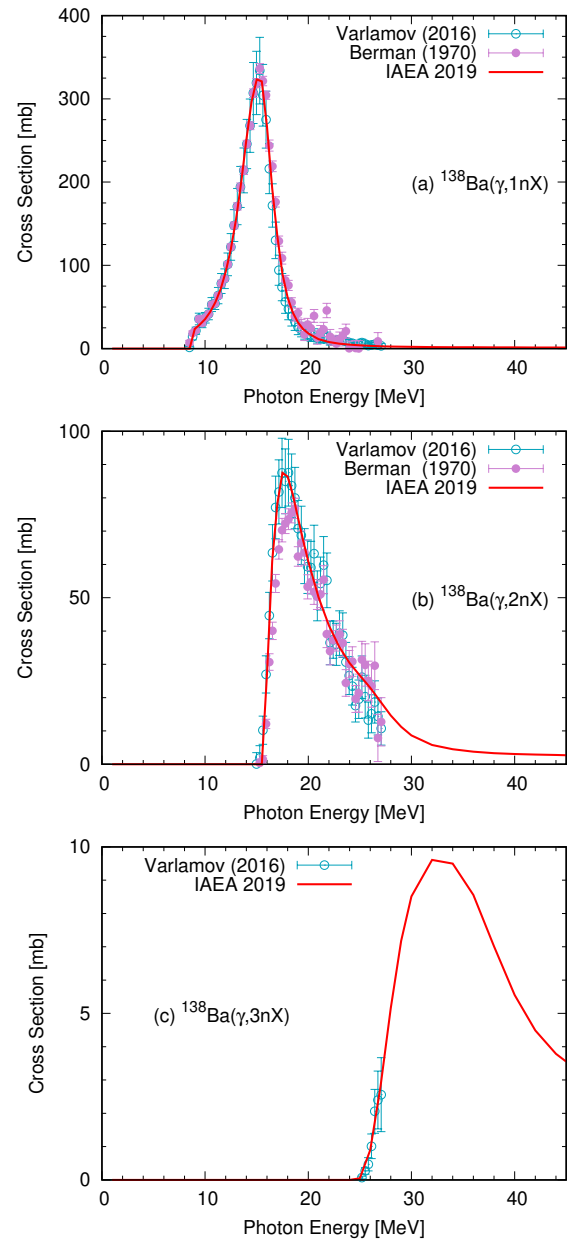


FIG. 15. (Color online) Comparison of evaluated and experimental cross sections for the γ -ray induced reaction on ^{138}Ba . (a) $\sigma(\gamma, 1nX)$, (b) $\sigma(\gamma, 2nX)$, and (c) $\sigma(\gamma, 3nX)$.

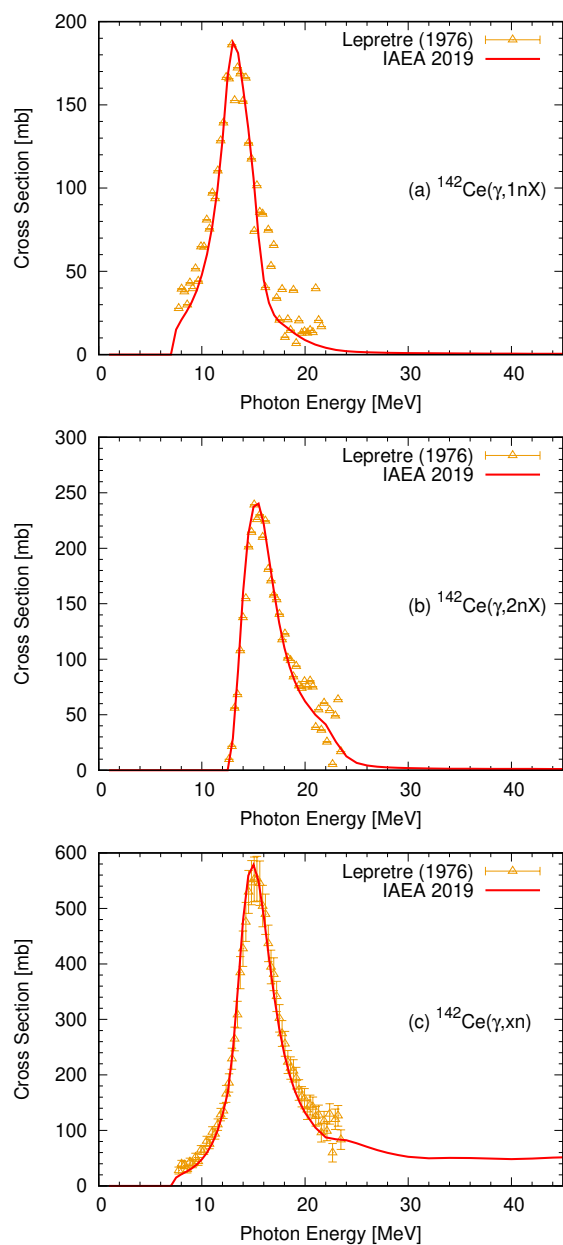


FIG. 16. (Color online) Comparison of evaluated and experimental cross sections for the γ -ray induced reaction on ^{142}Ce . (a) $\sigma(\gamma, 1nX)$, (b) $\sigma(\gamma, 2nX)$, and (c) σ_{xn} .

C. Data Evaluation at IFIN-HH

Photo-neutron reaction cross sections for ^{59}Co , ^{89}Y , ^{103}Rh , ^{159}Tb , ^{165}Ho , ^{169}Tm and ^{181}Ta have been recently measured in the GDR region using quasi-monochromatic LCS γ -ray beams at the NewSUBARU facility. The partial photo-neutron cross sections, σ_{inX} with $i = 1$ to 4, were determined with the direct neutron multiplicity sorting method described in Sec. IIIB4, which is based on a slow response flat efficiency neutron detector. The average neutron emission energy corresponding to the total neutron-yield cross section was also provided using the ring ratio method, as described in Sec. IIIB2. The total σ_{Sn} and partial σ_{inX} ($i = 1 - 4$) cross sections have been communicated among the CRP members for evaluations, leaving possible small modifications to be made on the final results which will be published separately. We evaluated the newly measured NewSUBARU data for the seven nuclei listed above in an attempt to resolve the long-standing discrepancies between the Livermore and Saclay measurements detailed in Sec. VA.

The EMPIRE statistical model code [73] has been employed for the evaluations. For each evaluated nucleus, we have investigated which of the MLO1, MLO2, SLO and SMLO closed-forms for E1 γ -ray strength functions [58] implemented in EMPIRE reproduces best the experimental data. We also implemented in EMPIRE a third SLO component, which was used if necessary. EMPIRE also includes the quasi-deuteron contribution to describe the photo-absorption cross section above the GDR region, up to 200 MeV.

When evaluating the NewSUBARU experimental data, we took into account that, as also in the case of Saclay and Livermore data, the detection system was not sensitive to the charged particle emission from the target. The NewSUBARU experiments provided the sum of cross sections with i neutrons in the final state (γ, inX), where $i = 1$ to 4. The total photo-neutron cross section σ_{Sn} was obtained as the sum $\sum_i \sigma_{inX}$. For each nucleus, we adjusted the photo-absorption to reproduce the total photo-neutron cross section σ_{Sn} . Finally we tuned the level density parameters, and the single particle level density parameters from the PCROSS pre-equilibrium model in order to reproduce the experimental σ_{inX} data with $i = 1 - 4$. The global Koning-Delaroche potentials [84] have been used to obtain the transmission coefficients for proton and neutron emission.

In order to compute complex σ_{inX} cross sections, one has to determine cross sections for different reaction chains which populate the same residual nucleus. For example, let us consider the $^A_Z X$ photo-disintegration to $^{A-3}_{Z-1} X$ nucleus, which can be produced by six different reaction chains (γ, nnp), (γ, npn), (γ, pnn), (γ, nd), (γ, dn) and (γ, t). We compute the sum cross sections (γ, nnp) + (γ, npn) + (γ, pnn) and (γ, nd) + (γ, dn) separately, which contribute to the ($\gamma, 2nX$) and ($\gamma, 1nX$) reactions, respectively.

Because of limitations imposed by the available com-

puting power and huge memory requirement, the EMPIRE statistical model code uses only one memory buffer per compound nucleus (CN) which is incremented by all reactions chains that populate the same CN. Thus, the code provides the population cross sections of each accessible CN disregarding the way it was produced and the emission cross section of each particle that can be emitted from the given CN. To obtain the cross sections for different reaction chains which populate the same residual nucleus, we developed a method of reconstructing all possible pathways by processing the statistical model code results. This treatment is particularly important for low mass nuclei which have a large contribution of charged particle emission.

The method uses the additional information provided by EMPIRE concerning exclusive cross sections, which are defined as the double differential cross section / occupation for obtaining a nucleus in a certain state after having emitted a certain particle (proton, neutron, α -particle, ...). This cross section takes into account all emissions of that particular particle that lead to the given final state. However, the method does not provide exact results, because the information concerning spin and parity population distribution of the CN is taken into account only as an average. EMPIRE could easily avoid this approximation, but the calculation would grow by many orders of magnitude, an increase which would not be justified by an advantage of more precise splitting of inclusive spectra into their exclusive components. Also, obtaining cross sections for all pathways is possible up to a certain energy over which, due to the complexity of all the possible pathways, the information concerning exclusive population cross section alone is not anymore sufficient to solve very complex equation systems. The NewSUBARU measurements were performed up to energies located under this energy limit to takes all possible pathways into account properly.

1. ^{59}Co

The previous ^{59}Co evaluation has been performed by KAERI using the GNASH code [85, 86]. The KAERI evaluation modeled the ($\gamma, 1nX$) and ($\gamma, 2nX$) reaction cross sections of Alvarez *et al.* [119] and Fultz *et al.* [118], the ($\gamma, 3nX$) reaction cross sections of Alvarez and the σ_{xn} data of Alvarez and Bazhanov *et al.* [127]. New σ_{Sn} , σ_{1nX} , σ_{2nX} and σ_{3nX} have been measured at NewSUBARU for ^{59}Co in the energy region between 10 and 40 MeV. The NewSUBARU data are shown by the filled circles in Figs. 17 and 18. The NewSUBARU (γ, Sn) cross section is about 20% higher than the Livermore data of Fultz and Alvarez and the peaks of the two GDR Lorentzians are not well separated. The MLO1 γ -ray strength function with two centroids reproduced best the (γ, Sn) cross sections. A third SLO has been introduced to reproduce the large width of the GDR region.

For this particular nucleus newly measured at New-

SUBARU, the charged-particle emission contribution is stronger, as can be seen in Figs 17 and 18. The EMPIRE photo-absorption and the photo-neutron cross sections are displayed in Fig. 17 by the dot-dashed and continuous lines, respectively, where the difference between the two cross sections is attributed to the charged-particle emission channel which is unaccompanied by neutron emission. The sum cross section of all neutron emission only channels is shown with the dotted line. We can observe that, because of the strong charged particle contribution, the GDR parameters, namely the peak cross section and width, cannot be obtained by directly fitting the measured photo-neutron cross section with a set of Lorentzians. Figure 18 shows the comparison between (γ, inX) (solid lines) and (γ, in) (dotted lines) cross sections for $i = 1 - 3$, where the emission of accompanying charged particles increases with increasing energy.

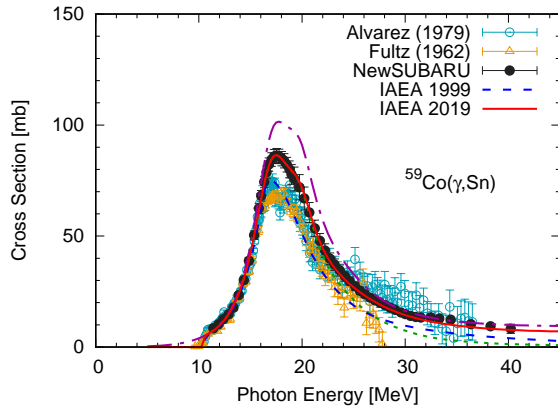


FIG. 17. (Color online) Comparison between experimental and evaluated (solid line) total cross sections σ_{Sn} for ^{59}Co . Evaluated photo-absorption cross section including charged-particle channels is also shown by the dot-dashed line. The evaluated sum cross section $\sum_i \sigma_{in}$ ($i = 1 - 3$) of all channels without charged-particle emission is also shown by the dotted line.

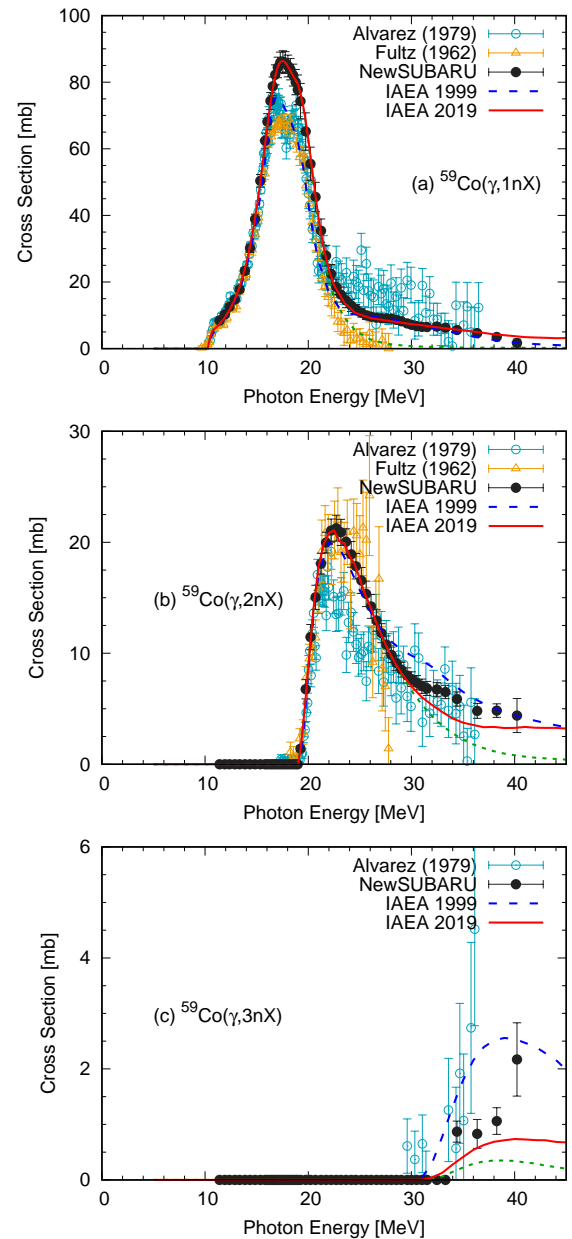


FIG. 18. (Color online) Comparison between experimental and evaluated (solid lines) partial cross sections for ^{59}Co : (a) σ_{1nX} , (b) σ_{2nX} , and (c) σ_{3nX} . See Fig. 17 for the dotted line.

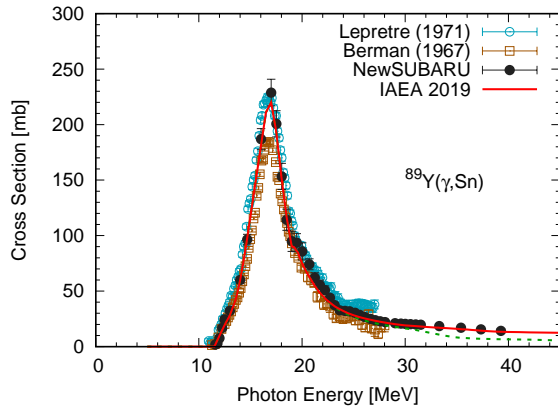


FIG. 19. (Color online) Comparison between evaluated (solid line) and experimental total cross sections σ_{Sn} for ^{89}Y . The evaluated sum cross section $\sum_i \sigma_{in}$ ($i = 1 - 3$) of all channels without charged-particle emission is also shown by the dotted line.

2. ^{89}Y

^{89}Y was not included in the previous IAEA 1999 database. The $(\gamma, 1nX)$, $(\gamma, 2nX)$, (γ, Sn) reaction cross sections and the neutron yield σ_{xn} have been measured by Berman *et al.* [33] and by Leprêtre *et al.* [128] between 11 and 28 MeV excitation energy. New (γ, Sn) , $(\gamma, 1nX)$, $(\gamma, 2nX)$ and $(\gamma, 3nX)$ cross sections have been measured at NewSUBARU for ^{89}Y in the energy region between 11 and 40 MeV. The NewSUBARU and the Saclay cross sections are in good agreement in the GDR peak energy region. The (γ, Sn) reaction cross section was best reproduced by using the SMLO model for the γ -ray strength function with two centroids. The evaluation is compared to the experimental data in Figs. 19 and 20.

3. ^{103}Rh

^{103}Rh was not included in the previous IAEA 1999 database. The $(\gamma, 1nX)$, $(\gamma, 2nX)$, (γ, Sn) reaction cross sections and the neutron yield σ_{xn} have been measured by Leprêtre *et al.* [123] between 9 and 26 MeV excitation energy. The (γ, Sn) cross section has been measured using bremsstrahlung beams by Parsons [129] and by Bogdankevich *et al.* [130], where Bogdankevich reported also the $(\gamma, 2nX)$ cross section. New (γ, Sn) , $(\gamma, 1nX)$, $(\gamma, 2nX)$ and $(\gamma, 3nX)$ cross sections have been measured at NewSUBARU for ^{103}Rh in the energy region between 9 and 42 MeV. The NewSUBARU and the Saclay cross sections are in overall good agreement in the entire investigated energy region. The MLO2 with two centroids reproduced best the (γ, Sn) cross sections. A third SLO has been introduced to reproduce the large width of the GDR peak region. The evaluation is compared to the experimental data in Figs. 21 and 22. The comparison be-

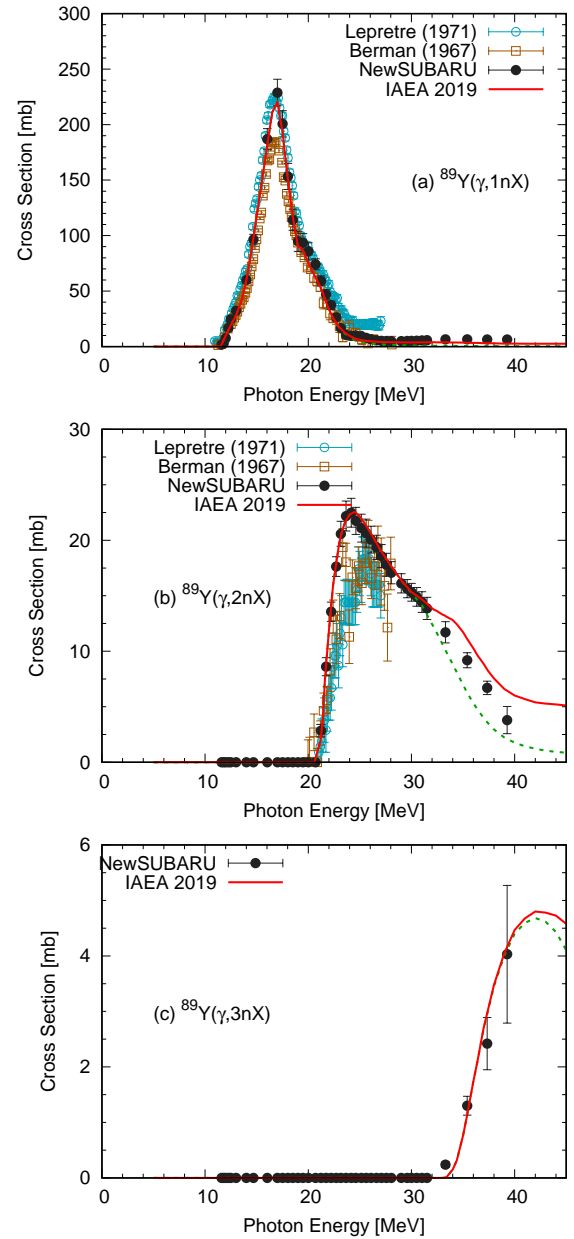


FIG. 20. (Color online) Comparison between experimental and evaluated (solid lines) partial cross sections for ^{89}Y : (a) σ_{1nX} , (b) σ_{2nX} , and (c) σ_{3nX} . See Fig. 19 for the dotted lines.

tween the experimental and calculated average neutron emission energy corresponding to the neutron-yield cross section is displayed in Fig. 22. We underline that the model parameter was tuned for the experimental cross sections not for the average neutron energies.

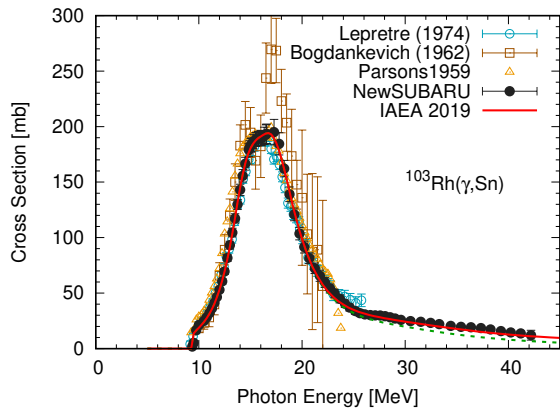


FIG. 21. (Color online) Comparison between experimental and evaluated (solid line) total cross sections σ_{Sn} for ^{103}Rh . The evaluated sum cross section $\sum_i \sigma_{in}$ ($i=1-3$) of all channels without charged-particle emission is also shown by the dotted line.

4. ^{159}Tb

The previous ^{159}Tb evaluation has been performed by KAERI using the GNASH code. The $(\gamma, 1nX)$, $(\gamma, 2nX)$ and (γ, xn) cross sections have been measured both by Bramblett *et al.* [131] and by Bergère *et al.* [132]. Bergère also reported the $(\gamma, 3nX)$ and (γ, Sn) cross sections. The σ_{Sn} have been measured using bremsstrahlung beams by Bogdankevich *et al.* [130] and by Goryachev *et al.* [133]. The KAERI evaluation follows the Bergère (γ, Sn) , $(\gamma, 1 \sim 3nX)$ cross sections. New (γ, Sn) , $(\gamma, 1nX)$, $(\gamma, 2nX)$, $(\gamma, 3nX)$ and $(\gamma, 4nX)$ cross sections have been measured at NewSUBARU for ^{159}Tb in the energy region between 8 and 42 MeV. The NewSUBARU $(\gamma, 1nX)$ and $(\gamma, 3nX)$ cross sections are in agreement with the Saclay data, while the new $(\gamma, 2nX)$ cross sections are in agreement with the Livermore data. For the evaluation, the NewSUBARU (γ, Sn) reaction cross section was best reproduced by using the SMLO model for the γ -ray strength function with two centroids. The evaluation is compared to the experimental data in Figs. 24 and 25.

5. ^{165}Ho

The previous ^{165}Ho evaluation has been performed by KAERI using the GNASH code. The (γ, Sn) , $(\gamma, 1nX)$, $(\gamma, 2nX)$, $(\gamma, 3nX)$ cross sections have been measured both by Berman *et al.* [134] and by Bergère *et al.* [132]. The total nuclear photo-absorption cross section σ_{abs} has been measured by Gurevich *et al.* [135]. The σ_{Sn} and σ_{2nx} have also been reported by Goryachev *et al.* [133]. The KAERI evaluation followed the Bergère cross sections. New (γ, Sn) , $(\gamma, 1nX)$, $(\gamma, 2nX)$, $(\gamma, 3nX)$ and $(\gamma, 4nX)$ cross sections have been measured at New-

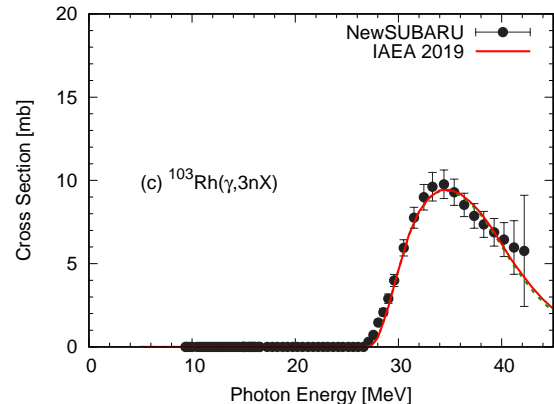
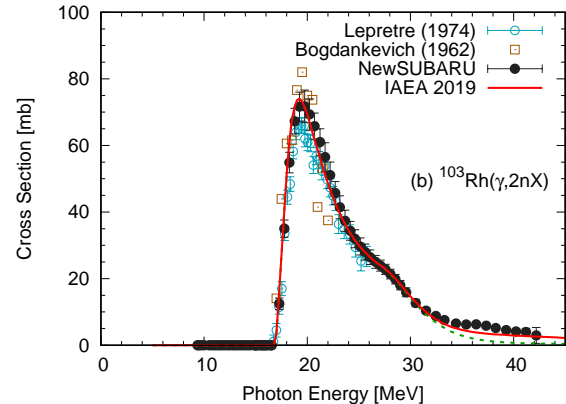
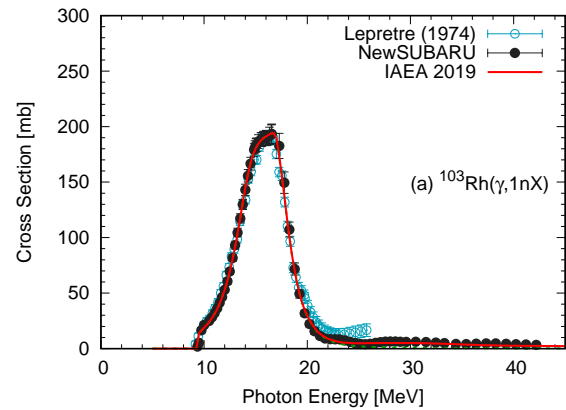


FIG. 22. (Color online) Comparison between experimental and evaluated (solid lines) partial cross sections for ^{103}Rh : (a) σ_{1nX} , (b) σ_{2nX} , and (c) σ_{3nX} . See Fig. 21 for the dotted lines.

SUBARU for ^{165}Ho in the energy region between 8 and 43 MeV. The NewSUBARU $(\gamma, 1nX)$ cross sections are in better agreement with the Saclay measurement while the new $(\gamma, 2nX)$ cross sections are higher than both the Saclay and Livermore data by $\sim 20\%$ in the peak region. For the evaluation, the NewSUBARU (γ, Sn) reaction cross section was best reproduced by using the SMLO model for the γ -ray strength function with two centroids. The evaluation is compared to the experimental data in Figs. 26 and 27.

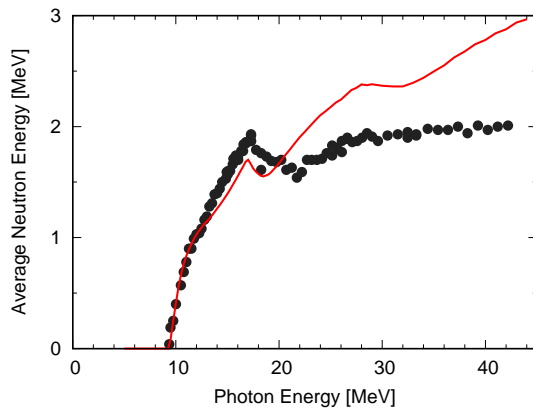


FIG. 23. (Color online) Comparison between evaluated and experimental values for average energy of neutrons emitted in photo-induced reactions on ^{103}Rh .

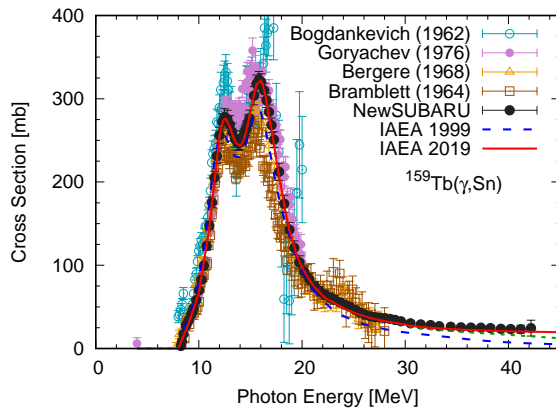


FIG. 24. (Color online) Comparison between experimental and evaluated total cross sections σ_{Sn} for ^{159}Tb . The solid line is the current evaluation, and the dashed line is IAEA 1999 library [3]. The evaluated sum cross section $\sum_i \sigma_{in}$ ($i = 1 - 4$) of all channels without charged-particle emission is also shown by the dotted line.

6. ^{169}Tm

The (γ, Sn) , $(\gamma, 1nX)$, $(\gamma, 2nX)$, $(\gamma, 3nX)$ and $(\gamma, 4nX)$ cross sections have been measured at NewSUBARU for ^{169}Tm in the energy region between 8 and 40 MeV. No other data exist. For the evaluation, the NewSUBARU (γ, Sn) reaction cross section was best reproduced by using the SMLO model for the gamma ray strength function with two centroids. The evaluation is compared to the experimental data in Figs. 28 and 29.

7. ^{181}Ta

The previous ^{181}Ta evaluation has been taken from the JENDL Photonuclear Data Library [136] constructed

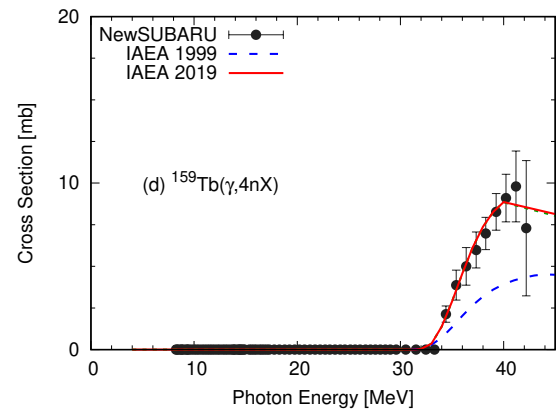
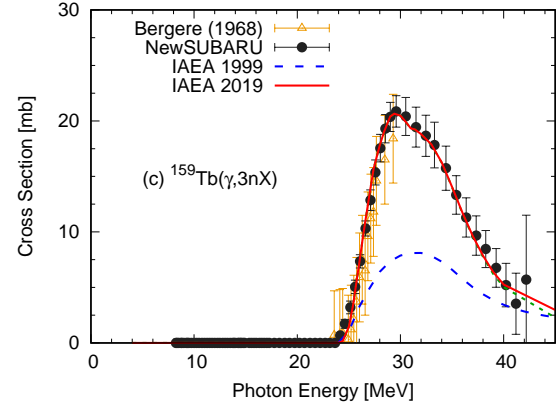
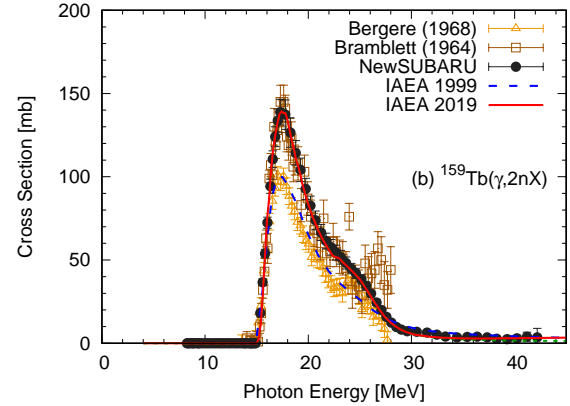
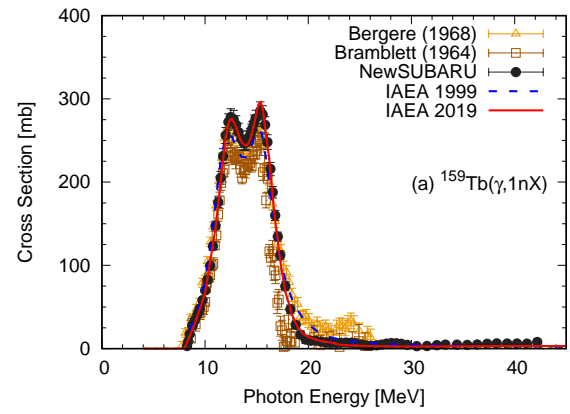


FIG. 25. (Color online) Comparison between experimental and evaluated (solid and dashed lines) partial cross sections for ^{159}Tb : (a) σ_{1nX} , (b) σ_{2nX} , (c) σ_{3nX} , and (d) σ_{4nX} . See Fig. 24 for the dotted lines.

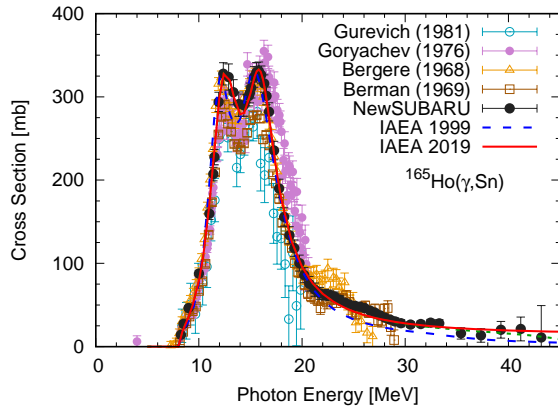


FIG. 26. (Color online) Comparison between experimental and evaluated (solid line) σ_{Sn} for ^{165}Ho . The evaluated sum cross section $\sum_i \sigma_{in}$ ($i = 1 - 4$) of all channels without charged-particle emission is also shown by the dotted lines.

with the ALICE-F [87] code. The JAERI evaluation was performed on existing (γ, Sn) , $(\gamma, 1nX)$ and $(\gamma, 2nX)$ cross sections measured by Bergère *et al.* [132] and by Bramblett *et al.* [137], where the Livermore cross sections have been reconstructed based on a study performed at the Sao Paulo laboratory [34, 138]. The σ_{Sn} has been measured using bremsstrahlung beams by Belyaev *et al.* [139], Fuller *et al.* [140], Antropov *et al.* [141], Bogdankevich *et al.* [130] and Gurevich *et al.* [142]. Bogdankevich [130] reported also the $(\gamma, 2nX)$. Additional $(\gamma, 1nX)$ measurements have been performed using LCS γ -ray beams by Utsunomiya *et al.* [42] and Goko *et al.* [143]. New (γ, Sn) , $(\gamma, 1nX)$, $(\gamma, 2nX)$, $(\gamma, 3nX)$ and $(\gamma, 4nX)$ cross sections have been measured at NewSUBARU for ^{181}Ta in the energy region between 12 and 41 MeV. The NewSUBARU $(\gamma, 1nX)$ cross sections are in better agreement with the Saclay measurement, but have higher cross sections in the GDR peak region. The NewSUBARU results do not separate well the peaks of the two GDR Lorentzians, resembling better the Livermore data. The new $(\gamma, 2nX)$ cross sections are in better agreement with the Livermore data. For the evaluation, the NewSUBARU (γ, Sn) reaction cross section was best reproduced by using the SMLO model for the γ -ray strength function with two centroids. The evaluation is compared to the experimental data in Figs. 30 and 31.

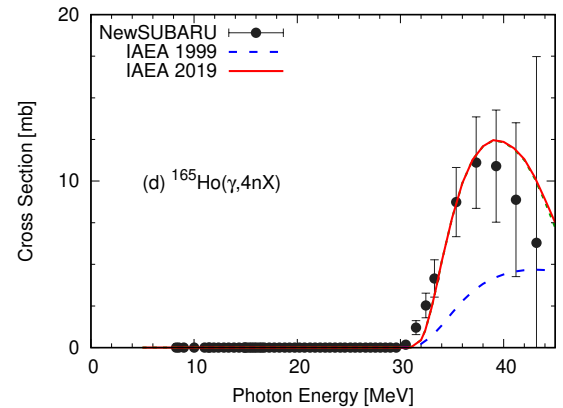
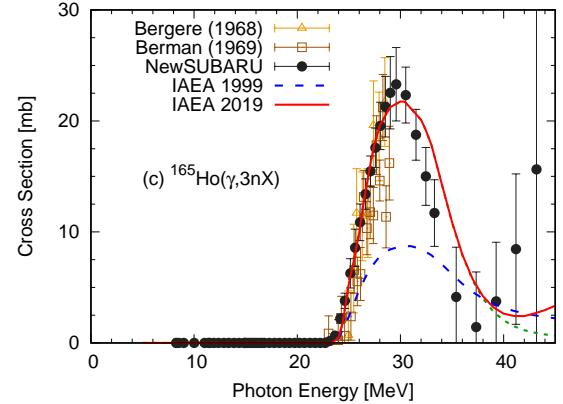
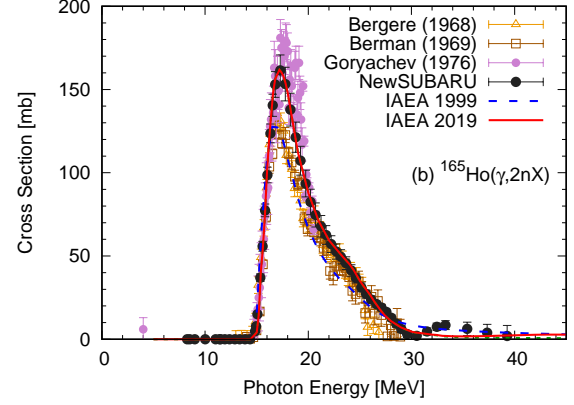
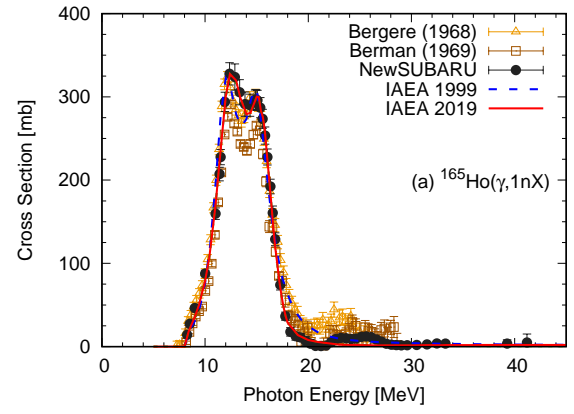


FIG. 27. (Color online) Comparison between experimental and evaluated (solid lines) partial cross sections for ^{165}Ho : (a) σ_{1nX} , (b) σ_{2nX} , (c) σ_{3nX} , and (d) σ_{4nX} . See Fig. 26 for the dotted lines.

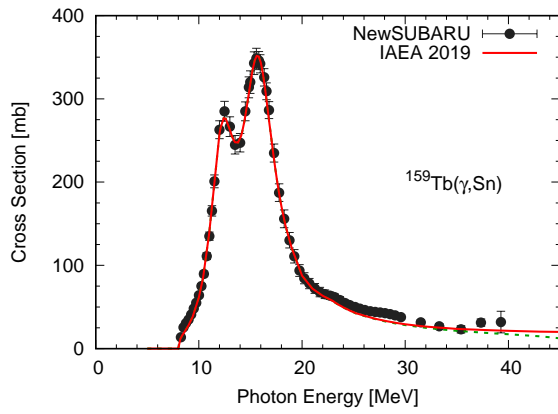


FIG. 28. (Color online) Comparison between evaluated and NewSUBARU σ_{Sn} for ^{169}Tm . The evaluated sum cross section $\sum_i \sigma_{in}$ ($i = 1 - 4$) of all channels without charged-particle emission is also shown by the dotted lines.

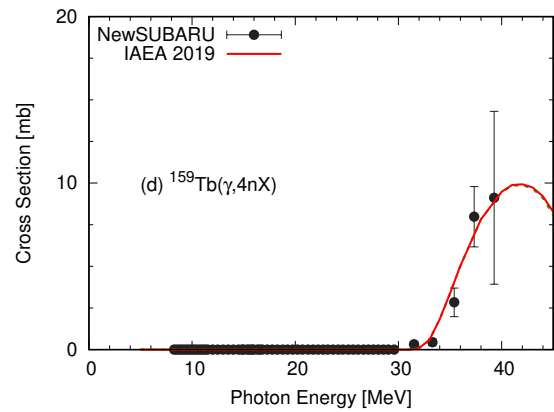
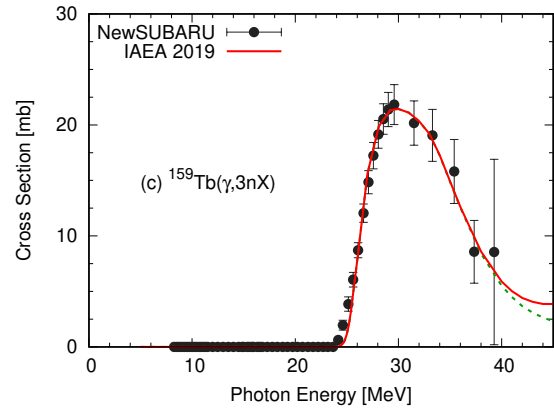
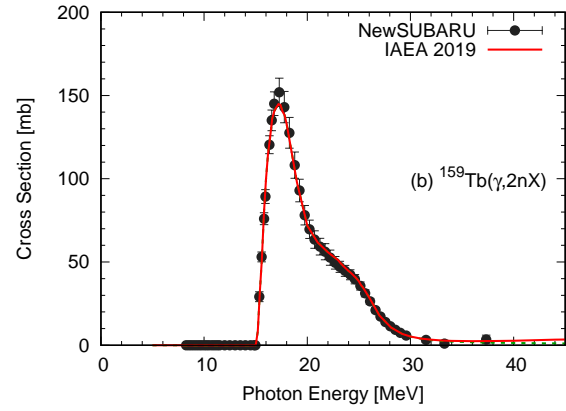
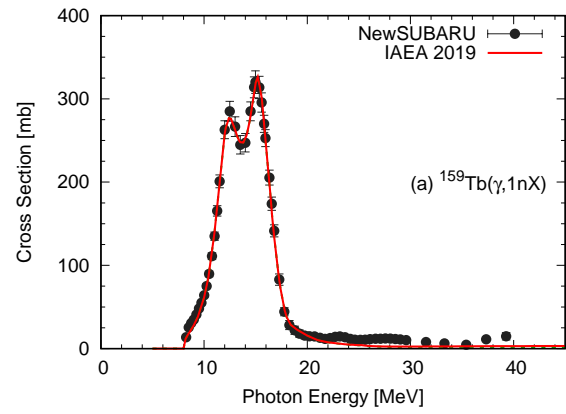


FIG. 29. (Color online) Comparison between evaluated and NewSUBARU partial cross sections for ^{169}Tm : (a) σ_{1nX} , (b) σ_{2nX} , (c) σ_{3nX} , and (d) σ_{4nX} . See Fig. 28 for the dotted lines.

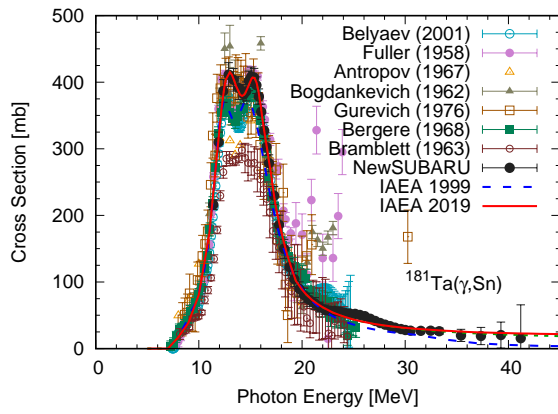


FIG. 30. (Color online) Comparison between experimental and evaluated σ_{Sn} for ^{181}Ta . The solid line is the current evaluation, and the dashed line is IAEA 1999 library [3]. The evaluated sum cross section $\sum_i \sigma_{in}$ ($i = 1 - 4$) of all channels without charged-particle emission is also shown by the dotted line.

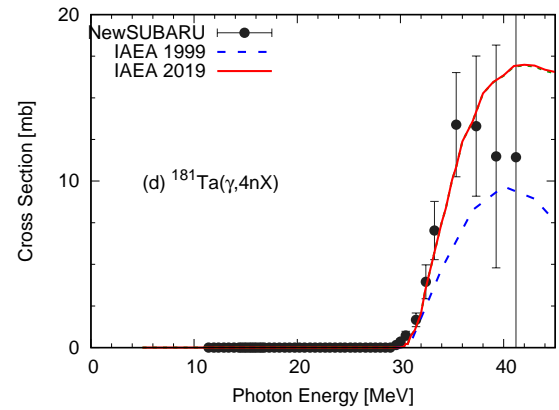
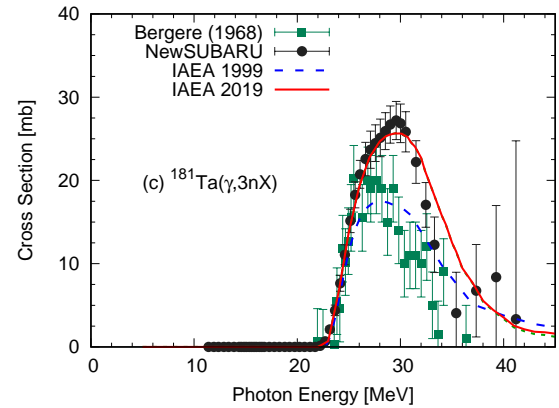
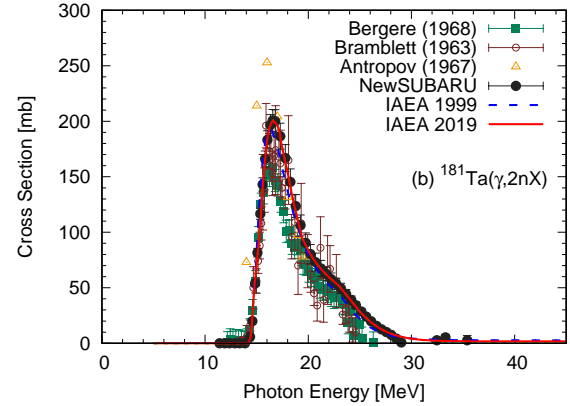
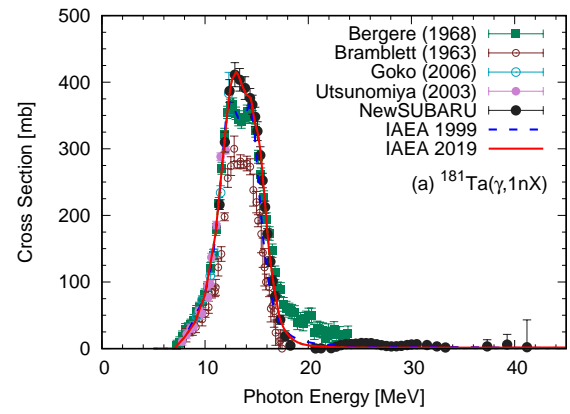


FIG. 31. (Color online) Comparison between evaluated and NewSUBARU partial cross sections for ^{181}Ta : (a) σ_{1nX} , (b) σ_{2nX} , (c) σ_{3nX} , and (d) σ_{4nX} . See Fig. 30 for the dotted line.

D. Data Evaluation at JAEA

For quite a few nuclides, the photonuclear data in the IAEA 2019 library are adopted from the JENDL photonuclear data file 2016 (JENDL/PD-2016), which was released in December, 2017. These nuclides are listed in Appendix A. JENDL/PD-2016 includes photo-induced reaction data (photo-absorption cross section, photo-fission cross section, the average number of prompt and delayed fission neutrons, particle and photon emission cross sections and energy-angle distribution, residual cross sections, *etc.*) up to 140 MeV energy. The evaluation was made by the CCONE code [75] for medium to heavy nuclides.

Some of the light nuclides with atomic number ≤ 20 were also taken from JENDL/PD-2016; ^3He , $^6,^7\text{Li}$, and ^{19}F . Those nuclear data were evaluated by the method described by Murata *et al.* [144] with the ALICE-F code [87], except for $^{35,37}\text{Cl}$, $^{36,38,40}\text{Ar}$ and $^{39,40,41}\text{K}$, which were evaluated with CCONE [75]. In Murata's method, measured photo-absorption and $(\gamma, 1nX)$ reaction cross sections were reproduced by resonances and quasi-deuteron disintegration models. The other cross sections were calculated with ALICE-F, which provided cross section ratios of particle emission cross sections to the photo-absorption one. The energy-angle distributions calculated with ALICE-F were replaced by the results of CCONE calculation. The nuclear data of light nuclides evaluated by this method have an upper energy limit of 140 MeV, which is the same as JENDL/PD-2016.

The CCONE code consists of the Hauser-Feshbach model for statistical decay and the two-component excitation model for pre-equilibrium decay. The deexcitation by γ -rays is expressed by the E1, M1 and E2 transitions. For the E1 radiation, the MLO1 model is basically utilized for the photon strength function. The default GDR parameters are taken from the RIPL-2 systematics [145]. Those parameters are modified so as to reproduce measured photo-absorption and/or photoneutron cross sections. For the M1 and E2 radiations the formulations of Kopecky and Uhl [65] are adopted. The discrete level information is taken from the RIPL-3 database [58]. The Gilbert-Cameron formula [146] is employed as a model describing the level density above the discrete levels, where the Fermi-gas model is replaced by the revised model of Mengoni and Nakajima [147]. In the statistical decay, we consider six particle emission channels, namely neutron, proton, deuteron, triton, ^3He , and α -particle, as well as the γ -ray emission. For the particle emission, the optical model potential parameters of Koning-Delaroche [84] for neutrons and protons, Han *et al.* [106] for deuteron, folding potential generated from the neutron and proton potentials of Koning-Delaroche for triton, Xu *et al.* [107] for ^3He and Avrigneanu-Avrigneanu [100] for α -particles are adopted. The photon incident energy region is extended up to 200 MeV. The lowest energy of 1 MeV is unchanged in the evaluations by CCONE. The quasi-deuteron disintegra-

tion model, which has an important contribution above the photon energy of 40 MeV, is also implemented. The Pauli-blocking function $P_b(E_\gamma)$ in the model is originally derived in the energy range of 20 to 140 MeV. The extension to lower and higher energies is necessary to produce nuclear data from 1 to 200 MeV. The function is extrapolated by Eq. (27).

The inclusive data form (MF/MT=6/5) in the ENDF-6 format is adopted in the JAEA evaluations. The experimental $(\gamma, 1nX)$ reaction cross section, which is the sum of $(\gamma, 1n)$, $(\gamma, 1np)$ and $(\gamma, 1n\alpha)$ reaction ones and so on, for example, cannot be separated into individual reaction. Thus, in the figures shown below, the present results for $(\gamma, 1n)$ and $(\gamma, 2n)$ reactions are used for comparisons with measured $(\gamma, 1nX)$ and $(\gamma, 2nX)$ reaction cross sections. Such a comparison is justified for nuclides with high atomic number, since reaction cross sections accompanying charged particle emissions such as $(\gamma, 1np)$ and $(\gamma, 1n\alpha)$ reactions are highly suppressed due to the large Coulomb barrier. Note that the $(\gamma, 1n)$ and $(\gamma, 2n)$ reaction cross sections are given as the production cross sections of residual nuclides with the mass numbers of $A - 1$ and $A - 2$ for a target with A in the ENDF-6 format.

In the case of nuclides with fission reaction, the average number of prompt neutrons per fission $\bar{\nu}_p$ is calculated with the linear functions with respect to photon energy fitted by Berman *et al.* [148] and Caldwell *et al.* [149], complemented with an exponential function [150] at the higher energies. The average number of delayed neutrons per fission $\bar{\nu}_d$ and the delayed neutron spectra, if available, are adopted from the neutron nuclear data of JENDL-4.0, if a compound nuclide is the same as the target in the photon-incident case.

1. ^{40}Ca

The IAEA 1999 library [3] has the nuclear data of ^{40}Ca performed with the GNASH code at LANL. There are a few experimental data available for the evaluation: photo-absorption, $(\gamma, 1nX)$, $(\gamma, 1pX)$, (γ, Sn) and (γ, xn) reactions. The present evaluation was carried out by applying Murata's method. The photo-absorption cross section measured by Ahrens *et al.* [151] was reconstructed by 10 resonances, and this was also estimated from the $(\gamma, 1nX)$ reaction cross section of Veyssi re *et al.* [152]. The other particle emissions and residual production cross sections were calculated with ALICE-F.

Figure 32 shows the comparison of the present evaluation with previous evaluation [3] and measured data for photo-absorption, $(\gamma, 1nX)$ and $(\gamma, 1pX)$ reaction cross sections. The measurements of photo-absorption cross sections are for the natural Ca target. The comparison of the present evaluation of ^{40}Ca with the measured data is physically meaningful, since the abundance of ^{40}Ca accounts for 96.9% of natural Ca. The present evaluation gives similar photo-absorption cross section as the IAEA

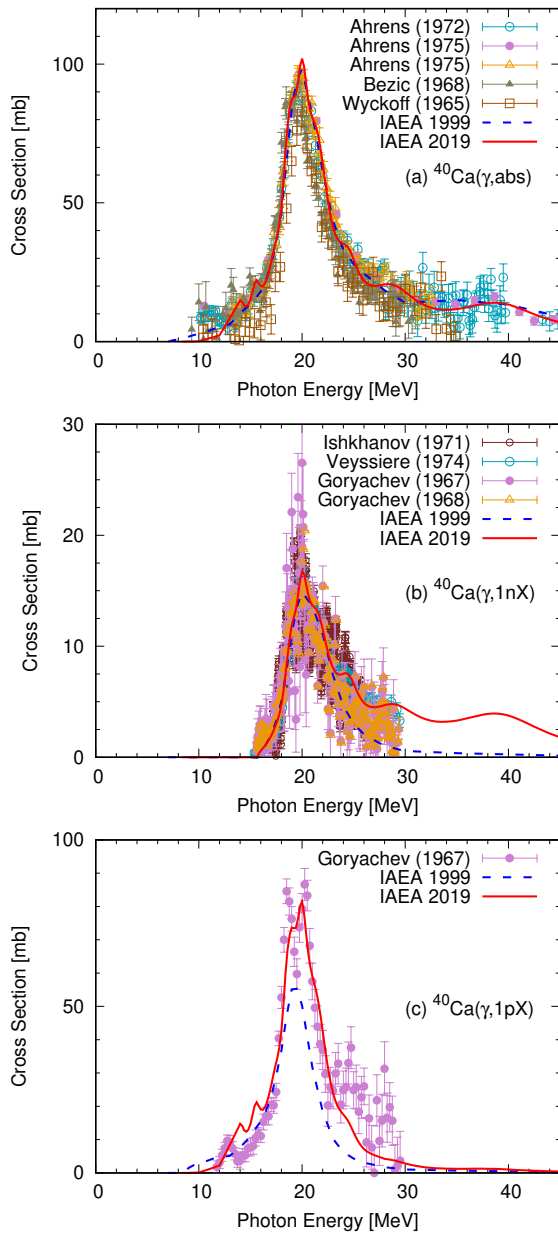


FIG. 32. (Color online) Comparisons of the present results with the evaluated (IAEA 1999) and experimental data for ^{40}Ca . The cross sections of (a) photo-absorption, (b) $(\gamma, 1nX)$ and (c) $(\gamma, 1pX)$ reactions are illustrated in each panel.

1999 library. The evaluated $(\gamma, 1p)$ reaction cross section is in good agreement with experimental data of Goryachev *et al.* [153] and higher than the previous evaluation in the IAEA 1999 library by 45% at the peak cross section.

2. ^{139}La

The photonuclear data of ^{139}La were not included in the IAEA 1999 library. New measurement was carried out at the NewSUBARU facility and provided the cross sections of $(\gamma, 1nX)$, $(\gamma, 2nX)$, $(\gamma, 3nX)$ and $(\gamma, 4nX)$ reactions. The measured data are compared with previous ones in Fig. 33. It is found that the $(\gamma, 1nX)$ and $(\gamma, 2nX)$ reaction cross sections of NewSUBARU are much higher than the previous ones. The present evaluation with the SMLO model for E1 photon strength function was made on the basis of the data measured at NewSUBARU.

The new evaluated cross sections for the $(\gamma, 1n)$, $(\gamma, 2n)$, $(\gamma, 3n)$ and $(\gamma, 4n)$ reactions are compared with JENDL/PD-2016 [154] in Fig. 33. The present evaluations are larger than JENDL/PD-2016, except for the $(\gamma, 1n)$ reaction cross section, where both evaluations agree since there is only one neutron emission below the threshold energy of $(\gamma, 2n)$ at 16.2 MeV. So, there is no ambiguity in detecting 1n or 2n neutrons. The recent data of Varlamov *et al.* have been evaluated on the basis of the old data of Beil *et al.* [155] from Saclay and are also smaller than those of NewSUBARU.

3. ^{239}Pu

The nuclear data of ^{239}Pu in the previous IAEA 1999 library was evaluated by IPPE. The energy region is limited to 20 MeV. The average number of prompt neutrons per fission $\bar{\nu}_p$ is given in the MF/MT=1/456 section (MF/MT combination defined in the ENDF-6 format), based on an estimation from neutron nuclear data of ^{238}Pu . The MF/MT=3/5 format is especially used as the sum of $(\gamma, 1n)$ and $(\gamma, 1np)$ reaction cross sections. The current new library adopts the data from JENDL/PD-2016, but with the incident energy range extended to 200 MeV. The evaluation was made with CCONE. $\bar{\nu}_p$ and $\bar{\nu}_d$ were included in the evaluation.

Figure 34 shows the comparison of the new evaluations with the previous IAEA 1999 library and the measured data for $(\gamma, 1nX)$, photo-fission and (γ, xn) reactions. The $(\gamma, 1nX)$ reaction cross section in the previous library shifts slightly to the lower energy region, relative to the measured data. The photo-fission cross sections are almost consistent with each other. The accuracy of this reaction cross section may be important for the development of inspection technology for nuclear fuel material. The small bump seen around 20 MeV comes from the contribution of third chance fission. This is not seen in the previous evaluation. The (γ, xn) reaction cross section has a contribution of fission neutrons as well as neutron emission cross sections multiplied by neutron multiplicity. The present (γ, xn) reaction cross section reproduces well the data of Berman *et al.* [148]. In contrast, the data in the previous library are lower than the measured data. This is attributed to the smaller $(\gamma, 2nX)$ reaction cross section.

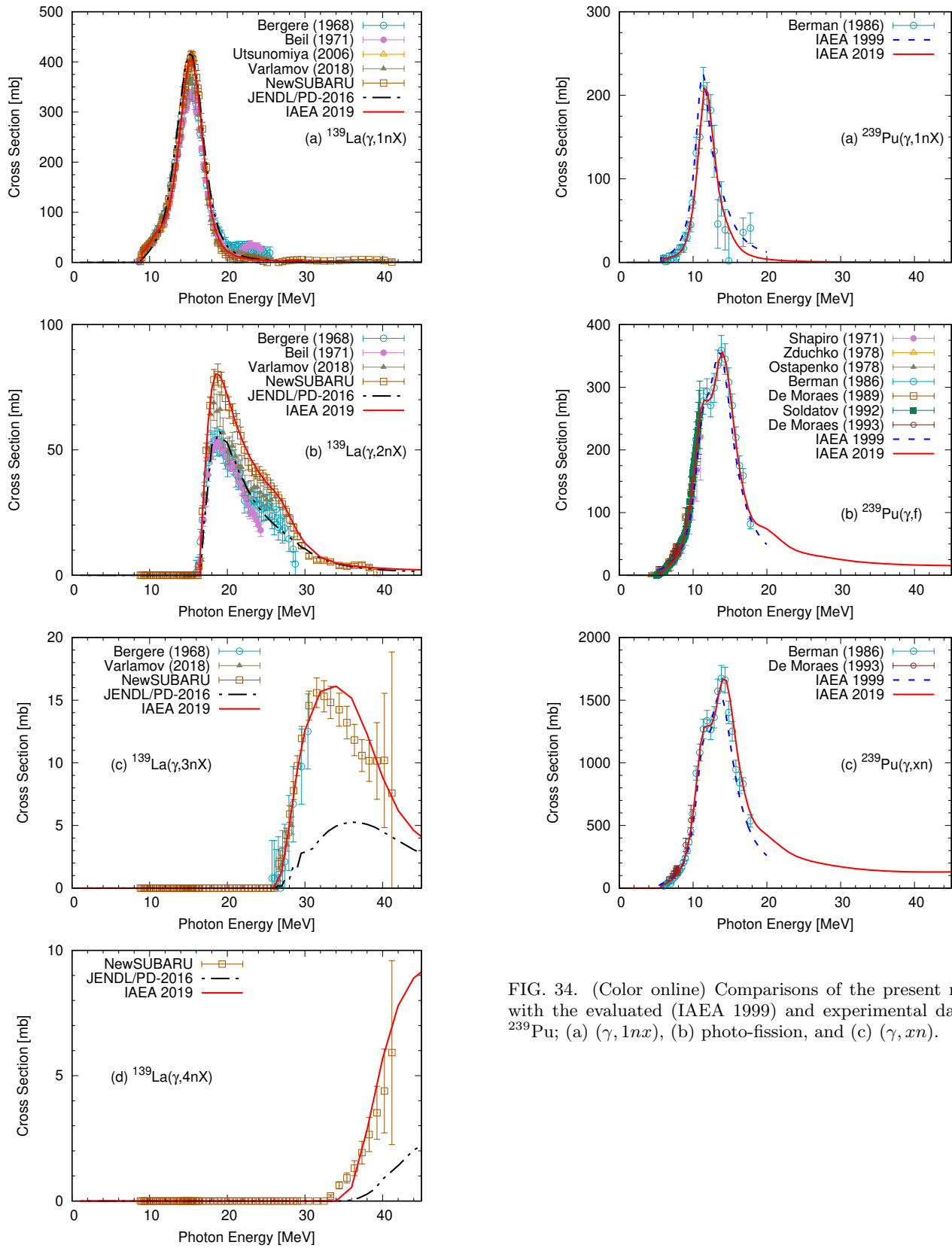


FIG. 34. (Color online) Comparisons of the present results with the evaluated (IAEA 1999) and experimental data for ^{239}Pu ; (a) $(\gamma, 1nX)$, (b) photo-fission, and (c) (γ, xn) .

FIG. 33. (Color online) Comparisons of the present photoneutron cross sections with the evaluated (JENDL/PD-2016) and experimental data for ^{139}La ; (a) $(\gamma, 1nX)$, (b) $(\gamma, 2nX)$, (c) $(\gamma, 3nX)$ and (d) $(\gamma, 4nX)$.

E. Data Evaluation at CIAE

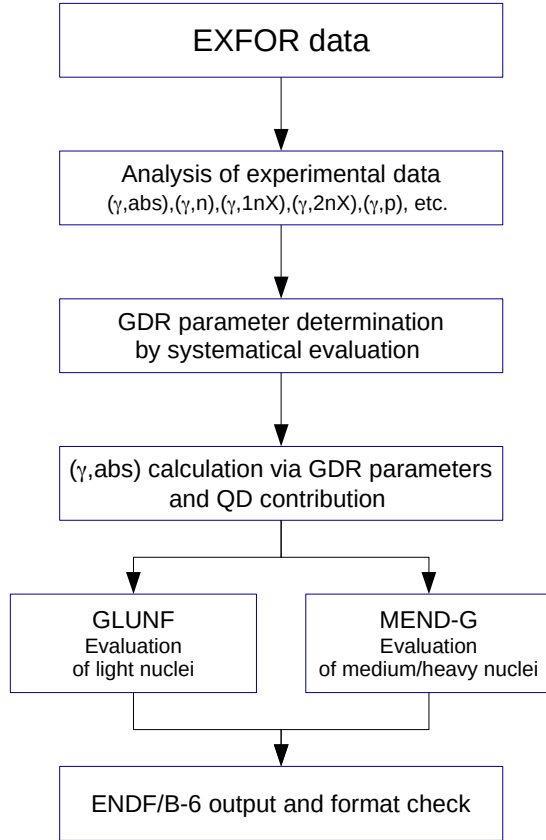


FIG. 35. Scheme of photonuclear data evaluation at CIAE/CNDC.

The evaluation scheme of photonuclear data at CIAE/CNDC is shown in Fig. 35. By collecting experimental data given in the EXFOR library, the following photonuclear reaction cross sections — (γ, abs) , (γ, xn) , $(\gamma, 1nX)$, $(\gamma, 2nX)$, $(\gamma, 3nX)$, $(\gamma, 1p)$, *etc.* — are recommended to guide our theoretical calculation. The new photonuclear reaction calculation systems, GLUNF for the light nuclei (${}^9\text{Be}$, ${}^{10,11}\text{B}$, ${}^{12}\text{C}$, ${}^{14}\text{N}$, and ${}^{16}\text{O}$) and MEND-G for the medium-heavy nuclei, are specially built for the incident γ -ray energy E_γ below 200 MeV under the corporation between CNDC and Nankai University. Reactions where up to eighteen particles are allowed to be emitted are considered in MEND-G, and the spherical optical model, equilibrium and pre-equilibrium statistical models are included in the code. Since determination of the scheme for competing particle emission is the most important in the light element case, a different reaction scheme in GLUNF is constructed for an individual photonuclear reaction chain for each of the light nuclei. Once the reaction chain was determined, the statistical theory of light-nucleus reaction [156, 157] is applied to calculate

all the reactions in the GLUNF code.

The photon strength function (PSF) used in deriving the photo-absorption cross sections is also systematically studied. For this purpose the code CPSF was developed at CNDC to produce the various PSFs, which includes several empirical Lorentzian functions [11], known as SLO, MLO1, MLO2, MLO3, EGLO, GFL, and SMLO. In addition, a semi-microscopic model, RQRPA, is also implemented in CPSF. In this calculation, we combine the GDR process below about 30 MeV and the phenomenological QD model up to 200 MeV.

1. ${}^9\text{Be}$

${}^9\text{Be}$ is a natural stable isotope of beryllium with the abundance of 100%. The evaluation in the previous IAEA 1999 library [3] was performed with the GLUNF code at CNDC. In the GLUNF reaction scheme used in our present evaluation, the photo-absorption cross section σ_{abs} is split into the reaction channels of $(\gamma, 2n)$, $(\gamma, 2n\alpha)$, (γ, np) , $(\gamma, n2\alpha)$, (γ, nd) , (γ, nt) , $(\gamma, 2np)$, (γ, pd) , $(\gamma, d\alpha)$, (γ, p_0) , (γ, p_1) , (γ, d_0) , (γ, d_1) , (γ, t_0) , (γ, t_1) , $(\gamma, {}^3\text{He}_0)$, and $(\gamma, {}^3\text{He}_1)$, where (γ, p_0) stands for the proton production by leaving the residual in its ground state.

The experimental data in EXFOR cover the data of σ_{abs} , (γ, n) , $(\gamma, 2n)$, and the charged particle emissions. In addition, the new NewSUBARU data for $(\gamma, n) + (\gamma, np)$ presented at this CRP are the main new experimental data used in our current update. Figure 36 compares our evaluated photo-absorption cross section with these experimental data. In the energy range 30–150 MeV, the evaluation of absorption cross section is based on the measurement of Ahrens *et al.* [151].

The new reaction chain scheme in GLUNF for ${}^9\text{Be}$ was developed at CNDC to evaluate the photonuclear data below 150 MeV. The optical model parameters were adjusted to the experimental data adopted in our evaluation. In Fig. 37, the calculated $(\gamma, n2\alpha)$ is compared with the available experimental data. The (γ, n) experimental data below 15 MeV were taken from EXFOR. Above 15 MeV, the measurement of Buchnea *et al.* [158] is compiled as the ${}^9\text{Be}(\gamma, n\alpha){}^4\text{He}$ reaction in EXFOR. The data shown by the filled circles are from the new measurement of Utsunomiya *et al.* reported in this CRP. The measurement of (γ, n) is represented by $(\gamma, n2\alpha)$. The results of $(\gamma, 2n)$ in our work are in good agreement with the experimental data of Utsunomiya as shown in Fig. 37. Also it is seen that the new evaluation is naturally extrapolated to the higher energy region oppose to the previous GLUNF evaluation, which predicts almost zero cross section of $(\gamma, n2\alpha)$ at 30 MeV.

2. ${}^{14}\text{N}$

${}^{14}\text{N}$ is a natural stable isotope of nitrogen, which has the largest abundance of 99.64%. A new evaluation

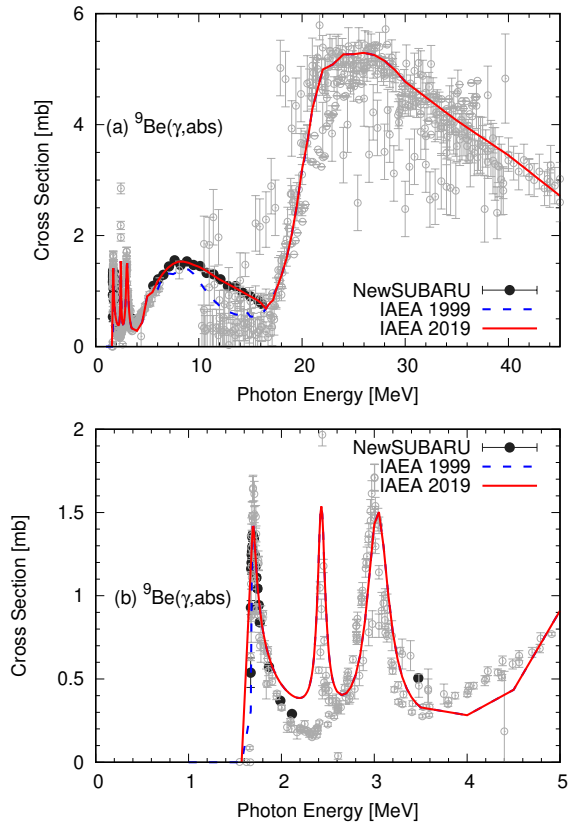


FIG. 36. (Color online) The evaluated photo-absorption cross section for ${}^9\text{Be}$. The bottom panel (b) is the zoom in the 1 – 5 MeV region. All the data are taken from EXFOR database, except for the NewSUBARU data shown by the filled circles.

for the photo-induced reaction on ${}^{14}\text{N}$ has been performed at CNDC. By setting up a reaction scheme in GLUNF, we produced σ_{abs} , $(\gamma, 2n)$, $(\gamma, n3\alpha)$, (γ, np) , (γ, nd) , $(\gamma, n^3\text{He})$, $(\gamma, nd2\alpha)$, $(\gamma, nt2\alpha)$, $(\gamma, n2p)$, (γ, n_0) , $(\gamma, 2\alpha)$, $(\gamma, 3\alpha)$, $(\gamma, 2p)$, $(\gamma, p\alpha)$, $(\gamma, t2\alpha)$, $(\gamma, d2\alpha)$, (γ, pd) , (γ, pt) , $(\gamma, d\alpha)$, as well as the proton, deuteron, triton, ${}^3\text{He}$, and α -particle emissions leaving the residuals in their discrete states.

The photo-absorption cross section is evaluated based on the measurement of Bezic *et al.* [159], which is shown in Fig. 38. Below 30 MeV, the $(\gamma, 1nX)$ cross section consists of the (γ, n) , (γ, np) and $(\gamma, np3\alpha)$ reactions in our estimation, and the comparison of evaluated and experimental data of $(\gamma, 1nX)$ is shown in Fig. 39. In Table I of Ref. [160], a relative yield of the (γ, np) reaction is reported to be 35%, while there are two channels given, 16% of (γ, n) and 11% of $(\gamma, 3\alpha pn)$, which produce one neutron. In addition, the residual of (γ, p) reaction at higher energies, ${}^{13}\text{C}^*$ undergoes neutron-decay, with a branching ratio estimated to be 28%. Since the data of Komar are for (γ, np) only, we multiplied their data by $(28 + 35 + 16 + 11)/35 = 2.57$. The re-scaled data better agree with other experimental data as well as our model

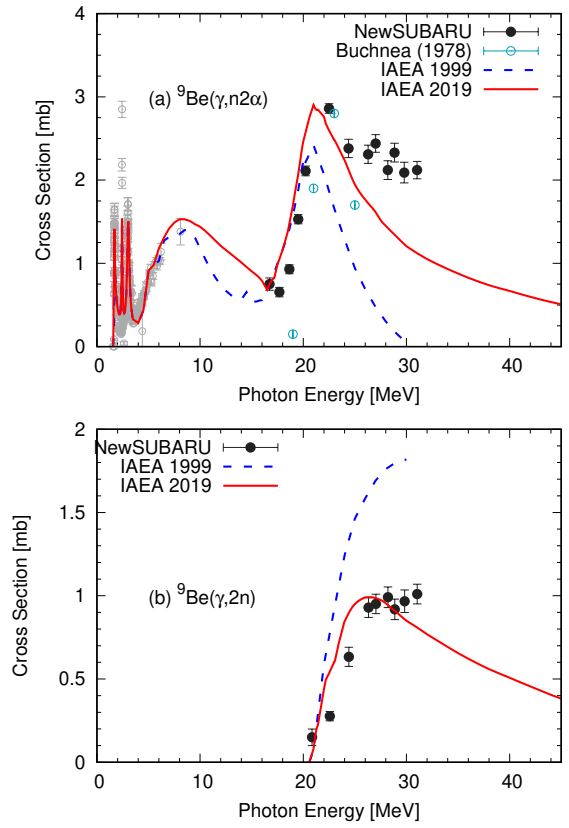


FIG. 37. (Color online) Comparison of the evaluated and experimental (a) ${}^9\text{Be}(\gamma, n2\alpha)$ and (b) $(\gamma, 2n)$ cross sections.

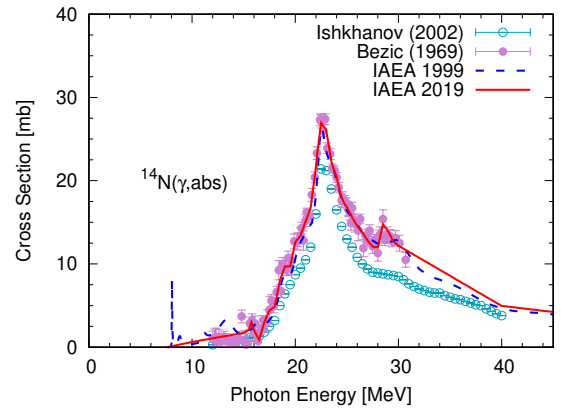


FIG. 38. (Color online) Comparison of evaluated and experimental data of the photo-absorption cross section for ${}^{14}\text{N}$.

calculation, as shown in Fig. 39.

The excited ${}^{14}\text{N}^*$ emits a neutron and the residual nucleus ${}^{13}\text{N}$ continues decaying by emitting a proton. The first excited state in ${}^{13}\text{N}$ would be 100% proton-decay and the probability of ${}^{13}\text{N}$ ground state production would be very small. This is predicted by our code as we get a very small (γ, n_0) cross section. In addition, $(\gamma, 2n)$ is

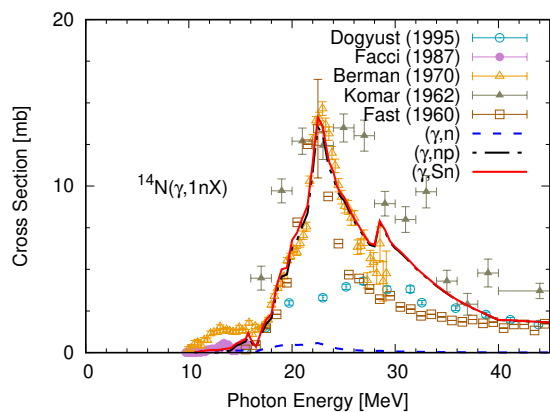


FIG. 39. (Color online) Comparison of evaluated and experimental data of neutron-production reaction cross sections, (γ, n) and (γ, np) for the photo-induced reaction on ^{14}N .

also included in GLUNF, although it has very small values, typically less than 0.01 mb.

3. ^{16}O

^{16}O is a natural stable isotope for oxygen with the abundance of 99.76%. We produced evaluated σ_{abs} and all of the exclusive cross sections for the $(\gamma, 2n)$, $(\gamma, n\alpha)$, $(\gamma, n3\alpha)$, (γ, np) , $(\gamma, n2\alpha)$, (γ, nd) , $(\gamma, n^3\text{He})$, $(\gamma, 2np)$, $(\gamma, n_0) - (\gamma, n_6)$, $(\gamma, 3\alpha)$, $(\gamma, 2p)$, $(\gamma, p\alpha)$, $(\gamma, t2\alpha)$, $(\gamma, d2\alpha)$, (γ, pd) , (γ, pt) , and $(\gamma, d\alpha)$ reactions, as well as the discrete transitions for the proton, deuteron, triton, ^3He , and α -particle emission reactions. As examples, the evaluated photo-absorption cross section and $(\gamma, 2n)$ reaction are shown in Figs. 40 and 41, respectively. A notable difference in the evaluated photo-absorption cross sections between the previous IAEA 1999 data file and the current evaluation is seen in the energy range below 20 MeV. While the older IAEA data have a resonance near 13 MeV, the new data exclude this peak. The new evaluation for the $(\gamma, 2n)$ reaction in Fig. 41 is significantly lower than the experimental data in the energy range above 40 MeV. We are unable to reproduce the data within our theoretical model framework, and we have no clear explanation for this. However, it should be noted that the previous evaluation, which employed a different statistical model, also shows the same tendency.

4. ^{27}Al

A new evaluation for ^{27}Al based on the MEND-G code calculation was adopted in the new photonuclear data library. The photo-absorption cross section is evaluated based on the experimental data of Ahrens *et al.* [151, 161], and the PSF calculation using the SMLO model. The evaluated photo-absorption cross section, shown in

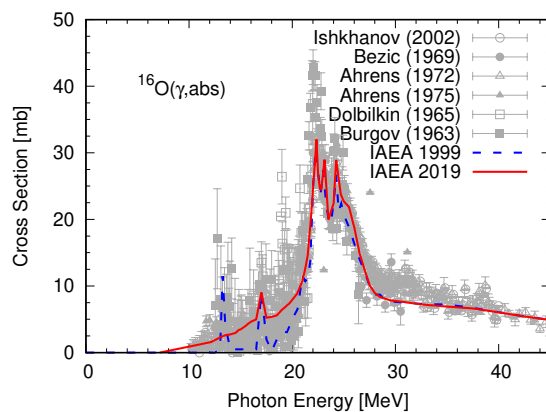


FIG. 40. (Color online) Comparison of theoretical results and experimental data for the photo-absorption cross section of ^{16}O .

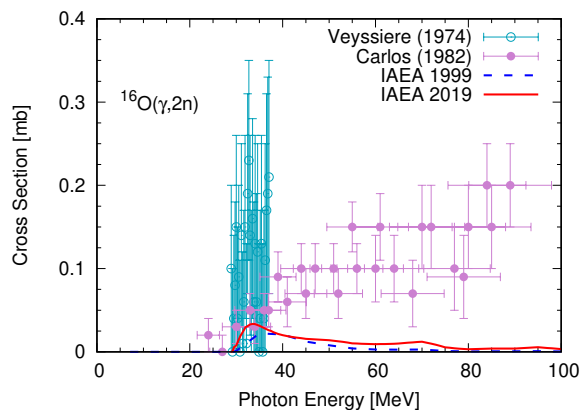


FIG. 41. (Color online) Comparison of evaluation and experimental data for the cross sections of $^{16}\text{O}(\gamma, 2n)^{14}\text{O}$.

Fig. 42 (a), is very similar to the older evaluation up to the GDR peak of 20 MeV, then tends to be higher at higher energies and agrees better with the Ahrens data.

The evaluated reaction cross sections are compared with measurements of Fultz *et al.* [162], Veyssi ere *et al.* [152], and Shoda *et al.* [163] in Fig. 42 (b)–(f). The new evaluations agree better with Fultz rather than Veyssi ere, although these data sets do not reveal critical discrepancies. In the case of the (γ, p) reaction shown in Fig. 42 (f), the experimental data of Shoda *et al.* are shifted to lower energies by 4 MeV to match the realistic reaction threshold energy.

5. ^{50}Cr

There are four natural stable isotopes for chromium, and all of them were evaluated by CIAE in the former IAEA Photonuclear data library. The new library includes an updated evaluation of ^{50}Cr whose abundance

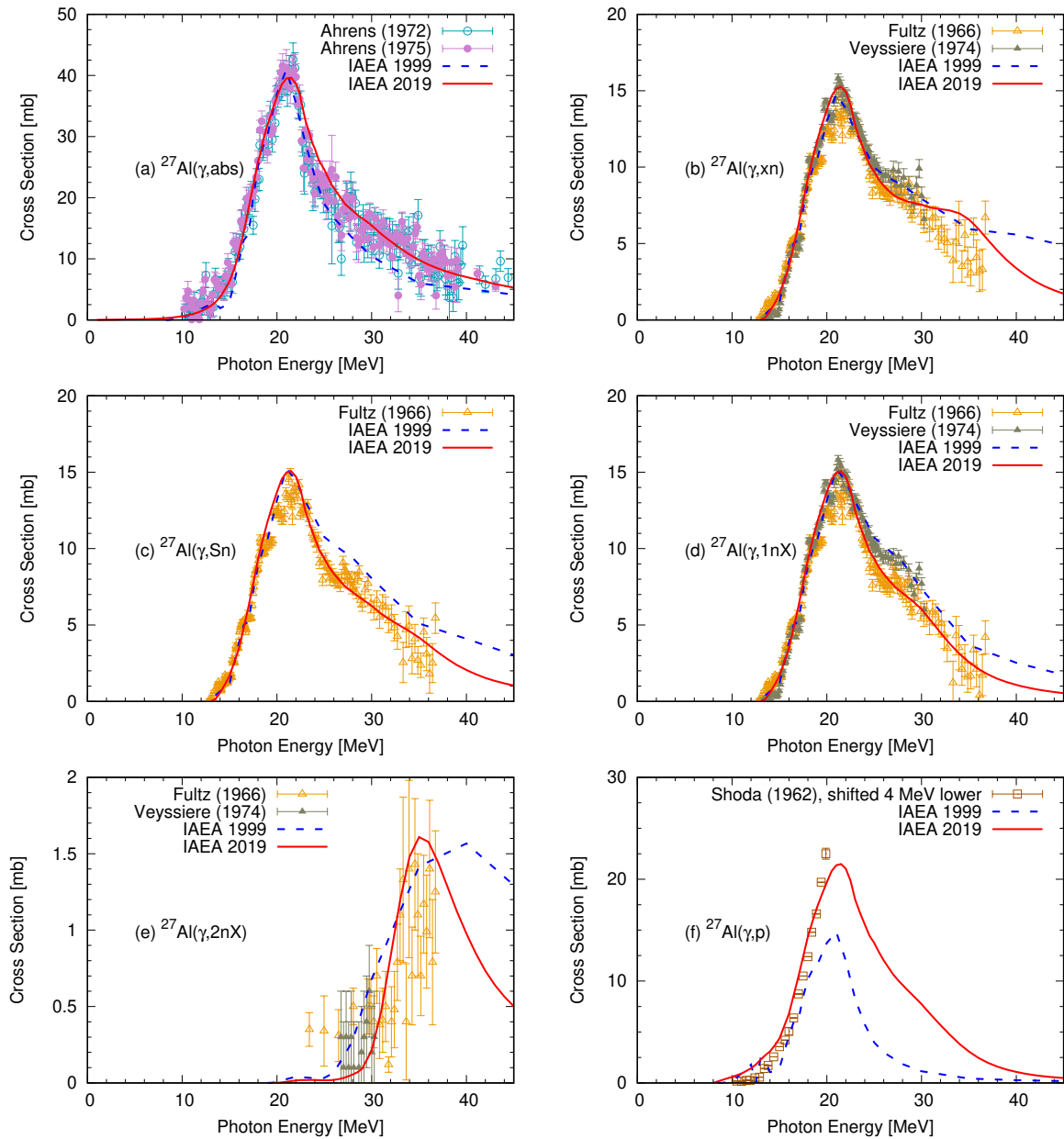


FIG. 42. (Color online) Comparison of evaluated and experimental data for ^{27}Al ; (a) photo-absorption, (b) σ_{xn} , (c) σ_{Sn} , (d) $(\gamma, 1n) + (\gamma, 1n + p)$, (e) $(\gamma, 2n) + (\gamma, 2n + p)$, and (f) (γ, p) reactions. In the panel (f), the data of Shoda *et al.* [163] are lower shifted by 4 MeV.

is 4.35%. On the other hand $^{53,54}\text{Cr}$ data were left unchanged, and the ^{52}Cr evaluation was replaced by a new JAEA evaluation.

The evaluation of the new ^{50}Cr data was performed with the MEND-G code. We employed the EGLO model for producing the photo-absorption cross section of ^{50}Cr . Figure 43 compares the current evaluation with some available experimental data for the (γ, n) reaction and the previous evaluation. The peak location of the new evaluation is slightly shifted toward the higher energy side, and the cross section drops rapidly above 25 MeV.

This is more physical as the number of open channels increases at higher energies.

6. ^{90}Zr

The natural zirconium includes five stable isotopes, and CIAE evaluated ^{90}Zr that has the largest abundance of 51.45%. The new evaluation was performed with the MEND-G code. The experimental data of Berman *et al.* [33] and Leprière *et al.* [128] are reported for

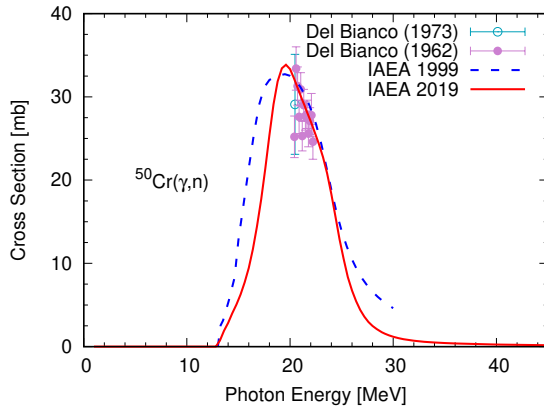


FIG. 43. (Color online) Comparison of evaluation and experimental data for $^{50}\text{Cr}(\gamma, n)$.

^{90}Zr . Varlamov *et al.* also published their evaluations of the partial neutron production cross sections [120] in 2018. As has been mentioned in previous sections, the data of Berman (Livermore) and Leprêtre (Saclay) show some inconsistencies. In this case, after considering all the available data, we decided to adopt Berman's data for our evaluation. SMLO is adopted to produce the photo-absorption cross sections. The evaluated photo-absorption cross section and the related neutron emission cross sections are in good agreement with the experimental data of Berman as shown in Fig. 44. We concluded that the Leprêtre data for σ_{1nX} and σ_{2nX} could have a neutron mis-counting issue, hence the current evaluation does not follow the Leprêtre data.

7. ^{118}Sn

There are 10 stable isotopes in natural tin. The IAEA photonuclear data library adopted ^{120}Sn from JENDL/PD-2016 [154], which has the largest abundance of 32.6%. CIAE undertook the evaluation of ^{118}Sn , whose abundance is the second largest of 24.22%. The experimental data of Fultz *et al.* [164] and Leprêtre [123] reported in 1960–1970s provide overall excitation functions of σ_{xn} and σ_{inX} for $i = 1, 2$ and 3. On the other hand, new neutron emission data by Utsunomiya *et al.* [165] were measured in 2011. Our evaluation strictly adopts the new data by Utsunomiya, which compare with the other experimental data as well as the corrected data by Varlamov *et al.* in the four panels of Fig. 45.

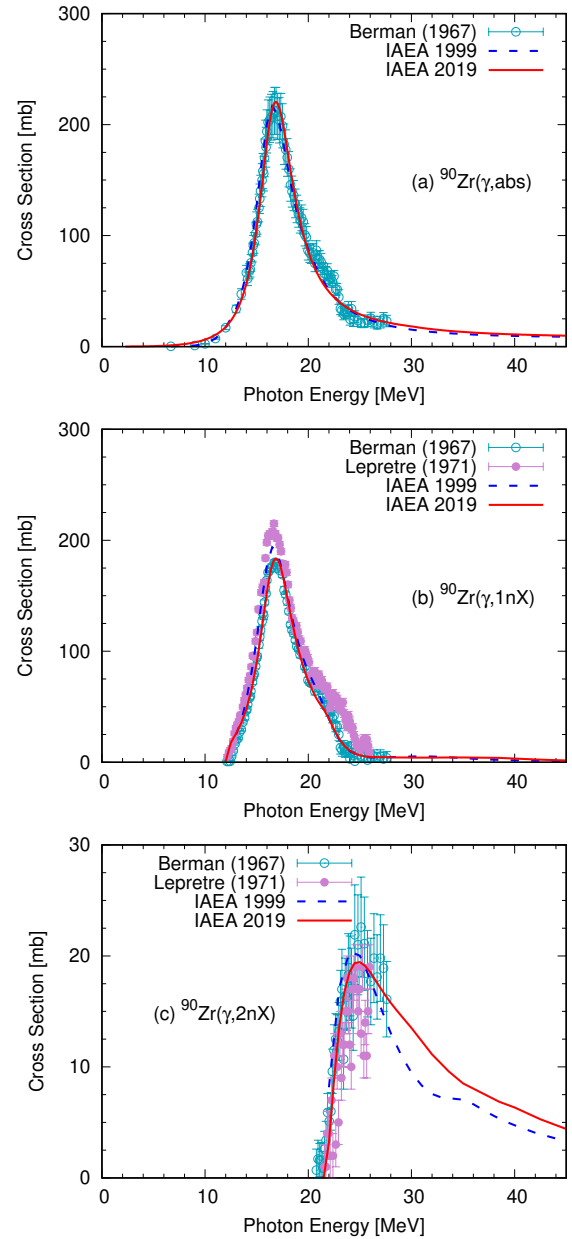


FIG. 44. (Color online) Comparison of evaluated and experimental data for ^{90}Zr ; (a) photo-absorption, (b) $(\gamma, n) + (\gamma, n + p)$, and (c) $(\gamma, 2n) + (\gamma, 2n + p)$ cross sections.

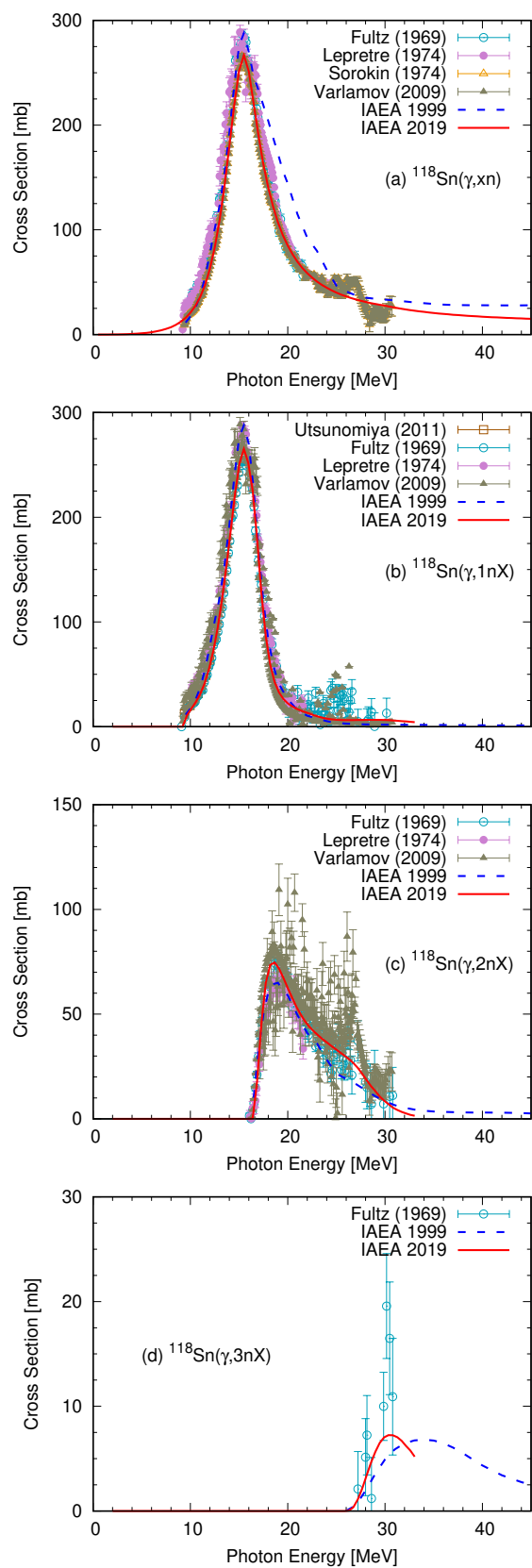


FIG. 45. (Color online) Comparison of evaluated and experimental data for ^{118}Sn ; (a) (γ, xn) , (b) $(\gamma, 1nX)$, (c) $(\gamma, 2nX)$, and (d) $(\gamma, 3nX)$

VI. CONTENTS OF THE LIBRARY

The new IAEA photonuclear data library contains photo-induced reaction data for 220 nuclides for photon energies up to 200 MeV. The energy and mass ranges are expanded compared to the previous 1999 version [3] which included 164 nuclides with the energies mostly up to 140 MeV. Here we call new library IAEA 2019. In Appendix A we summarize the source of evaluated data for each isotope in both IAEA 1999 and IAEA 2019.

Many of the isotopes evaluations included in IAEA 1999 originated from different evaluated nuclear data libraries maintained by different institutes. For example, the actinides data were taken from BOFOD [166], the JAERI evaluations were from JENDL photonuclear data file 2004 [136]. KAERI had significant contributions to both JENDL 2004 and IAEA 1999.

The sources of the IAEA 2019 library are classified into;

- New photonuclear data evaluations for IAEA 2019 at CNDC/CIAE, as well as special upgrades of their new upcoming CENDL (Chinese Evaluated Nuclear Data Library);
- JENDL Photonuclear Data File [154], and upgrades and high energy extension, as well as new evaluations specialized for IAEA 2019 at NDC/JAEA;
- New evaluations at IFIN-HH;
- New evaluations at NDC/KAERI; and
- Carry-over from IAEA 1999 photonuclear data library.

In some cases, the same isotopes were evaluated by more than one institutes. The inter-comparison of the different evaluations led to improvements in the evaluations performed by the individual institutes. They also triggered discussions on potential issues in the experimental data themselves, as most often, the differences in the evaluations were a result of adopting different experimental data sets. In the end, one set of evaluations was selected for these isotopes. The criteria for selection were based mainly on how well these evaluations reproduce the recommended available experimental data. An external review team that consisted of nuclear data evaluation experts, some of whom contributed to the previous IAEA 1999 library, reviewed the evaluations and following discussions with the evaluators arrived at a consensus on a unique set of the data library. It should be emphasized that all the evaluated data files that were produced within this CRP, including those that were not included in the new IAEA library, are of extremely good quality and could be available as part of other libraries such as CENDL, JENDL, *etc.* in near future.

The new IAEA Photonuclear Data Library is produced in the ENDF-6 format. The ENDF-6 format adopted for the stored cross sections and energy spectra depends on the isotopes, due to a difficulty in applying a common evaluation technique and format for all the isotopes. For some

nuclides, typically for light elements, exclusive nuclear reaction channels are explicitly given in MF=3 (MF: the file number defined in ENDF-6). While in many cases the MF=3 contains the total photo-absorption cross section only, and all individual information, such as the particle multiplicities and the residual nucleus production probabilities, is stored in MF=6. The MF=6 representation is the most common method since the library contains the high energy data part where the number of exclusive reaction channels exceeds the limitation of the ENDF-6 rule.

The new IAEA Photonuclear Data Library is available through the IAEA ENDF web interface (<http://www-nds.iaea.org/endl/>). In addition, users will be able to access all the graphical comparisons of the new evaluated data with experimental data and previous evaluations from a dedicated web interface that is under construction on the IAEA web server. The evaluated data will be downloadable as simple ascii files from this web interface as well.

VII. CONCLUSIONS

The new 2019 IAEA Photonuclear Data Library contains 220 isotopes, including 56 newly added data files. This library is one of the major final products of the IAEA CRP “Updating the Photonuclear Data Library and Generating a Reference Database for Photon Strength Functions.” The photon energy range was extended to 200 MeV to cover many applications of photonuclear data for radiation transport calculations as well as isotope production. In this paper we reviewed the experimental techniques used to measure photonuclear reaction cross sections, and summarized possible issues in the reported experimental data due to deficiencies in the techniques. We discussed the method of assessing published partial photoneutron cross section data developed by Varlamov *et al.*, to identify neutron mis-counting issues that lurk in the neutron-multiplicity sorting technique. The method which is based on the F_i correction factors, has been applied to several of the new evaluations, however, the need to consider the model-dependent uncertainties when applying it to correct the experimental data was highlighted in this review. One important accomplishment of this CRP was the completion of the new direct multiplicity counting technique at the NewSUBARU facility that led to new measurements of (γ, inX) cross sections for seven isotopes. These new data were considered in the new evaluations performed for the updated library.

The statistical Hauser-Feshbach model calculation was heavily involved in the data evaluation; GLUNF and MEND-G codes at CIAE, CCONE at JAEA, TALYS at KAERI, and EMPIRE at IFIN-HH. Since understanding characteristics of each Hauser-Feshbach code is crucial to estimate uncertainties coming from the limitation in the evaluation technique, a code inter-comparison was performed. The comparison also included the CoH₃ code

at LANL, as well as the CPNRM code at SINP/MSU, which was used for the F_i value correction to experimental data. We reported that the largest difference amongst the model codes is seen in the pre-equilibrium modeling in each code.

We assembled the new data library by collecting five main sources; new evaluations performed at CIAE along with some special upgrades of the new CENDL photodata library for the IAEA, JENDL/PD-2016 evaluations and new evaluations at JAEA, new evaluations at KAERI, and new evaluations at IFIN-HH based on the experimental data from NewSUBARU Laser Compton Scattering Facility, and some data files carried-over from the 1999 IAEA Photonuclear Data Library. Finally some selected comparisons of the newly evaluated data with available experimental data were given to demonstrate the improved evaluations over the previous IAEA data library. The new 2019 IAEA Photonuclear Data Library will be available on the IAEA web server (<http://www-nds.iaea.org/endlf>).

ACKNOWLEDGMENTS

This work was performed within the IAEA CRP on “Updating the Photonuclear Data Library and Generat-

ing a Reference Database for Photon Strength Functions” (F41032). Contributors from the following institutes are grateful to the IAEA for financial support within the CRP: CIAE, KAERI, IFIN-HH, Taras Shevchenko National University, Lomonosov Moscow State University, Centre for Energy Research (HAS), Charles University (Prague), and iThemba LABS. The work described in this paper would not have been possible without contributions by the IAEA member states. HU acknowledges support extended to the PHOENIX collaboration for the IAEA-CRP by the Premier Project of Konan University. YC was supported by the R&D program of the Korea Atomic Energy Research Institute funded by the Korean Ministry of Science and ICT. TK carried out this work under the auspices of the National Nuclear Security Administration of the U.S. Department of Energy at Los Alamos National Laboratory under Contract No. 89233218CNA000001.

-
- [1] B. L. Berman, “Atlas of photoneutron cross sections obtained with monoenergetic photons,” *AT. DATA NUCL. DATA TABLES* **15**, 319 (1975).
- [2] S. S. Dietrich and B. L. Berman, “Atlas of photoneutron cross sections obtained with monoenergetic photons,” *AT. DATA NUCL. DATA TABLES* **38**, 199 (1988).
- [3] “Handbook on photonuclear data for applications. cross-sections and spectra, final report of a co-ordinated research project 1996–1999,” *Tech. Rep. IAEA-TECDOC-1178*, International Atomic Energy Agency (2000).
- [4] D. Habs and U. Köster, “Production of medical radioisotopes with high specific activity in photonuclear reactions with γ -beams of high intensity and large brilliance,” *APPL. PHYS. B* **103**, 501 (2011).
- [5] A. L. Nichols and R. Capote, “Nuclear data for medical applications — recent developments and future requirements,” *NUCL. DATA SHEETS* **120**, 239 (2014).
- [6] A. L. Nichols, S. M. Qaim, and R. Capote Noy, “Summary report of the technical meeting on intermediate-term nuclear data needs for medical applications: Cross sections and decay data,” *Tech. Rep. INDC(NDS)-0596*, International Atomic Energy Agency (2011).
- [7] A. L. Nichols, F. M. Nortier, and R. Capote Noy, “Summary report of third research coordination meeting on nuclear data for charged-particle monitor reactions and medical isotope production,” *Tech. Rep. INDC(NDS)-0717*, International Atomic Energy Agency (2016).
- [8] V. A. Plujko, O. M. Gorbachenko, R. Capote, and P. Dimitriou, “Giant dipole resonance parameters of ground-state photoabsorption: Experimental values with uncertainties,” *AT. DATA NUCL. DATA TABLES* **123–124**, 1 (2018).
- [9] N. Otuka, E. Dupont, V. Semkova, *et al.*, “Towards a more complete and accurate experimental nuclear reaction data library (EXFOR): International collaboration between nuclear reaction data centres (NRDC),” *NUCL. DATA SHEETS* **120**, 272 (2014).
- [10] H. Utsunomiya, I. Gheorghe, D. M. Filipescu, *et al.*, “Direct neutron-multiplicity sorting with a flat-efficiency detector,” *NUCL. INST. METH. A* **871**, 135 (2017).
- [11] S. Goriely, P. Dimitriou, M. Wiedeking, *et al.*, “Reference database for photon strength functions,” *EUR. PHYS. J. A* (2019) [submitted to EPJA].
- [12] V. V. Varlamov, B. S. Ishkhanov, V. N. Orlin, and S. Y. Troshchiev, “New data for $^{197}\text{Au}(\gamma, nx)$ and $^{197}\text{Au}(\gamma, 2nx)$ reaction cross sections,” *BULL. RUS. ACAD. SCI.* **74** (2010).
- [13] O. V. Bogdankevich and F. A. Nikolaev, *Methods in Bremsstrahlung Research*. New York, USA: Academic Press (1966).
- [14] E. Van Camp, R. Van de Vyver, E. Kerkhove, D. Ryckbosch, H. Ferdinande, P. Van Otten, and P. Berkvens, “Experimental determination of the proton escape width in the giant dipole resonance of ^{89}Y ,” *PHYS. REV. C* **24**, 2499 (1981).
- [15] A. S. Penfold and J. E. Leiss, “Analysis of photonuclear cross sections,” *PHYS. REV.* **114**, 1332 (1959).
- [16] E. Bramanis, T. K. Deague, R. Hicks, R. S. Hughes, E. G. Muirhead, R. H. Sambell, and R. J. J. Stewart, “The analysis of photonuclear yield curves,” *NUCL. INST. METH.* **100**, 59 (1972).

- [17] A. N. Tikhonov, V. G. Shevchenko, V. Galkin, B. I. Goryachev, P. N. Zaikin, B. Ishkhanov, and I. M. Kapitonov, "About the determination of photonuclear reaction cross-sections," *VESTNIK MOSKOVSKOGO UNIV. FIZ. ASTRON.* **2**, 208 (1970).
- [18] B. C. Cook, "Least structure solution of photonuclear yield functions," *NUCL. INST. METH.* **24**, 256 (1963).
- [19] K. N. Geller and E. G. Muirhead, "Photoneutron cross section of oxygen," *PHYS. REV. LETT.* **11**, 371 (1963).
- [20] V. F. Turchin, V. P. Kozlov, and M. S. Malkevich, "The use of mathematical-statistics methods in the solution of incorrectly posed problems," *SOV. PHYS. USPEKHI* **13**, 681 (1971).
- [21] A. Tzara, "A method of producing a narrow spectrum of high-energy photons," *COMPTES RENDUS ACAD. SCI.* **56** (1957).
- [22] B. L. Berman and S. C. Fultz, "Measurements of the giant dipole resonance with monoenergetic photons," *REV. MOD. PHYS.* **47**, 713 (1975).
- [23] S. C. Fultz, R. L. Bramblett, J. T. Caldwell, and N. A. Kerr, "Photoneutron cross-section measurements on gold using nearly monochromatic photons," *PHYS. REV.* **127**, 1273 (1962).
- [24] L. S. Cardman, *Photon tagging, present practice and future prospects*. Univ. of Illinois at Urbana-Champaign Dept. of Physics Report R/83/12/168 (1983).
- [25] H. Ohgaki, H. Toyokawa, K. Kudo, N. Takeda, and T. Yamazaki, "Generation and application of laser-compton gamma-ray at ETL," *NUCL. INST. METH. A* **455**, 54 (2000).
- [26] S. Amano, K. Horikawa, K. Ishihara, S. Miyamoto, T. Hayakawa, T. Shizuma, and T. Mochizuki, "Several-MeV γ -ray generation at NewSUBARU by laser Compton backscattering," *NUCL. INST. METH. A* **602**, 337 (2009).
- [27] K. Horikawa, S. Miyamoto, S. Amano, and T. Mochizuki, "Measurements for the energy and flux of laser Compton scattering γ -ray photons generated in an electron storage ring: NewSUBARU," *NUCL. INST. METH. A* **618**, 209 (2010).
- [28] H. Utsunomiya, S. Hashimoto, and S. Miyamoto, "The γ -ray beam-line at NewSUBARU," *NUCL. PHYS. NEWS* **25**, 25 (2015).
- [29] H. Utsunomiya, T. Shima, K. Takahisa, *et al.*, "Energy calibration of the NewSUBARU storage ring for laser Compton-scattering gamma rays and applications," *IEEE TRANS. ON NUCL. SCI.* **61**, 1252 (2014).
- [30] T. Kii, T. Baba, Y. Nagai, H. Ohgaki, T. Shima, and H. Toyokawa, "Photon counting method for high flux pulsed laser-compton backscattered photons based on poisson model," *12TH SYMP. ON ACCEL. SCI. TECHNOL. WAKO, JPN. 27 - 29 OCT 1999*, 484.
- [31] T. Kondo, H. Utsunomiya, H. Akimune, T. Yamagata, A. Okamoto, H. Harada, F. Kitatani, T. Shima, K. Horikawa, and S. Miyamoto, "Determination of the number of pulsed laser-compton scattering photons," *NUCL. INST. METH. A* **659**, 462 (2011).
- [32] H. Utsunomiya, T. Watanabe, T. Ari-izumi, *et al.*, "Photon-flux determination by the poisson-fitting technique with quenching corrections," *NUCL. INST. METH. A* **896**, 103 (2018).
- [33] B. L. Berman, J. T. Caldwell, R. R. Harvey, M. A. Kelly, R. L. Bramblett, and S. C. Fultz, "Photoneutron cross sections for Zr^{90} , Zr^{91} , Zr^{92} , Zr^{94} , and Y^{89} ," *PHYS. REV.* **162**, 1098 (1967).
- [34] E. Wolynec, A. R. V. Martinez, P. Gouffon, Y. Miyao, V. A. Serrão, and M. N. Martins, "Comment on photoneutron cross sections," *PHYS. REV. C* **29**, 1137 (1984).
- [35] E. Wolynec and M. N. Martins, "Discrepancies between Saclay and Livermore photoneutron cross sections," *REVISTA BRASILEIRA DE FISICA* **17**, 56 (1987).
- [36] V. V. Varlamov and B. S. Ishkhanov, "Study of consistency between (γ, xn) , $[(\gamma, n) + (\gamma, np)]$ and $(\gamma, 2n)$ reaction cross sections using data systematics," Tech. Rep. INDC(CCP)-433, International Atomic Energy Agency (2002).
- [37] S. S. Belyshev, B. S. Ishkhanov, A. A. Kuznetsov, V. N. Orlin, K. A. Stopani, V. V. Khankin, and N. V. Shvedunov, "Photodisintegration of cadmium isotopes," *PHYS. ATOM. NUCL.* **77**, 809 (2014).
- [38] S. S. Belyshev, D. M. Filipescu, I. Gheoghe, *et al.*, "Multinucleon photonuclear reactions on ^{209}Bi : Experiment and evaluation," *EUR. PHYS. J. A* **51**, 67 (2015).
- [39] H. Naik, G. Kim, K. Kim, M. Zaman, A. Goswami, M. W. Lee, S.-C. Yang, Y.-O. Lee, S.-G. Shin, and M.-H. Cho, "Measurement of flux-weighted average cross sections for $^{197}\text{Au}(\gamma, xn)$ reactions and isomeric yield ratios of $^{196m, g}\text{Au}$ with bremsstrahlung," *NUCL. PHYS. A* **948**, 28 (2016).
- [40] H. Utsunomiya, A. Makinaga, S. Goko, *et al.*, "Photoneutron cross section measurements on the $N = 82$ nuclei ^{139}La and ^{141}Pr : Implications for p -process nucleosynthesis," *PHYS. REV. C* **74**, 025806 (2006).
- [41] O. Itoh, H. Utsunomiya, H. Akimune, *et al.*, "Photoneutron cross sections for Au revisited: Measurements with laser Compton scattering γ -rays and data reduction by a least-squares method," *J. NUCL. SCI. TECHNOL.* **48**, 834 (2011).
- [42] H. Utsunomiya, H. Akimune, S. Goko, *et al.*, "Cross section measurements of the $^{181}\text{Ta}(\gamma, n)^{180}\text{Ta}$ reaction near neutron threshold and the p -process nucleosynthesis," *PHYS. REV. C* **67**, 015807 (2003).
- [43] H. Utsunomiya, S. Goriely, H. Akimune, *et al.*, "Photoneutron cross sections for ^{90}Zr : A systematic experimental study of photoneutron and radiative neutron capture cross sections for zirconium isotopes," *PHYS. REV. C* **81**, 035801 (2010).
- [44] T. Kondo, H. Utsunomiya, S. Goriely, *et al.*, "Total and partial photoneutron cross sections for Pb isotopes," *PHYS. REV. C* **86**, 014316 (2012).
- [45] H. Utsunomiya, S. Goriely, T. Kondo, *et al.*, "Photoneutron cross sections for Mo isotopes: A step toward a unified understanding of (γ, n) and (n, γ) reactions," *PHYS. REV. C* **88**, 015805 (2013).
- [46] T. Renstrøm, H. Utsunomiya, H. T. Nyhus, *et al.*, "Verification of detailed balance for γ absorption and emission in Dy isotopes," *PHYS. REV. C* **98**, 054310 (2018).
- [47] I. Gheorghe, H. Utsunomiya, S. Katayama, *et al.*, "Photoneutron cross-section measurements in the $^{209}\text{Bi}(\gamma, xn)$ reaction with a new method of direct neutron-multiplicity sorting," *PHYS. REV. C* **96**, 044604 (2017).
- [48] V. I. Antonescu, "IAEA bibliographical series, photonuclear reactions," Tech. Rep. 10, International Atomic Energy Agency, Vienna, Austria (1964).
- [49] E. G. Fuller and H. Gerstenberg, *Photonuclear data - abstract sheets 1955 - 1982. Report of the US National*

- Bureau of Standards, NBSIR 83 - 2742, I - XV.* National Institute of Standards and Technology, Gaithersburg (1983).
- [50] V. V. Varlamov, V. V. Sapunenko, and M. E. Stepanov, *Photonuclear data index 1976–1995*. Moscow State University (1996).
- [51] T. Asami and T. Nakagawa, “Bibliographic index to photonuclear reaction data (1955 – 1992),” Tech. Rep. JAERI-M-93-195, INDC(JPN)-167L, Japan Atomic Energy Research Institute, Ibaraki-ken, Japan (1993).
- [52] V. V. Varlamov, “CDFE online services,” <http://cdfe.sinp.msu.ru/services/pnisearch.html>
- [53] “Handbook on nuclear activation data,” Tech. Rep. Technical Report Series No.273, International Atomic Energy Agency (1987).
- [54] A. I. Blokhon and S. M. Nasyrova, “Plots of the experimental and evaluated photonuclear cross-sections,” Tech. Rep. INDC(CCP)-337, International Atomic Energy Agency (1991).
- [55] A. V. Varlamov, V. V. Varlamov, D. S. Rudenko, and M. E. Stepanov, “Atlas of giant dipole resonances, parameters and graphs of photonuclear reaction cross sections,” Tech. Rep. INDC(NDS)-394, International Atomic Energy Agency (1999).
- [56] A. Schiller and M. Thoennessen, “Compilation of giant electric dipole resonances built on excited states,” *AT. DATA NUCL. DATA TABLES* **93**, 549 (2007).
- [57] V. A. Plujko, R. Capote, and O. M. Gorbachenko, “Giant dipole resonance parameters with uncertainties from photonuclear cross sections,” *AT. DATA NUCL. DATA TABLES* **97**, 567 (2011).
- [58] R. Capote, M. Herman, P. Obložinský, *et al.*, “RIPL — reference input parameter library for calculation of nuclear reactions and nuclear data evaluations,” *NUCL. DATA SHEETS* **110**, 3107 (2009).
- [59] V. McLane, “EXFOR systems manual nuclear reaction data exchange format,” Tech. Rep. BNL-NCS-63330-00/04-REV;KB0401040, Brookhaven National Laboratory (2000).
- [60] N. Otsuka and S. Dunaeva, “International network of nuclear reaction data centres,” Tech. Rep. INDC(NDS)-401, International Atomic Energy Agency (2010).
- [61] V. V. Zerkin and B. Pritychenko, “The experimental nuclear reaction data (EXFOR): Extended computer database and Web retrieval system,” *NUCL. INST. METH. A* **888**, 31 (2018).
- [62] J. S. Levinger, “The high energy nuclear photoeffect,” *PHYS. REV.* **84**, 43 (1951).
- [63] J. S. Levinger, “Modified quasi-deuteron model,” *PHYS. LETT. B* **82**, 181 (1979).
- [64] C. M. McCullagh, M. L. Stelts, and R. E. Chrien, “Dipole radiative strength functions from resonance neutron capture,” *PHYS. REV. C* **23**, 1394 (1981).
- [65] J. Kopecky and M. Uhl, “Test of gamma-ray strength functions in nuclear reaction model calculations,” *PHYS. REV. C* **41**, 1941 (1990).
- [66] J. Kopecky, M. Uhl, and R. E. Chrien, “Radiative strength in the compound nucleus ^{157}Gd ,” *PHYS. REV. C* **47**, 312 (1993).
- [67] T. Nakatsukasa, T. Inakura, and K. Yabana, “Finite amplitude method for the solution of the random-phase approximation,” *PHYS. REV. C* **76**, 024318 (2007).
- [68] S. Péru and M. Martini, “Mean field based calculations with the Gogny force: Some theoretical tools to explore the nuclear structure,” *THE EUR. PHYS. J. A* **50**, 88 (2014).
- [69] V. A. Plujko, O. M. Gorbachenko, V. M. Bondar, and R. Capote, “Renewed database of GDR parameters for atomic nuclei,” *J. KOREAN PHYS. SOC.* **59**, 1514 (2011).
- [70] M. B. Chadwick, P. Obložinský, P. E. Hodgson, and G. Reffo, “Pauli-blocking in the quasideuteron model of photoabsorption,” *PHYS. REV. C* **44**, 814 (1991).
- [71] H. Feshbach, A. Kerman, and S. Koonin, “The statistical theory of multi-step compound and direct reactions,” *ANNALS PHYS.* **125**, 429 (1980).
- [72] M. Herman, R. Capote, B. V. Carlson, P. Obložinský, M. Sin, A. Trkov, H. Wienke, and V. Zerkin, “EMPIRE: Nuclear reaction model code system for data evaluation,” *NUCL. DATA SHEETS* **108**, 2655 (2007).
- [73] M. Herman, R. Capote, M. Sin, *et al.*, “EMPIRE-3.2 Malta, modular system for nuclear reaction calculations and nuclear data evaluation user’s manual,” Tech. Rep. INDC(NDS)-0603, International Atomic Energy Agency (2013).
- [74] A. J. Koning, S. Hilaire, and M. C. Duijvestijn, “TALYS-1.0,” *EPJ WEB CONF.*, 211 (2008). *Proc. Int. Conf. on Nuclear Data for Science and Technology*, 22 – 27 Apr., 2007, Nice, France, (Eds.) O. Bersillon, F. Gungor, E. Bauge, R. Jacqmin, and S. Leray.
- [75] O. Iwamoto, N. Iwamoto, S. Kunieda, F. Minato, and K. Shibata, “The CCONE code system and its application to nuclear data evaluation for fission and other reactions,” *NUCL. DATA SHEETS* **131**, 259 (2016).
- [76] T. Kawano, “CoH₃: The coupled-channels and hauser-feshbach code,” (2019). CNR2018: International Workshop on Compound Nucleus and Related Topics, LBNL, Berkeley, CA, USA, September 24 – 28, 2018, (Ed.) J. Escher.
- [77] F. C. Williams, “Particle-hole state density in the uniform spacing model,” *NUCL. PHYS. A* **166**, 231 (1971).
- [78] E. Běták and J. Dobeš, “The finite depth of the nuclear potential well in the exciton model of preequilibrium decay,” *Z. FÜR PHYSIK A* **279**, 319 (1976).
- [79] M. B. Chadwick and P. G. Young, “Feshbach-Kerman-Koonin analysis of ^{93}Nb reactions: P→Q transitions and reduced importance of multistep compound emission,” *PHYS. REV. C* **47**, 2255 (1993).
- [80] T. Kawano, “Microscopic calculation of the multistep compound process,” *PHYS. REV. C* **59**, 865 (1999).
- [81] W. Hauser and H. Feshbach, “The inelastic scattering of neutrons,” *PHYS. REV.* **87**, 366 (1952).
- [82] M. B. Chadwick, P. G. Young, and S. Chiba, “Photonuclear angular distribution systematics in the quasideuteron regime,” *J. NUCL. SCI. TECHNOL.* **32**, 1154 (1995).
- [83] C. Kalbach, “Systematics of continuum angular distributions: Extensions to higher energies,” *PHYS. REV. C* **37**, 2350 (1988).
- [84] A. J. Koning and J.-P. Delaroche, “Local and global nucleon optical models from 1 keV to 200 MeV,” *NUCL. PHYS. A* **713**, 231 (2003).
- [85] P. G. Young and E. D. Arthur, “GNASH, a pre-equilibrium, statistical nuclear-model code for calculation of cross sections and emission spectra,” Tech. Rep. LA-6947, Los Alamos National Laboratory (1977).
- [86] P. G. Young, E. D. Arthur, and M. B. Chadwick, “Comprehensive nuclear model calculations: Introduction to the theory and use of the GNASH code,” Tech. Rep.

- LA-12343-MS, Los Alamos National Laboratory (1992).
- [87] T. Fukahori, "ALICE-F calculation of nuclear data up to 1 GeV," *JAERI-M* **92-039**, 114 (1992).
- [88] N. Kishida and H. Kadotani, "On the validity of the intranuclear-cascade and evaporation model for high energy proton induced reactions," *PROC. INT. CONF. NUCL. DATA FOR SCI. TECHNOL.*, 1209 (1989). Mito, Japan, May 30 – June 3, 1988, (Ed.) S. Igarasi (Saikon Publishing Co. Ltd, Tokyo).
- [89] Z. Zhang, "Illustration on photonuclear data calculation with GUNF code," *COMM. NUCL. DATA PROG.* **19**, 33 (1998).
- [90] Z. Zhang, "Illustration on photonuclear data calc. with GLUNF code," *COMM. NUCL. DATA PROG.* **22**, (1999).
- [91] A. Blokhin, "The XGFISS code for analysis of photonuclear cross-sections for actinide nuclei," *YADERNYE KONSTANTY* **2** (1999).
- [92] R. Capote, S. Hilaire, O. Iwamoto, T. Kawano, and M. Sin, "Inter-comparison of Hauser-Feshbach model codes toward better actinide evaluations," *EPJ WEB CONF.* **146**, 12034 (2017). ND 2016: International Conference on Nuclear Data for Science and Technology, Bruges, Belgium, September 11 – 16, 2016, (Eds.) A. Plompen, F.-J. Hamsch, P. Schillebeeckx, W. Mondelaers, J. Heyse, S. Kopecky, P. Siegler and S. Oberstedt.
- [93] T. Kawano, P. Talou, and H. A. Weidenmüller, "Random-matrix approach to the statistical compound nuclear reaction at low energies using the Monte Carlo technique," *PHYS. REV. C* **92**, 044617 (2015).
- [94] C.-H. Cai, "MEND-A code for calculating nuclear data of medium-heavy nuclei below 250 MeV," *NUCL. PHYS. REV.* **28**, 354 (2011).
- [95] B. S. Ishkhanov and V. N. Orlin, "Semimicroscopic description of the giant dipole resonance," *PHYS. PART. NUCL.* **38**, 232 (2007).
- [96] B. S. Ishkhanov and V. N. Orlin, "Preequilibrium model of photonucleon reactions that is based on Fermi gas densities," *PHYS. ATOM. NUCL.*, 493 (2008).
- [97] S. Watanabe, "High energy scattering of deuterons by complex nuclei," *NUCL. PHYS.* **8**, 484 (1958).
- [98] V. Avrigeanu, P. E. Hodgson, and M. Avrigeanu, "Global optical potentials for emitted alpha particles," *PHYS. REV. C* **49**, 2136 (1994).
- [99] M. Avrigeanu, A. C. Obreja, F. L. Roman, V. Avrigeanu, and W. von Oertzen, "Complementary optical-potential analysis of α -particle elastic scattering and induced reactions at low energies," *AT. DATA NUCL. DATA TABLES* **95**, 501 (2009).
- [100] M. Avrigeanu and V. Avrigeanu, " α -particle nuclear surface absorption below the Coulomb barrier in heavy nuclei," *PHYS. REV. C* **82**, 014606 (2010).
- [101] V. Avrigeanu, M. Avrigeanu, and C. Mănăilescu, "Further explorations of the α -particle optical model potential at low energies for the mass range $A \approx 45$ –209," *PHYS. REV. C* **90**, 044612 (2014).
- [102] H. An and C. Cai, "Global deuteron optical model potential for the energy range up to 183 MeV," *PHYS. REV. C* **73**, 054605 (2006).
- [103] J. Bojowald, H. Machner, H. Nann, W. Oelert, M. Rogge, and P. Turek, "Elastic deuteron scattering and optical model parameters at energies up to 100 MeV," *PHYS. REV. C* **38**, 1153 (1988).
- [104] F. D. Becchetti and G. W. Greenlees, "Nucleon-nucleus optical-model parameters, $A > 40$, $E < 50$ MeV," *PHYS. REV.* **182**, 1190 (1969).
- [105] F. D. Becchetti and G. W. Greenlees, "Standard optical model parameters," *Tech. Rep.*, University of Minnesota (1969).
- [106] Y. Han, Y. Shi, and Q. Shen, "Deuteron global optical model potential for energies up to 200 MeV," *PHYS. REV. C* **74**, 044615 (2006).
- [107] Y. Xu, H. Guo, and Y. Han, "Helium-3 global optical model potential with energies below 250 MeV," *SCI. CHINA PHYS. MECH. ASTRON.* **54**, 2005 (2011).
- [108] V. V. Varlamov, B. S. Ishkhanov, V. N. Orlin, N. N. Peskov, and M. E. Stepanov, "New data on (γ, n) , $(\gamma, 2n)$, and $(\gamma, 3n)$ partial photoneutron reactions," *PHYS. ATOM. NUCL.* **76**, 1403 (2013).
- [109] V. V. Varlamov, B. S. Ishkhanov, and V. N. Orlin, "New approach to analyzing and evaluating cross sections for partial photoneutron reactions," *PHYS. ATOM. NUCL.* **75**, 1339 (2012).
- [110] V. V. Varlamov, B. S. Ishkhanov, V. N. Orlin, and K. A. Stopani, "A new approach for analysis and evaluation of partial photoneutron reaction cross sections," *EUR. PHYS. J. A* **50**, 114 (2014).
- [111] B. S. Ishkhanov, V. N. Orlin, and V. V. Varlamov, "Total and partial photoneutron reactions cross sections - new analysis and evaluation," *EPJ WEB CONF.* **38**, 12003 (2012).
- [112] V. V. Varlamov, M. A. Makarov, N. N. Peskov, and M. E. Stepanov, "New data on cross sections for partial and total photoneutron reactions on the isotopes $^{91,94}\text{Zr}$," *PHYS. ATOM. NUCL.* **78**, 634 (2015).
- [113] V. Varlamov, M. Makarov, N. Peskov, and M. Stepanov, "Photodisintegration of the isotopes $^{186,188,189,190,192}\text{Os}$: Similarities and distinctions," *PHYS. ATOM. NUCL.* **78**, 746 (2015).
- [114] V. V. Varlamov, A. I. Davydov, M. A. Makarov, V. N. Orlin, and N. N. Peskov, "Reliability of the data on the cross sections of the partial photoneutron reaction for $^{63,65}\text{Cu}$ and ^{80}Se nuclei," *BULL. RUS. ACAD. SCI.* **80**, 317 (2016).
- [115] V. V. Varlamov, B. S. Ishkhanov, V. N. Orlin, and N. N. Peskov, "Data on photoneutron reactions from various experiments for ^{133}Cs , ^{138}Ba and ^{209}Bi nuclei," *PHYS. ATOM. NUCL.* **79**, 501 (2016).
- [116] S. C. Fultz, R. L. Bramblett, J. T. Caldwell, and R. R. Harvey, "Photoneutron cross sections for natural Cu, Cu^{63} , and Cu^{65} ," *PHYS. REV.* **133**, B1149 (1964).
- [117] V. V. Varlamov, A. I. Davydov, and B. S. Ishkhanov, "Photoneutron cross sections for ^{59}Co : Systematic uncertainties of data from various experiments," *EUR. PHYS. J. A* **53**, 180 (2017).
- [118] S. C. Fultz, R. L. Bramblett, J. T. Caldwell, N. E. Hansen, and C. P. Jupiter, "Photoneutron cross sections for V^{51} and Co^{59} ," *PHYS. REV.* **128**, 2345 (1962).
- [119] R. A. Alvarez, B. L. Berman, D. D. Faul, F. H. Lewis, and P. Meyer, "Photoneutron cross sections for ^{55}Mn and ^{59}Co ," *PHYS. REV. C* **20**, 128 (1979).
- [120] V. V. Varlamov, A. I. Davydov, B. S. Ishkhanov, and V. N. Orlin, "The reliability of photoneutron cross sections for $^{90,91,92,94}\text{Zr}$," *EUR. PHYS. J. A* **54**, 74 (2018).
- [121] B. S. Ishkhanov, V. N. Orlin, and S. Y. Troschiev, "Photodisintegration of tantalum," *PHYS. ATOM. NUCL.* **75**, 253 (2012).
- [122] V. Varlamov, B. Ishkhanov, and V. Orlin, "Experimental and evaluated photoneutron cross sections for

- ¹⁹⁷Au,” *PHYS. REV. C* **96**, 044606 (2017).
- [123] A. Leprêtre, H. Beil, R. Bergère, P. Carlos, A. De Miniac, A. Veyssièrre, and K. Kernbach, “A study of the giant dipole resonance of vibrational nuclei in the $103 \leq A \leq 133$ mass region,” *NUCL. PHYS. A* **219**, 39 (1974).
- [124] B. L. Berman, R. L. Bramblett, J. T. Caldwell, H. S. Davis, M. A. Kelly, and S. C. Fultz, “Photoneutron cross sections for As⁷⁵, Ag¹⁰⁷, and Cs¹³³,” *PHYS. REV.* **177**, 1745 (1969).
- [125] B. L. Berman, S. C. Fultz, J. T. Caldwell, M. A. Kelly, and S. S. Dietrich, “Photoneutron cross sections for Ba¹³⁸ and N¹⁴,” *PHYS. REV. C* **2**, 2318 (1970).
- [126] A. Leprêtre, H. Beil, R. Bergère, P. Carlos, J. Fagot, A. De Miniac, A. Veyssièrre, and H. Miyase, “A study of the giant dipole resonance in doubly even tellurium and cerium isotopes,” *NUCL. PHYS. A* **258**, 350 (1976).
- [127] E. B. Bazhanov, A. P. Komar, and A. V. Kulikov, “Photoneutrons from Li⁶ and Co⁵⁹,” *SOV. PHYS. JETP* **19**, 1014 (1964).
- [128] A. Leprêtre, H. Beil, R. Bergère, P. Carlos, A. Veyssièrre, and M. Sugawara, “The giant dipole states in the $A = 90$ mass region,” *NUCL. PHYS. A* **175**, 609 (1971).
- [129] R. W. Parsons, “The photodisintegration of manganese and rhodium,” *CAN. J. PHYS.* **37**, 1344 (1959).
- [130] O. V. Bogdankevich, B. I. Goryachev, and V. A. Zapevalov, “Splitting of the giant dipole resonance in medium-heavy nuclei,” *J. EXP. THEOR. PHYS.* **15**, 1044 (1962).
- [131] R. L. Bramblett, J. T. Caldwell, R. R. Harvey, and S. C. Fultz, “Photoneutron cross sections of Tb¹⁵⁹ and O¹⁶,” *PHYS. REV.* **133**, B869 (1964).
- [132] R. Bergère, H. Beil, and A. Veyssièrre, “Photoneutron cross sections of La, Tb, Ho and Ta,” *NUCL. PHYS. A* **121**, 463 (1968).
- [133] B. I. Goryachev, Y. V. Kuznetsov, V. N. Orlin, N. A. Pozhidaeva, and V. G. Shevchenko, “Giant resonance in strongly deformed nuclei Tb-159, Ho-165, Er-166, and Hf-178,” *YAD. FIZ.* **23**, 1145 (1976).
- [134] B. L. Berman, M. A. Kelly, R. L. Bramblett, J. T. Caldwell, H. S. Davis, and S. C. Fultz, “Giant resonance in deformed nuclei: Photoneutron cross sections for Eu¹⁵³, Gd¹⁶⁰, Ho¹⁶⁵, and W¹⁸⁶,” *PHYS. REV.* **185**, 1576 (1969).
- [135] G. M. Gurevich, L. E. Lazareva, V. M. Mazur, S. Y. Merkulov, G. V. Solodukhov, and V. A. Tyutin, “Total nuclear photoabsorption cross sections in the region $150 < A < 190$,” *NUCL. PHYS. A* **351**, 257 (1981).
- [136] N. Kishida, T. Murata, T. Asami, K. Kosako, K. Maki, H. Harada, Y. Lee, J. Chang, S. Chiba, and T. Fukahori, “JENDL photonuclear data file,” **769**, 199 (2004). Proceedings of International Conference on Nuclear Data for Science and Technology, Santa Fe, New Mexico, USA, Sep. 26 – Oct. 1, 2004, (Eds.) R.C. Haight, M.B. Chadwick, T. Kawano, P. Talou.
- [137] R. L. Bramblett, J. T. Caldwell, G. F. Auchampaugh, and S. C. Fultz, “Photoneutron cross sections of Ta¹⁸¹ and Ho¹⁶⁵,” *PHYS. REV.* **129**, 2723 (1963).
- [138] P. Obložinský, “Summary report of the 1st research co-ordination meeting on compilation and evaluation of photonuclear data for applications,” Tech. Rep. INDC(NDS)-364, IAEA Nuclear Data Section Vienna, Austria (1996).
- [139] S. N. Belyaev and V. P. Sinichkin, *Precision photonuclear experiment for investigation of ¹⁸¹Ta GDR intermediate structure*. Workshop on Beam Dynamics and Optimiz, Saratov 2001, p.81, Russia (2001).
- [140] E. G. Fuller and M. S. Weiss, “Splitting of the giant resonance for deformed nuclei,” *PHYS. REV.* **112**, 560 (1958).
- [141] G. P. Antropov, I. E. Mitrofanov, and B. S. Russkikh, “Photoneutron reactions on Al, S, Ta, and Bi,” *Izv. ROSSIJSKOI AKADEMII NAUK, SER.FIZ.* **31**, 336 (1967).
- [142] G. M. Gurevich, L. E. Lazareva, V. M. Mazur, and G. V. Solodukhov, “Width of giant resonance in the absorption for the cross sections of gamma-rays by nuclei in the region $150 < A < 200$,” *ZHURNAL EKSPER. I TEOR. FIZ., PISMA V REDAKT.* **23**, 411 (1976).
- [143] S. Goko, H. Utsunomiya, S. Goriely, *et al.*, “Partial photoneutron cross sections for the isomeric state ¹⁸⁰Ta^m,” *PHYS. REV. LETT.* **96**, 192501 (2006).
- [144] T. Murata, K. Kosaka, and T. Fukahori, “Renewal of JENDL photonuclear data file 2004 (I) elements of atomic number below 20,” *JAEA-CONF* **2011-002**, 235 (2011).
- [145] “Handbook for calculations of nuclear reaction data, RIPL-2 reference input parameter library-2,” Tech. Rep. IAEA-TECDOC-1506, International Atomic Energy Agency (2006).
- [146] A. Gilbert and A. G. W. Cameron, “A composite nuclear-level density formula with shell corrections,” *CAN. J. PHYS.* **43**, 1446 (1965).
- [147] A. Mengoni and Y. Nakajima, “Fermi-gas model parametrization of nuclear level density,” *J. NUCL. SCI. TECHNOL.* **31**, 151 (1994).
- [148] B. L. Berman, J. T. Caldwell, E. J. Dowdy, S. S. Dietrich, P. Meyer, and R. A. Alvarez, “Photofission and photoneutron cross sections and photofission neutron multiplicities for ²³³U, ²³⁴U, ²³⁷Np, and ²³⁹Pu,” *PHYS. REV. C* **34**, 2201 (1986).
- [149] J. T. Caldwell, E. J. Dowdy, R. A. Alvarez, B. L. Berman, and P. Meyer, “Experimental determination of photofission neutron multiplicities for ²³⁵U, ²³⁶U, ²³⁸U, and ²³²Th using monoenergetic photons,” *NUCL. SCI. ENG.* **73**, 153 (1980).
- [150] T. Ethvignot, M. Devlin, H. Duarte, T. Granier, R. C. Haight, B. Morillon, R. O. Nelson, J. M. O’Donnell, and D. Rochman, “Neutron multiplicity in the fission of ²³⁸U and ²³⁵U with neutrons up to 200 MeV,” *PHYS. REV. LETT.* **94**, 052701 (2005).
- [151] J. Ahrens, H. Borchert, K. Czock, *et al.*, “Total nuclear photon absorption cross sections for some light elements,” *NUCL. PHYS. A* **251**, 479 (1975).
- [152] A. Veyssièrre, H. Beil, R. Bergère, P. Carlos, A. Leprêtre, and A. De Miniac, “A study of the photoneutron contribution to the giant dipole resonance of s-d shell nuclei,” *NUCL. PHYS. A* **227**, 513 (1974).
- [153] B. I. Goryachev, B. S. Ishkhanov, I. M. Kapitonov, I. M. Piskarev, V. G. Shevchenko, and O. P. Shevchenko, “Structure of the gross section the reaction Ca⁴⁰(γ , p),” *JETP LETT.* **5** (1967).
- [154] N. Iwamoto, K. Kosako, and T. Murata, “Photonuclear data file,” *JAEA-CONF* 2016-004, 53 (2016).
- [155] H. Beil, R. Bergere, P. Carlos, A. Lepretre, A. Veyssièrre, and A. Parlag, “Giant dipole resonance in $N = 82$ nuclei,” *NUCL. PHYS. A* **172**, 426 (1971).
- [156] X. Sun and J. Zhang, “New integral formula for obtaining analytical Legendre expansion coefficients and its applications to light-nucleus reactions,” *PHYS. REV. C*

- 92**, 061601 (2015).
- [157] X. Sun and J. Zhang, “Statistical theory of light-nucleus reactions and application to the ${}^9\text{Be}(p, xn)$ reaction,” *PHYS. REV. C* **93**, 014609 (2016).
- [158] A. Buchnea, R. G. Johnson, and K. G. McNeill, “Alpha particles from the photodisintegration of ${}^9\text{Be}$ in the photon energy region 18 to 26 MeV,” *CAN. J. PHYS.* **56**, 47 (1978).
- [159] N. Bezić, D. Brajnik, D. Jamnik, and G. Kernel, “Total photonuclear cross sections for ${}^{12}\text{C}$, ${}^{14}\text{N}$, ${}^{16}\text{O}$ and ${}^{19}\text{F}$ in the region of the giant resonance,” *NUCL. PHYS. A* **128**, 426 (1969).
- [160] A. P. Komar, Y. Krzhemenek, and I. P. Yavor, “Photodisintegration of nitrogen,” *NUCL. PHYS.* **34**, 551 (1962).
- [161] J. Ahrens, H. Borchert, H. B. Eppler, H. Gimm, H. Gundrum, P. Riehn, G. Sita Ram, A. Zieger, M. Kröning, and B. Ziegler, “Total cross sections for the nuclear photoeffect,” *PROC. INT. CONF. NUCL. STRUCT. STUDIES, SENDAI, JPN.* (1972).
- [162] S. C. Fultz, J. T. Caldwell, B. L. Berman, R. L. Bramblett, and R. R. Harvey, “Photoneutron cross sections for C^{12} and Al^{27} ,” *PHYS. REV.* **143**, 790 (1966).
- [163] K. Shoda, K. Abe, T. Ishizuka, N. Kawamura, and M. Kimura, “Photoproton cross sections for Mg, Al, Si and S,” *J. PHYS. SOC. JPN.* **17**, 735 (1962).
- [164] S. C. Fultz, B. L. Berman, J. T. Caldwell, R. L. Bramblett, and M. A. Kelly, “Photoneutron cross sections for Sn^{116} , Sn^{117} , Sn^{118} , Sn^{119} , Sn^{120} , Sn^{124} , and indium,” *PHYS. REV.* **186**, 1255 (1969).
- [165] H. Utsunomiya, S. Goriely, M. Kamata, *et al.*, “Photoneutron cross sections for ${}^{118-124}\text{Sn}$ and the γ -ray strength function method,” *PHYS. REV. C* **84**, 055805 (2011).
- [166] A. I. Blokhin, N. N. Buleeva, S. M. Nasyrova, O. A. Pakhomova, S. V. Zabrodszkaya, and A. M. Tsibulya, “Formation and application of evaluated photoneutron data library BOFOD,” *YADERNYE KONSTANTY* **3**, 3 (1992).
- [167] Y. Zhuang, T. Liu, J. Zhang, and P. Liu, “CENDL-3 - chinese evaluated nuclear data library, version 3,” *J. NUCL. SCI. TECHNOL.* **39**, 37 (2002).

**Appendix A: Contents of IAEA 1999 and 2019
Photonuclear Data Libraries**

In the following table, we summarize the source of evaluated file for each isotope. In the IAEA 1999 column, an institute name that undertook the evaluation is given. When this column is empty, no evaluation is given in IAEA 1999. In the IAEA 2019 column, JENDL/PD-2016 means these files were taken from JENDL Photonuclear Data File 2016 [154], the = sign indicates the IAEA 1999 data were carried over, and the institution names stand for the new evaluations performed at each institute.

TABLE II. Contents of IAEA 1999 and 2019 photonuclear data libraries. The source of the data or leading evaluation institute is given. The = sign means the 2019 library is the same as 1999.

Nuclide	IAEA 1999	IAEA 2019
² H	JAERI	=
³ He		JENDL/PD-2016
⁶ Li		JENDL/PD-2016
⁷ Li		JENDL/PD-2016
⁹ Be	CIAE	CIAE
¹² C	LANL	CIAE
¹³ C	KAERI	=
¹⁴ C		KAERI
¹⁴ N	JAERI	CIAE
¹⁵ N	KAERI	=
¹⁶ O	LANL	=
¹⁷ O	KAERI	=
¹⁸ O	KAERI	=
¹⁹ F		JENDL/PD-2016
²³ Na	KAERI	=
²⁴ Mg	KAERI	=
²⁵ Mg	KAERI	=
²⁶ Mg	KAERI	=
²⁷ Al	LANL	CIAE
²⁷ Si	KAERI	=
²⁸ Si	KAERI	=
²⁹ Si	KAERI	=
³⁰ Si	KAERI	=
³² S	KAERI	=
³³ S	KAERI	=
³⁴ S	KAERI	=
³⁶ S	KAERI	=
³⁵ Cl	KAERI	JAEA
³⁷ Cl	KAERI	JAEA
³⁶ Ar	KAERI	JAEA
³⁸ Ar	KAERI	JAEA
⁴⁰ Ar	KAERI	JAEA
³⁹ K	KAERI	JAEA
⁴⁰ K	KAERI	JAEA
⁴¹ K	KAERI	JAEA
⁴⁰ Ca	LANL	JENDL/PD-2016
⁴² Ca	KAERI	=
⁴³ Ca	KAERI	=
⁴⁴ Ca	KAERI	JENDL/PD-2016
⁴⁶ Ca	KAERI	=

TABLE II continued.

Nuclide	IAEA 1999	IAEA 2019
⁴⁸ Ca	KAERI	JENDL/PD-2016
⁴⁵ Sc		JAEA
⁴⁶ Ti	KAERI	JAEA
⁴⁷ Ti	KAERI	JAEA
⁴⁸ Ti	KAERI	JAEA
⁴⁹ Ti	KAERI	JAEA
⁵⁰ Ti	KAERI	JAEA
⁵⁰ V		JAEA
⁵¹ V	CIAE	JAEA
⁵⁰ Cr	CIAE	CIAE
⁵² Cr	CIAE	JAEA
⁵³ Cr	CIAE	=
⁵⁴ Cr	CIAE	=
⁵⁵ Mn	KAERI	JAEA
⁵⁴ Fe	JAERI	JAEA
⁵⁶ Fe	JAERI	JAEA
⁵⁷ Fe	KAERI	JAEA
⁵⁸ Fe	KAERI	JAEA
⁵⁹ Co	KAERI	IFIN-HH
⁵⁸ Ni	JAERI	JAEA
⁶⁰ Ni	KAERI	JAEA
⁶¹ Ni	KAERI	JAEA
⁶² Ni	KAERI	JAEA
⁶⁴ Ni	KAERI	JAEA
⁶³ Cu	LANL	JAEA
⁶⁵ Cu	JAERI	JAEA
⁶⁴ Zn	JAERI	KAERI
⁶⁶ Zn	KAERI	JENDL/PD-2016
⁶⁷ Zn	KAERI	JENDL/PD-2016
⁶⁸ Zn	KAERI	JENDL/PD-2016
⁷⁰ Zn	KAERI	JENDL/PD-2016
⁷⁰ Ge	KAERI	JENDL/PD-2016
⁷² Ge	KAERI	JENDL/PD-2016
⁷³ Ge	KAERI	JENDL/PD-2016
⁷⁴ Ge	KAERI	JENDL/PD-2016
⁷⁶ Ge	KAERI	JENDL/PD-2016
⁷⁵ As		KAERI
⁷⁶ Se		KAERI
⁷⁸ Se		KAERI
⁸⁰ Se		KAERI
⁸⁴ Sr	KAERI	JENDL/PD-2016
⁸⁶ Sr	KAERI	JENDL/PD-2016
⁸⁷ Sr	KAERI	JENDL/PD-2016
⁸⁸ Sr	KAERI	JENDL/PD-2016
⁹⁰ Sr	KAERI	JENDL/PD-2016
⁸⁹ Y		IFIN-HH
⁹⁰ Zr	KAERI	CIAE
⁹¹ Zr	CIAE	KAERI
⁹² Zr	CIAE	JENDL/PD-2016
⁹³ Zr	KAERI	JENDL/PD-2016
⁹⁴ Zr	KAERI	KAERI
⁹⁶ Zr	CIAE	JENDL/PD-2016
⁹³ Nb	KAERI	JENDL/PD-2016
⁹⁴ Nb	KAERI	JENDL/PD-2016
⁸² Se		KAERI

TABLE II continued.

Nuclide	IAEA 1999	IAEA 2019
⁹² Mo	KAERI	JENDL/PD-2016
⁹⁴ Mo	KAERI	JENDL/PD-2016
⁹⁵ Mo	KAERI	JENDL/PD-2016
⁹⁶ Mo	KAERI	JENDL/PD-2016
⁹⁷ Mo	KAERI	JENDL/PD-2016
⁹⁸ Mo	KAERI	JENDL/PD-2016
¹⁰⁰ Mo	KAERI	JENDL/PD-2016
⁹⁸ Ru		JAEA
¹⁰³ Rh		IFIN-HH
¹⁰² Pd	KAERI	JENDL/PD-2016
¹⁰⁴ Pd	KAERI	JENDL/PD-2016
¹⁰⁵ Pd	KAERI	JENDL/PD-2016
¹⁰⁶ Pd	KAERI	JENDL/PD-2016
¹⁰⁷ Pd	KAERI	JENDL/PD-2016
¹⁰⁸ Pd	KAERI	JENDL/PD-2016
¹¹⁰ Pd	KAERI	JENDL/PD-2016
¹⁰⁷ Ag	KAERI	JENDL/PD-2016
¹⁰⁸ Ag	KAERI	JAEA
¹⁰⁹ Ag	KAERI	JENDL/PD-2016
¹⁰⁶ Cd	KAERI	JENDL/PD-2016
¹⁰⁸ Cd	KAERI	JENDL/PD-2016
¹¹⁰ Cd	KAERI	JENDL/PD-2016
¹¹¹ Cd	KAERI	JENDL/PD-2016
¹¹² Cd	KAERI	JENDL/PD-2016
¹¹³ Cd	KAERI	JENDL/PD-2016
¹¹⁴ Cd	KAERI	JENDL/PD-2016
¹¹⁶ Cd	KAERI	JENDL/PD-2016
¹¹⁵ In		KAERI
¹¹² Sn	KAERI	JENDL/PD-2016
¹¹⁴ Sn	KAERI	JENDL/PD-2016
¹¹⁵ Sn	KAERI	JENDL/PD-2016
¹¹⁶ Sn	KAERI	KAERI
¹¹⁷ Sn	KAERI	JENDL/PD-2016
¹¹⁸ Sn	KAERI	CIAE
¹¹⁹ Sn	KAERI	JENDL/PD-2016
¹²⁰ Sn	KAERI	JENDL/PD-2016
¹²² Sn	KAERI	JENDL/PD-2016
¹²⁴ Sn	KAERI	JENDL/PD-2016
¹²¹ Sb	KAERI	JENDL/PD-2016
¹²³ Sb	KAERI	JENDL/PD-2016
¹²⁰ Te	KAERI	JENDL/PD-2016
¹²² Te	KAERI	JENDL/PD-2016
¹²³ Te	KAERI	JENDL/PD-2016
¹²⁴ Te	KAERI	JENDL/PD-2016
¹²⁵ Te	KAERI	JENDL/PD-2016
¹²⁶ Te	KAERI	JENDL/PD-2016
¹²⁸ Te	KAERI	JENDL/PD-2016
¹³⁰ Te	KAERI	JENDL/PD-2016
¹²⁷ I	KAERI	JENDL/PD-2016
¹²⁹ I	KAERI	JENDL/PD-2016
¹³² Xe		JAEA
¹³³ Cs	KAERI	KAERI
¹³⁵ Cs	KAERI	JENDL/PD-2016
¹³⁷ Cs	KAERI	JENDL/PD-2016
¹³⁸ Ba		KAERI

TABLE II continued.

Nuclide	IAEA 1999	IAEA 2019
¹³⁹ La		JAEA
¹⁴⁰ Ce		KAERI
¹⁴² Ce		KAERI
¹⁴¹ Pr	KAERI	JENDL/PD-2016
¹⁴² Nd		KAERI
¹⁴³ Nd		KAERI
¹⁴⁴ Nd		KAERI
¹⁴⁵ Nd		KAERI
¹⁴⁶ Nd		KAERI
¹⁴⁸ Nd		KAERI
¹⁵⁰ Nd		KAERI
¹⁴⁴ Sm	KAERI	JAEA
¹⁴⁷ Sm	KAERI	JAEA
¹⁴⁸ Sm	KAERI	JAEA
¹⁴⁹ Sm	KAERI	JAEA
¹⁵⁰ Sm	KAERI	JAEA
¹⁵¹ Sm	KAERI	JAEA
¹⁵² Sm	KAERI	JAEA
¹⁵⁴ Sm	KAERI	JAEA
¹⁵³ Eu		KAERI
¹⁵⁶ Gd		JAEA
¹⁵⁷ Gd		JAEA
¹⁵⁸ Gd		JAEA
¹⁶⁰ Gd		JENDL/PD-2016
¹⁵⁸ Tb	KAERI	JENDL/PD-2016
¹⁵⁹ Tb	KAERI	IFIN-HH
¹⁶² Dy		JAEA
¹⁶³ Dy		JAEA
¹⁶⁵ Ho	KAERI	IFIN-HH
¹⁶⁶ Er		JAEA
¹⁷⁰ Er		JAEA
¹⁶⁹ Tm		IFIN-HH
¹⁷⁵ Lu		KAERI
¹⁷⁴ Hf		JAEA
¹⁷⁶ Hf		JAEA
¹⁷⁷ Hf		JAEA
¹⁷⁸ Hf		JAEA
¹⁷⁹ Hf		JAEA
¹⁸⁰ Hf		JAEA
¹⁸¹ Ta	JAERI	IFIN-HH
¹⁸⁰ W	CIAE	CIAE
¹⁸² W	JAERI	CIAE
¹⁸³ W	CIAE	CIAE
¹⁸⁴ W	LANL	CIAE
¹⁸⁶ W	JAERI	CIAE
¹⁸⁵ Re		JAEA
¹⁸⁷ Re		JAEA
¹⁸⁶ Os		KAERI
¹⁸⁸ Os		KAERI
¹⁸⁹ Os		KAERI
¹⁹⁰ Os		KAERI
¹⁹² Os		KAERI
¹⁹⁴ Pt		JAEA
¹⁹⁷ Au	KAERI	JAEA
²⁰⁶ Pb	LANL	JENDL/PD-2016

TABLE II continued.

Nuclide	IAEA 1999	IAEA 2019
²⁰⁷ Pb	LANL	JENDL/PD-2016
²⁰⁸ Pb	LANL	JENDL/PD-2016
²⁰⁹ Bi	CIAE	KAERI
²²⁶ Ra		JAEA
²³² Th	IPPE	JENDL/PD-2016
²³³ U	IPPE	JENDL/PD-2016
²³⁴ U	IPPE	JENDL/PD-2016
²³⁵ U	IPPE	JENDL/PD-2016
²³⁶ U	IPPE	JENDL/PD-2016
²³⁸ U	IPPE	JENDL/PD-2016
²³⁷ Np		JENDL/PD-2016
²³⁸ Pu	IPPE	JENDL/PD-2016
²³⁹ Pu	IPPE	JENDL/PD-2016
²⁴¹ Pu	IPPE	JENDL/PD-2016

Appendix B: GDR ATLAS

Here we summarize the updated tables for the recommended experimental GDR parameters within the Standard Lorentzian (SLO) and the Simplified version of the modified Lorentzian (SMLO) approaches. In the case of double humped shape, two sets of GDR parameters are given. A complete list of all the references is given at <https://www-nds.iaea.org/CRP-photonuclear/>, and only abbreviations are given for the sake of simplicity.

TABLE III. Recommended experimental GDR parameters within the Standard Lorentzian (SLO) approach.

	E [MeV]	Γ [MeV]	σ [mb]	Range [MeV]	Ref.
⁶ Li	23.69	5.26	3.71	21.5 – 27.0	1986Var
⁷ Li	18.59	16.28	3.65	13.2 – 25.6	1985Ahr
⁹ Be	23.75	9.47	5.17	17.5 – 26.0	1975Ahr
¹⁰ B	21.72	9.08	4.64	8.5 – 24.9	1987Ahs
¹² C	22.86	3.61	21.30	20.1 – 25.0	1969Bez
¹³ C	24.60	8.43	12.71	14.5 – 29.0	2002Ish
¹⁴ C	15.41	5.82	7.49	14.5 – 30.0	2002Ish
	26.13	7.78	8.13		
^{nat} C	23.12	4.19	19.28	19.5 – 25.6	1985Ahr
¹⁴ N	23.05	6.95	22.95	18.2 – 28.0	1969Bez
¹⁵ N	24.78	12.82	13.82	14.5 – 28.0	2002Ish
¹⁶ O	23.70	5.36	27.96	18.1 – 26.0	1975Ahr
¹⁷ O	23.40	5.48	21.82	18.5 – 26.5	2002Ish
¹⁸ O	19.08	2.12	5.13	18.5 – 26.0	2002Ish
	24.10	5.25	13.48		
^{nat} O	23.60	5.82	27.07	18.9 – 27.9	1985Ahr
¹⁹ F	21.61	12.57	16.58	10.0 – 24.0	2002Ish
²³ Na	17.43	3.10	12.38	14.2 – 23.0	1981Ish
	21.13	4.51	26.98		
²⁴ Mg	19.51	2.71	21.40	16.5 – 27.0	1966Dol
	23.88	8.86	25.20		
²⁵ Mg	22.06	6.09	34.99	9.0 – 24.2	2002Ish
²⁶ Mg	17.38	2.15	16.53	16.1 – 26.5	2003Var
	23.64	7.25	39.12		
^{nat} Mg	22.55	7.97	20.88	15.1 – 26.6	1965Wyc
²⁷ Al	20.73	7.45	38.99	14.0 – 24.1	1985Ahr
²⁸ Si	19.81	2.56	38.75	16.7 – 23.0	2003Var
	21.81	3.15	40.23		
²⁹ Si	20.70	5.60	40.01	14.2 – 23.0	2002Ish
³⁰ Si	20.86	7.40	29.56	14.2 – 23.0	2002Ish
^{nat} Si	20.35	4.53	51.41	16.4 – 25.8	1975Ahr
	25.16	2.86	10.47		
³² S	19.51	4.83	35.43	14.7 – 23.0	1968Dol
³⁴ S	20.89	9.61	50.54	12.0 – 25.0	1986Ass
^{nat} S	20.31	5.48	47.84	17.2 – 23.6	1965Wyc
⁴⁰ Ar	19.86	9.12	56.89	10.5 – 25.0	2002Ish
^{nat} K	21.12	6.89	22.58	16.0 – 25.9	1974Ve1
⁴⁰ Ca	20.58	6.23	104.78	17.2 – 23.7	1966Dol
⁴² Ca	20.11	8.07	72.15	15.2 – 23.0	2003Ero
⁴⁴ Ca	19.60	11.33	63.70	15.5 – 26.0	2003Ero
⁴⁸ Ca	19.70	6.23	105.44	17.9 – 21.6	1987Oke
^{nat} Ca	20.06	4.89	94.13	15.1 – 24.0	1975Ahr
⁴⁶ Ti	19.96	6.92	78.94	13.2 – 25.0	2002Ish

TABLE III continued.

	E [MeV]	Γ [MeV]	σ [mb]	Range [MeV]	Ref.
⁴⁸ Ti	19.78	8.42	63.74	14.5 – 23.0	2002Ish
⁵¹ V	17.90	4.55	60.32	14.1 – 22.9	1962Fu1
	21.26	4.37	26.38		
⁵² Cr	19.16	6.19	81.34	14.3 – 23.0	2002Ish
⁵⁵ Mn	16.43	2.95	27.02	14.0 – 23.0	1979Al2
	19.77	8.61	52.03		
⁵⁴ Fe	19.35	5.50	147.00	16.0 – 23.0	1978Nor
⁵⁹ Co	16.43	2.73	28.28	14.0 – 20.9	1979Al2
	18.64	7.31	57.16		
⁵⁸ Ni	18.78	5.57	87.90	14.1 – 22.0	2003Var
⁶⁰ Ni	16.69	3.47	62.80	12.1 – 21.0	2003Var
	19.57	5.26	71.14		
⁶³ Cu	16.43	4.84	79.79	14.0 – 21.0	2003Var
	20.15	5.52	49.39		
⁶⁵ Cu	16.92	8.09	86.38	14.2 – 21.0	2003Var
^{nat} Cu	18.12	5.61	97.93	14.4 – 24.9	1965Wyc
⁶⁴ Zn	16.23	3.25	41.21	14.0 – 20.8	1976Ca1
	19.16	5.91	54.90		
⁶⁵ Zn	16.17	3.06	34.89	12.0 – 21.0	2003Rod
	19.04	6.50	55.53		
⁷⁰ Ge	15.16	5.92	160.51	10.0 – 20.0	1975Mcc
⁷² Ge	17.88	5.71	167.57	10.0 – 24.0	1975Mcc
⁷⁴ Ge	14.51	2.01	25.54	13.1 – 20.8	1976Ca1
	17.03	7.97	100.80		
⁷⁶ Ge	15.48	4.37	61.70	13.1 – 20.8	1976Ca1
	18.87	10.99	71.09		
⁷⁵ As	14.98	3.66	41.85	13.1 – 20.9	1969Be1
	17.59	7.12	75.35		
⁷⁶ Se	15.67	6.33	151.59	13.1 – 19.7	1978Gur
⁷⁸ Se	14.97	3.91	70.45	13.1 – 20.8	1976Ca1
	18.42	6.19	79.42		
⁸⁰ Se	16.60	6.80	137.82	13.1 – 20.0	2016Va1
⁸² Se	16.00	5.68	175.06	13.1 – 19.9	1978Gur
^{nat} Rb	16.73	4.25	190.04	10.6 – 17.9	1971Lep
^{nat} Sr	16.79	4.32	205.99	10.9 – 17.9	1971Lep
⁸⁹ Y	16.74	4.23	224.56	14.0 – 19.0	1971Le1
⁹⁰ Zr	16.82	3.99	253.58	14.9 – 18.5	2003Var
⁹¹ Zr	16.58	4.17	183.17	14.0 – 18.9	1967Be2
⁹² Zr	16.26	4.64	164.72	14.0 – 18.9	1967Be2
⁹⁴ Zr	16.21	5.25	159.83	14.0 – 18.9	1967Be2
⁹³ Nb	16.58	4.95	200.25	14.0 – 19.0	1971Le1
⁹² Mo	17.16	4.68	239.77	14.4 – 19.0	2003Var
⁹⁴ Mo	16.53	5.12	192.92	9.6 – 18.9	1974Be3
⁹⁶ Mo	16.11	5.64	184.80	13.2 – 17.0	1974Be3
⁹⁸ Mo	15.79	5.90	188.16	13.2 – 18.9	1974Be3
¹⁰⁰ Mo	15.72	7.68	170.10	12.1 – 20.0	1974Be3
¹⁰³ Rh	16.24	7.49	192.03	13.1 – 19.0	2003Var
¹⁰⁸ Pd	14.97	5.42	143.49	10.0 – 19.0	1969Dea
	18.13	4.03	103.37		
^{nat} Pd	15.89	6.30	201.91	10.2 – 17.8	1971Lep
¹⁰⁷ Ag	15.83	6.49	185.05	9.5 – 19.0	1969Ish
¹⁰⁹ Ag	13.54	3.49	80.46	13.1 – 19.0	1969Ish
	16.62	4.41	113.46		
^{nat} Ag	16.06	7.33	197.91	13.2 – 18.9	1971Lep
^{nat} Cd	15.77	5.70	228.50	10.2 – 17.8	1971Lep

TABLE III continued.

	E [MeV]	Γ [MeV]	σ [mb]	Range [MeV]	Ref.
¹¹⁵ In	15.72	5.57	245.50	13.2 – 17.8	1974Le1
¹¹² Sn	15.62	5.01	262.94	10.9 – 18.0	1974Sor
¹¹⁴ Sn	15.82	6.08	243.01	13.1 – 18.0	1975Sor
¹¹⁶ Sn	15.55	5.06	269.30	13.1 – 17.9	1974Le1
¹¹⁷ Sn	15.64	5.02	257.30	13.2 – 17.8	1974Le1
¹¹⁸ Sn	15.43	4.84	277.65	13.1 – 17.9	1974Le1
¹¹⁹ Sn	15.53	4.78	251.37	13.0 – 17.9	1969Fu1
¹²⁰ Sn	15.37	5.08	284.00	13.1 – 17.9	1974Le1
¹²² Sn	15.34	4.73	266.89	13.1 – 18.0	1975Sor
¹²⁴ Sn	15.31	4.94	270.63	13.1 – 18.0	2003Var
^{nat} Sb	15.48	5.01	279.38	10.2 – 17.8	1971Lep
¹²⁴ Te	15.23	5.50	280.36	12.0 – 18.9	1976Le2
¹²⁶ Te	15.15	5.36	295.55	12.0 – 18.9	1976Le2
¹²⁸ Te	15.12	5.30	304.18	12.0 – 18.9	1976Le2
¹³⁰ Te	15.11	4.98	319.24	12.0 – 18.9	1976Le2
¹²⁷ I	14.77	4.09	229.29	12.0 – 20.0	1999Bel
	17.30	3.69	55.30		
¹³³ Cs	15.33	5.28	315.25	12.0 – 19.0	1974Le1
¹³⁸ Ba	15.13	4.51	317.33	12.1 – 18.7	2016Va2
^{nat} Ba	15.29	4.93	353.21	10.1 – 17.8	1971Be4
¹³⁹ La	15.24	4.82	367.47	12.0 – 18.9	1972De1
¹⁴⁰ Ce	15.03	4.39	381.89	12.0 – 18.9	1976Le2
¹⁴² Ce	14.85	5.08	331.25	12.0 – 18.9	1976Le2
¹⁴¹ Pr	15.19	4.23	342.68	12.1 – 16.9	1987Ber
¹⁴² Nd	14.95	4.46	360.54	13.1 – 18.0	2003Var
¹⁴³ Nd	15.00	4.73	347.60	12.0 – 19.0	1971Ca1
¹⁴⁴ Nd	15.04	5.25	315.51	12.0 – 18.9	1971Ca1
¹⁴⁵ Nd	14.94	6.27	295.27	12.0 – 18.9	1971Ca1
¹⁴⁶ Nd	14.73	5.74	309.04	12.0 – 18.9	1971Ca1
¹⁴⁸ Nd	12.78	4.03	110.23	10.8 – 18.6	1971Ca1
	15.49	5.22	215.89		
¹⁵⁰ Nd	12.30	3.38	175.75	10.8 – 18.6	1971Ca1
	16.03	5.12	220.50		
¹⁴⁴ Sm	15.31	4.42	381.69	12.1 – 18.9	1974Ca5
¹⁴⁸ Sm	14.82	5.06	337.78	12.1 – 18.9	1974Ca5
¹⁵⁰ Sm	14.59	5.92	310.73	12.1 – 18.9	1974Ca5
¹⁵² Sm	12.39	2.99	176.80	10.9 – 18.8	1974Ca5
	15.73	5.15	232.25		
¹⁵⁴ Sm	12.17	2.80	181.90	10.9 – 18.6	1981Gur
	15.63	5.89	209.70		
¹⁵¹ Eu	13.88	4.69	254.17	10.2 – 18.0	1971Vas
	14.45	0.75	65.45		
¹⁵³ Eu	12.33	2.77	155.86	10.9 – 18.7	1969Be8
	15.78	5.76	219.21		
¹⁵² Gd	11.79	3.03	145.74	10.2 – 18.0	1971Vas
	14.72	3.16	253.50		
¹⁵⁴ Gd	11.97	2.65	163.89	10.2 – 18.0	1971Vas
	15.05	3.35	245.22		
¹⁵⁶ Gd	12.46	3.14	230.03	10.9 – 18.7	1981Gur
	15.79	4.56	215.94		
¹⁵⁸ Gd	11.86	2.94	182.05	10.2 – 18.0	1971Vas
	15.16	3.31	245.62		
¹⁶⁰ Gd	12.28	3.33	234.33	10.9 – 18.8	2003Var
	16.06	5.12	247.23		

TABLE III continued.

	E [MeV]	Γ [MeV]	σ [mb]	Range [MeV]	Ref.
¹⁵⁹ Tb	12.42	2.71	171.70	11.1 – 19.0	1976Gor
	15.86	5.98	295.78		
¹⁶⁵ Ho	12.38	2.59	220.67	11.1 – 18.7	1981Gur
	15.48	4.05	226.69		
¹⁶⁸ Er	12.09	3.66	237.40	10.9 – 18.8	1981Gur
	15.54	3.99	252.64		
¹⁷⁴ Yb	12.50	3.41	339.31	10.9 – 18.7	1981Gur
	15.68	3.74	291.85		
¹⁷⁵ Lu	12.32	2.59	218.42	11.0 – 18.7	1969Be6
	15.47	4.64	284.83		
¹⁷⁶ Hf	12.34	2.77	279.26	10.9 – 17.9	1977Gor
	15.67	4.72	275.10		
¹⁷⁸ Hf	12.42	4.89	363.72	10.8 – 18.6	1981Gur
	15.70	3.13	234.94		
¹⁸⁰ Hf	12.55	4.71	351.75	10.8 – 18.7	1981Gur
	15.61	3.27	243.23		
¹⁸¹ Ta	12.19	2.93	262.35	10.8 – 18.6	1981Gur
	14.99	5.13	317.52		
¹⁸² W	11.98	3.91	283.99	11.0 – 18.8	1981Gur
	14.94	5.16	259.40		
¹⁸⁴ W	11.92	4.52	347.68	11.0 – 17.6	1981Gur
	15.05	3.87	233.17		
¹⁸⁶ W	13.04	6.60	410.29	10.9 – 18.7	1981Gur
	14.89	2.12	69.05		
¹⁸⁵ Re	12.59	2.22	221.75	10.2 – 18.0	1973Gor
	15.17	6.02	328.79		
nat Re	14.11	6.52	470.27	10.2 – 18.0	1975Vey
¹⁸⁶ Os	12.73	2.34	214.24	11.1 – 18.9	2015Var
	14.73	4.08	355.57		
¹⁸⁸ Os	12.81	2.83	281.11	10.8 – 18.9	2014Var
	14.93	3.83	388.79		
¹⁸⁹ Os	12.92	3.07	329.04	10.8 – 18.9	2014Var
	15.02	3.94	299.55		
¹⁹⁰ Os	13.10	3.34	372.87	10.8 – 18.9	2015Var
	15.12	3.80	247.98		
¹⁹² Os	12.59	2.13	173.74	10.8 – 18.9	2015Var
	14.32	4.60	426.27		
¹⁹¹ Ir	12.72	2.08	183.14	11.0 – 16.8	1978Go1
	14.21	5.27	382.41		
¹⁹³ Ir	12.86	1.90	229.81	11.0 – 16.8	1978Go1
	14.30	5.62	356.07		
nat Ir	13.77	4.86	495.41	10.2 – 18.0	1975Vey
¹⁹⁴ Pt	13.42	3.61	453.02	11.0 – 17.8	1978Go1
	15.97	6.16	111.63		
¹⁹⁵ Pt	12.99	2.92	357.53	11.0 – 17.8	1978Go1
	14.90	4.85	253.95		
¹⁹⁶ Pt	13.28	3.10	345.43	11.0 – 17.8	1978Go1
	14.81	7.51	192.99		
¹⁹⁸ Pt	13.56	4.88	528.76	11.0 – 17.8	1978Go1
¹⁹⁷ Au	13.58	5.32	522.88	11.1 – 17.0	1981Gur
²⁰³ Tl	14.04	3.77	436.99	9.0 – 17.9	1970Ant
²⁰⁵ Tl	14.46	2.95	478.97	10.5 – 17.9	1970Ant
²⁰⁶ Pb	13.58	3.83	512.45	10.0 – 17.0	1964Ha2
²⁰⁷ Pb	13.55	3.95	479.80	10.0 – 17.0	1964Ha2

TABLE III continued.

	E [MeV]	Γ [MeV]	σ [mb]	Range [MeV]	Ref.
²⁰⁸ Pb	13.37	3.93	645.49	10.9 – 18.8	2003Var
nat Pb	13.48	3.99	637.69	12.1 – 16.9	1985Ahr
²⁰⁹ Bi	13.79	5.02	588.63	10.9 – 18.3	1976Gu2
²³² Th	10.86	2.86	230.28	10.2 – 18.3	1976Gu1
	13.74	4.74	382.21		
²³³ U	10.98	1.53	140.38	9.4 – 17.8	1986Be2
	13.30	5.71	439.10		
²³⁴ U	11.18	2.41	379.61	9.4 – 17.8	1986Be2
	14.03	4.46	398.77		
²³⁵ U	10.82	3.88	302.02	9.5 – 18.4	1976Gu1
	13.80	4.54	319.35		
²³⁶ U	11.04	2.65	279.96	9.5 – 17.8	1980Ca1
	13.92	4.77	407.27		
²³⁸ U	11.06	2.95	283.53	9.2 – 18.8	1976Gu1
	14.26	4.80	347.16		
nat U	10.73	2.47	301.11	10.2 – 17.9	1985Ahr
²³⁷ Np	13.72	5.04	405.91		
	10.99	2.20	310.02	9.4 – 17.8	1986Be2
²³⁹ Pu	14.08	4.66	535.89		
	11.07	3.29	227.77	9.3 – 18.7	1976Gu1
	14.00	5.51	358.18		

TABLE IV. Recommended experimental GDR parameters within the Simplified version of the modified Lorentzian (SMLO) approach.

	E [MeV]	Γ [MeV]	σ [mb]	Range [MeV]	Ref.
⁶ Li	23.75	5.33	3.70	21.5 – 27.0	1986Var
⁷ Li	20.21	21.81	3.47	13.2 – 25.6	1985Ahr
⁹ Be	24.18	10.86	5.09	17.5 – 26.0	1975Ahr
¹⁰ B	23.31	17.51	4.12	8.5 – 24.9	1987Ahs
¹² C	22.90	3.69	21.21	20.1 – 25.0	1969Bez
¹³ C	25.02	10.72	11.65	14.5 – 29.0	2002Ish
	15.69	6.51	7.67	14.5 – 30.0	2002Ish
¹⁴ C	26.27	7.11	7.74		
	23.14	4.24	19.38	19.5 – 25.6	1985Ahr
¹⁴ N	23.19	7.09	22.95	18.2 – 28.0	1969Bez
¹⁵ N	26.29	19.45	12.85	14.5 – 28.0	2002Ish
¹⁶ O	23.78	5.67	27.70	18.1 – 26.0	1975Ahr
¹⁷ O	23.46	5.95	21.29	18.5 – 26.5	2002Ish
	19.12	2.31	5.51	18.5 – 26.0	2002Ish
¹⁸ O	24.19	5.24	13.38		
	23.64	5.88	27.13	18.9 – 27.9	1985Ahr
¹⁹ F	24.09	24.69	14.94	10.0 – 24.0	2002Ish
²³ Na	17.57	3.75	13.62	14.2 – 23.0	1981Ish
	21.26	4.35	25.45		
²⁴ Mg	19.46	2.80	22.51	16.5 – 27.0	1966Dol
	24.30	9.80	24.18		
²⁵ Mg	22.73	8.44	33.04	9.0 – 24.2	2002Ish
²⁶ Mg	17.39	2.36	17.88	16.1 – 26.5	2003Var
	23.83	7.57	38.38		
nat Mg	22.32	8.72	21.08	15.1 – 26.6	1965Wyc

TABLE IV continued.

	E [MeV]	Γ [MeV]	σ [mb]	Range [MeV]	Ref.
²⁷ Al	21.00	8.62	37.64	14.0 – 24.1	1985Ahr
²⁸ Si	19.88	2.91	38.41	16.7 – 23.0	2003Var
	21.84	3.39	36.60		
²⁹ Si	20.97	6.88	37.83	14.2 – 23.0	2002Ish
³⁰ Si	21.32	9.16	28.52	14.2 – 23.0	2002Ish
^{nat} Si	20.45	4.85	51.22	16.4 – 25.8	1975Ahr
	25.24	2.10	8.02		
³² S	19.57	5.10	34.93	14.7 – 23.0	1968Dol
³⁴ S	21.66	13.43	47.29	12.0 – 25.0	1986Ass
^{nat} S	20.42	5.74	47.22	17.2 – 23.6	1965Wyc
⁴⁰ Ar	19.91	11.50	54.19	10.5 – 25.0	2002Ish
^{nat} K	21.28	7.40	22.28	16.0 – 25.9	1974Ve1
⁴⁰ Ca	20.72	6.44	104.09	17.2 – 23.7	1966Dol
⁴² Ca	20.53	9.75	68.87	15.2 – 23.0	2003Ero
⁴⁴ Ca	20.08	12.45	62.19	15.5 – 26.0	2003Ero
⁴⁸ Ca	19.90	6.42	104.95	17.9 – 21.6	1987OKe
^{nat} Ca	20.09	5.07	93.50	15.1 – 24.0	1975Ahr
⁴⁶ Ti	19.95	7.99	76.44	13.2 – 25.0	2002Ish
⁴⁸ Ti	20.13	9.98	61.66	14.5 – 23.0	2002Ish
⁵¹ V	18.18	5.29	63.92	14.1 – 22.9	1962Fu1
	21.37	3.36	18.23		
⁵² Cr	19.16	6.70	79.20	14.3 – 23.0	2002Ish
⁵⁵ Mn	16.43	2.91	21.84	14.0 – 23.0	1979Al2
	20.13	11.28	51.12		
⁵⁴ Fe	19.39	5.69	145.35	16.0 – 23.0	1978Nor
⁵⁹ Co	16.44	2.42	20.11	14.0 – 20.9	1979Al2
	18.68	8.63	59.76		
⁵⁸ Ni	18.87	6.16	86.03	14.1 – 22.0	2003Var
⁶⁰ Ni	16.59	3.17	39.23	12.1 – 21.0	2003Var
	19.39	7.82	77.98		
⁶³ Cu	16.79	5.76	87.60	14.0 – 21.0	2003Var
	20.37	4.56	35.92		
⁶⁵ Cu	17.23	8.38	86.10	14.2 – 21.0	2003Var
^{nat} Cu	17.91	5.24	99.60	14.4 – 24.9	1965Wyc
⁶⁴ Zn	16.37	3.84	48.04	14.0 – 20.8	1976Ca1
	19.49	5.82	47.80		
⁶⁵ Zn	16.06	2.26	21.02	12.0 – 21.0	2003Rod
	18.87	8.62	60.27		
⁷⁰ Ge	15.31	7.19	151.53	10.0 – 20.0	1975Mcc
⁷² Ge	17.85	6.22	159.50	10.0 – 24.0	1975Mcc
⁷⁴ Ge	14.42	2.46	32.43	13.1 – 20.8	1976Ca1
	17.47	8.37	96.06		
⁷⁶ Ge	15.42	3.62	38.51	13.1 – 20.8	1976Ca1
	18.69	13.81	82.19		
⁷⁵ As	15.25	4.73	59.84	13.1 – 20.9	1969Be1
	18.16	6.73	59.05		
⁷⁶ Se	15.86	6.50	150.72	13.1 – 19.7	1978Gur
⁷⁸ Se	15.23	4.67	82.67	13.1 – 20.8	1976Ca1
	18.76	5.68	66.04		
⁸⁰ Se	16.84	7.45	135.22	13.1 – 20.0	2016Va1
⁸² Se	16.13	5.81	175.20	13.1 – 19.9	1978Gur
^{nat} Rb	16.92	4.93	185.68	10.6 – 17.9	1971Lep
^{nat} Sr	16.99	5.03	201.18	10.9 – 17.9	1971Lep
⁸⁹ Y	16.82	4.42	222.48	14.0 – 19.0	1971Le1

TABLE IV continued.

	E [MeV]	Γ [MeV]	σ [mb]	Range [MeV]	Ref.
⁹⁰ Zr	16.90	4.13	251.98	14.9 – 18.5	2003Var
⁹¹ Zr	16.64	4.32	181.76	14.0 – 18.9	1967Be2
⁹² Zr	16.34	4.70	165.00	14.0 – 18.9	1967Be2
⁹⁴ Zr	16.35	5.52	157.58	14.0 – 18.9	1967Be2
⁹³ Nb	16.70	5.18	198.63	14.0 – 19.0	1971Le1
⁹² Mo	17.28	5.05	236.19	14.4 – 19.0	2003Var
⁹⁴ Mo	16.73	6.04	186.31	9.6 – 18.9	1974Be3
⁹⁶ Mo	16.42	6.52	182.00	13.2 – 17.0	1974Be3
⁹⁸ Mo	15.96	6.17	186.76	13.2 – 18.9	1974Be3
¹⁰⁰ Mo	16.02	8.44	167.02	12.1 – 20.0	1974Be3
¹⁰³ Rh	16.59	8.44	187.85	13.1 – 19.0	2003Var
¹⁰⁸ Pd	16.15	8.26	169.74	10.0 – 19.0	1969Dea
	18.09	1.65	45.85		
^{nat} Pd	16.24	7.63	195.79	10.2 – 17.8	1971Lep
¹⁰⁷ Ag	16.05	7.51	179.36	9.5 – 19.0	1969Ish
¹⁰⁹ Ag	13.74	3.81	90.32	13.1 – 19.0	1969Ish
	16.76	4.17	103.59		
^{nat} Ag	16.39	8.03	194.95	13.2 – 18.9	1971Lep
^{nat} Cd	16.03	6.69	222.13	10.2 – 17.8	1971Lep
¹¹⁵ In	15.91	6.00	242.23	13.2 – 17.8	1974Le1
¹¹² Sn	15.82	5.87	254.14	10.9 – 18.0	1974Sor
¹¹⁴ Sn	16.08	6.74	238.62	13.1 – 18.0	1975Sor
¹¹⁶ Sn	15.69	5.29	267.45	13.1 – 17.9	1974Le1
¹¹⁷ Sn	15.77	5.29	254.71	13.2 – 17.8	1974Le1
¹¹⁸ Sn	15.55	5.02	276.03	13.1 – 17.9	1974Le1
¹¹⁹ Sn	15.65	5.09	248.89	13.0 – 17.9	1969Fu1
¹²⁰ Sn	15.50	5.26	282.55	13.1 – 17.9	1974Le1
¹²² Sn	15.45	4.98	262.09	13.1 – 18.0	1975Sor
¹²⁴ Sn	15.41	5.06	269.85	13.1 – 18.0	2003Var
^{nat} Sb	15.62	5.59	273.38	10.2 – 17.8	1971Lep
¹²⁴ Te	15.36	5.81	276.72	12.0 – 18.9	1976Le2
¹²⁶ Te	15.27	5.62	292.05	12.0 – 18.9	1976Le2
¹²⁸ Te	15.23	5.55	300.47	12.0 – 18.9	1976Le2
¹³⁰ Te	15.21	5.19	316.19	12.0 – 18.9	1976Le2
¹²⁷ I	15.05	4.76	242.61	12.0 – 20.0	1999Bel
	17.33	1.83	22.56		
¹³³ Cs	15.44	5.50	312.95	12.0 – 19.0	1974Le1
¹³⁸ Ba	15.16	4.68	312.33	12.1 – 18.7	2016Va2
^{nat} Ba	15.46	5.57	344.80	10.1 – 17.8	1971Be4
¹³⁹ La	15.30	5.11	360.94	12.0 – 18.9	1972De1
¹⁴⁰ Ce	15.09	4.51	378.93	12.0 – 18.9	1976Le2
¹⁴² Ce	14.95	5.24	328.39	12.0 – 18.9	1976Le2
¹⁴¹ Pr	15.33	4.49	340.06	12.1 – 16.9	1987Ber
¹⁴² Nd	15.02	4.41	361.62	13.1 – 18.0	2003Var
¹⁴³ Nd	15.08	4.99	341.49	12.0 – 19.0	1971Ca1
¹⁴⁴ Nd	15.17	5.56	311.38	12.0 – 18.9	1971Ca1
¹⁴⁵ Nd	15.14	6.75	289.80	12.0 – 18.9	1971Ca1
¹⁴⁶ Nd	14.88	6.04	304.19	12.0 – 18.9	1971Ca1
¹⁴⁸ Nd	13.34	5.41	156.93	10.8 – 18.6	1971Ca1
	15.79	4.57	164.60		
¹⁵⁰ Nd	12.49	3.93	194.54	10.8 – 18.6	1971Ca1
	16.23	4.85	197.33		
¹⁴⁴ Sm	15.37	4.53	379.27	12.1 – 18.9	1974Ca5
¹⁴⁸ Sm	14.91	5.15	336.69	12.1 – 18.9	1974Ca5

TABLE IV continued.

	E [MeV]	Γ [MeV]	σ [mb]	Range [MeV]	Ref.
¹⁵⁰ Sm	14.76	6.01	309.77	12.1 – 18.9	1974Ca5
¹⁵² Sm	12.56	3.53	202.99	10.9 – 18.8	1974Ca5
	15.97	4.77	206.96		
¹⁵⁴ Sm	12.31	3.27	208.97	10.9 – 18.6	1981Gur
	15.95	5.53	186.51		
¹⁵¹ Eu	13.43	5.18	168.67	10.2 – 18.0	1971Vas
	14.52	2.28	158.70		
¹⁵³ Eu	12.47	3.26	180.63	10.9 – 18.7	1969Be8
	16.07	5.48	198.64		
¹⁵² Gd	11.96	3.49	161.00	10.2 – 18.0	1971Vas
	14.75	2.87	234.24		
¹⁵⁴ Gd	12.09	3.08	176.27	10.2 – 18.0	1971Vas
	15.10	3.09	227.94		
¹⁵⁶ Gd	12.63	3.61	252.40	10.9 – 18.7	1981Gur
	15.97	4.10	188.83		
¹⁵⁸ Gd	12.00	3.37	193.78	10.2 – 18.0	1971Vas
	15.19	2.97	231.63		
¹⁶⁰ Gd	12.47	3.85	258.30	10.9 – 18.8	2003Var
	16.26	4.69	218.92		
¹⁵⁹ Tb	12.55	3.23	205.41	11.1 – 19.0	1976Gor
	16.16	5.74	270.81		
¹⁶⁵ Ho	12.47	2.84	238.17	11.1 – 18.7	1981Gur
	15.59	3.78	209.10		
¹⁶⁸ Er	12.33	4.18	258.17	10.9 – 18.8	1981Gur
	15.65	3.58	222.84		
¹⁷⁴ Yb	12.73	3.95	367.77	10.9 – 18.7	1981Gur
	15.80	3.18	249.27		
¹⁷⁵ Lu	12.44	2.99	245.80	11.0 – 18.7	1969Be6
	15.65	4.32	260.78		
¹⁷⁶ Hf	12.46	3.13	303.74	10.9 – 17.9	1977Gor
	15.86	4.44	247.79		
¹⁷⁸ Hf	12.59	4.95	372.55	10.8 – 18.6	1981Gur
	15.65	3.00	218.91		
¹⁸⁰ Hf	12.74	4.93	364.50	10.8 – 18.7	1981Gur
	15.59	3.04	220.92		
¹⁸¹ Ta	12.36	3.41	311.29	10.8 – 18.6	1981Gur
	15.26	4.71	273.41		
¹⁸² W	13.08	7.29	380.79	11.0 – 18.8	1981Gur
	15.20	1.53	99.76		
¹⁸⁴ W	12.27	5.17	373.92	11.0 – 17.6	1981Gur
	15.10	3.15	186.15		
¹⁸⁶ W	13.01	6.25	381.26	10.9 – 18.7	1981Gur
	14.81	2.84	122.86		
¹⁸⁵ Re	12.89	3.48	329.91	10.2 – 18.0	1973Gor
	15.84	4.37	252.98		
^{nat} Re	14.30	7.05	462.90	10.2 – 18.0	1975Vey
¹⁸⁶ Os	13.00	3.09	309.47	11.1 – 18.9	2015Var
	15.09	3.39	274.49		
¹⁸⁸ Os	13.14	3.59	382.50	10.8 – 18.9	2014Var
	15.22	2.98	294.24		
¹⁸⁹ Os	13.18	3.64	416.27	10.8 – 18.9	2014Var
	15.32	2.95	214.75		
¹⁹⁰ Os	13.21	3.59	427.44	10.8 – 18.9	2015Var
	15.28	2.93	206.88		

TABLE IV continued.

	E [MeV]	Γ [MeV]	σ [mb]	Range [MeV]	Ref.
¹⁹² Os	13.08	3.61	365.35	10.8 – 18.9	2015Var
	14.98	3.68	249.26		
¹⁹¹ Ir	13.16	3.75	418.50	11.0 – 16.8	1978Go1
	15.24	3.69	170.79		
¹⁹³ Ir	12.85	1.64	160.61	11.0 – 16.8	1978Go1
	14.18	5.94	393.43		
^{nat} Ir	13.81	4.97	492.98	10.2 – 18.0	1975Vey
¹⁹⁴ Pt	13.66	4.29	499.56	11.0 – 17.8	1978Go1
	16.70	4.55	34.46		
¹⁹⁵ Pt	13.28	3.71	464.49	11.0 – 17.8	1978Go1
	15.44	3.56	137.09		
¹⁹⁶ Pt	13.38	2.87	235.00	11.0 – 17.8	1978Go1
	14.18	6.94	275.78		
¹⁹⁸ Pt	13.62	4.83	533.11	11.0 – 17.8	1978Go1
¹⁹⁷ Au	13.72	5.43	522.61	11.1 – 17.0	1981Gur
²⁰³ Tl	14.06	3.95	435.91	9.0 – 17.9	1970Ant
²⁰⁵ Tl	14.47	2.93	482.88	10.5 – 17.9	1970Ant
²⁰⁶ Pb	13.61	4.01	504.02	10.0 – 17.0	1964Ha2
²⁰⁷ Pb	13.57	4.22	467.03	10.0 – 17.0	1964Ha2
²⁰⁸ Pb	13.34	3.64	662.00	10.9 – 18.8	2003Var
^{nat} Pb	13.58	4.05	635.27	12.1 – 16.9	1985Ahr
²⁰⁹ Bi	13.87	5.04	591.22	10.9 – 18.3	1976Gu2
²³² Th	11.10	3.51	285.95	10.2 – 18.3	1976Gu1
	13.97	4.22	334.57		
²³³ U	11.01	2.23	209.80	9.4 – 17.8	1986Be2
	13.68	5.38	403.97		
²³⁴ U	11.30	2.83	428.01	9.4 – 17.8	1986Be2
	14.23	4.04	353.66		
²³⁵ U	11.11	4.52	345.36	9.5 – 18.4	1976Gu1
	13.92	3.88	269.50		
²³⁶ U	11.25	3.34	340.25	9.5 – 17.8	1980Ca1
	14.18	4.25	351.15		
²³⁸ U	11.24	3.54	324.58	9.2 – 18.8	1976Gu1
	14.45	4.26	305.65		
^{nat} U	10.86	2.83	353.45	10.2 – 17.9	1985Ahr
	13.96	4.69	368.18		
²³⁷ Np	11.10	2.72	366.61	9.4 – 17.8	1986Be2
	14.27	4.27	498.40		
²³⁹ Pu	11.47	4.50	303.03	9.3 – 18.7	1976Gu1
	14.37	4.76	278.70		